UNIVERSITY OF WARSAW
FACULTY OF PHYSICS

DOCTORAL THESIS

Quantum Metrology with Atoms and Light

Author:
Karol GIETKA

Supervisor:
dr hab. Jan CHWEDEŃCZUK

Auxiliary Supervisor:
dr Tomasz WASAK

December 6, 2018

Streszczenie

Kwantowa Metrologia z Atomami i Światłem

Głównym celem tej dysertacji jest zaproponowanie metod tworzenia kwantowych stanów materii oraz światła i sprawdzenie możliwości wykorzystania tych stanów do precyzyjnych pomiarów wielkości fizycznych. Pierwsza część tego celu realizowana jest przy pomocy formalizmu kwantowo-mechanicznego w kontekście teorii ultra-zimnych gazów atomowych oraz kwantowej elektrodynamiki we wnęce, natomiast druga część realizowana jest za pomocą metod teorii estymacji z informacją Fishera w roli głównej. Połączenie powyższych metod jest znane ogólnie pod pojęciem kwantowej metrologii. W ostatnich latach wiele teoretycznego i eksperymentalnego wysiłku zostało włożonego w dziedzinę kwantowej metrologii, ponieważ dzięki niej możliwy będzie nie tylko rozwój technik pomiarowych dających lepszą precyzję niż te same pomiary wykonane w ramach klasycznej teorii, ale także może być użyta do badania fundamentalnych aspektów mechaniki kwantowej takich jak splątanie.

Pierwszą metodą, którą rozważamy to mechanizm tworzenia tworzenia stanów spinowo-ściśniętych znany jako *one-axis twisting*, który może być zastosowany na przykład w kondensacie Bosego-Einsteina uwięzionego w podwójnej studni potencjału tworząc efektywnie kondensat dwu składnikowy. Pokazujemy, że stany spinowo-ściśnięte stanowią tylko małą rodzinę stanów splątanych, które mogą być wytworzone przez Hamiltonian *one-axis twisting*. Ta duża rodzina stanów typu *twisted* zawiera nawet najbardziej splątany stan znany jako kot Schroödingera. Pokazujemy również jak wykorzystać te kwantowe zasoby w pomiarze nieznanego parametru, wykorzystując nieidealne detektory atomowe oraz w przypadku kiedy oddziaływanie pomiędzy atomami nie jest dokładnie znane.

Drugi schemat tworzenia kwantowo-skorelowanych stanów jest oparty na *quantum non-demolition measurement*. W metodzie tej atom przelatujący przez wnękę optyczną zostaje splątany z obecnymi w niej fotonami, a w wyniku pomiaru wykonanego na atomie następuje kolaps funkcji falowej łącznego stanu materii i światła do nieklasycznego stanu światła. W celu uwzględnienia strat fotonów we wnęce używamy równania *master* w formie Lindblada. Pokazujemy jak takie nieklasyczne stany mogą zostać wydobyte z wnęki oraz użyte później w interferometrze Macha-Zehndera. Bazując na funkcji Wignera wyjaśniamy również jakie cechy tego rodzaju stanów przyczyniają się do niezwykle wysokiej czułości interferometru.

Na koniec pokazujemy, jak układ wykazujący właściwości chaotyczne może zostać badany z perspektywy metrologicznej za pomocą kwantowej informacji Fishera. Klasyczne układy chaotyczne to układy, które są bardzo czułe na warunki początkowe. Jednakże, kwantowe układy nie mogą wykazywać takiego rodzaju dynamiki, ponieważ równanie Schrödingera jest liniowe w funkcji falowej. Można jednak mówić o tak zwanych kwantowych sygnaturach chaosu. Na początku pokazujemy podręcznikowy przykład klasycznego chaosu, jakim jest podwójne wahadło, a następnie pokazujemy jak kwantowa informacja Fishera może posłużyć do badania charakterystycznych skal czasowych układów chaotycznych i przejścia pomiędzy porządkiem a chaosem. Takie podejście otwiera nowe możliwości badania związku pomiędzy kwantowym chaosem a porządkiem.

Abstract

Quantum Metrology with Atoms and Light

The primary objective of this dissertation is to propose methods of generating non-classical states of matter or light and examine the possibility of using such states in precise measurements of physical quantities. The first part of this objective is realised by using quantum-mechanical formalism with an emphasis on the theory of ultra-cold atomic gases and cavity quantum electrodynamics, and the second part is realised with methods of the theory of estimation with the Fisher information playing the pivotal role. The fusion of these methods is generally known as quantum metrology. In recent years, a lot of theoretical and experimental effort was put in the field of quantum metrology since it not only promises to develop measurement techniques that give better precision than the same measurements performed in a classical framework but also can be used to study the most fundamental aspects of quantum theory, like quantum entanglement.

The first method which we consider is based on the mechanism of creating spin-squeezed states known as the one-axis twisting, which can be realised, for instance, in a Bose-Einstein condensate trapped in a double-well potential forming effectively a two-mode system. We show that the spin-squeezed states are just a small family of entangled states that can be generated by one-axis twisting Hamiltonian. This vast family of twisted states includes even the highest entangled state known as the Schrödinger's cat. We also show how to exploit this quantum resource in a measurement of an unknown parameter with imperfect atomic detectors and when the strength of the interaction between the atoms is not precisely known.

The second scheme for creating non-classical states is based on the quantum non-demolition measurement. This method involves an atom passing through an optical cavity which entangles with the photons inside the cavity and a subsequent measurement on the atom that collapses the combined matter-light state to a non-classical state of light. To take into account photon losses in the cavity, we harness the master equation in Lindblad form. We show how such non-classical states can be extracted from the cavity and used later in a Mach-Zehnder interferometer. Based on the Wigner function, we also explain what features of this kind of states give rise to a high sensitivity of an interferometer.

Finally, we show how a system that exhibits chaotic properties can be studied from the metrological perspective with the help of quantum Fisher information. Classical chaotic systems are systems that are highly sensitive to initial conditions. However, quantum systems can never exhibit this type of dynamics since the Schrödinger's equation is linear. Therefore, one often says about quantum signatures of chaos. First, we show a textbook example of classical chaos, which is a double-rod pendulum, and, subsequently, we show how quantum Fisher information can serve to investigate characteristic time-scales of chaotic systems and the transition from integrable to chaotic dynamics. This could open a new possibility to study the relationship between the classical and quantum chaos.

Contents

Preface

This dissertation was written mainly during my ETIUDA internship in Innsbruck in the group of Helmut Ritsch and partially in Warsaw. I started writing it at the beginning of October 2017 and finished at the beginning of June 2018. I have to admit that the process of writing, although not that straightforward, was extremely satisfying, and I had a lot of fun during it. It helped me to categorise my knowledge somehow, rethink certain aspects that I already knew, and also learn a lot of new stuff, especially while re-deriving most of the Formulae contained in the thesis. It is unbelievable how many mistakes I have found in various books and articles, which was extremely annoying and frustrating. Anyway, I cannot blame the authors and editors because checking every single word or term in a formula is almost impossible. Therefore, I kindly ask not to blame me for any mistake that an observant reader may find, and for which I beg its pardon. Although English is not my native language, I decided to write this dissertation in English since I believe that English is currently the language of science, and so, in principle, any person, if interested, can read this thesis. Here, I would also like to apologise the reader for sentences or formulations that are not English-like and, of course, for those which are simply incorrect. Apart from this, I firmly believe that this thesis is understandable and intelligible.

The dissertation consists of two main parts. The first of them is an introductory part where I give a brief introduction to the field of quantum metrology, quantum optics, ultracold quantum gases in optical lattices, and theory of estimation. This part is based mostly on a few manuscripts including "Introductory Quantum Optics" by Christopher Gerry and Peter Knight, "Exploring the Quantum" by Serge Haroche, "Ultracold Quantum Gases in Optical Lattices" by Immanuel Bloch, "Quantum Theory of Phase Estimation" by Luca Pezzé and Augusto Smerzi, "Quantum Spin Squeezing" by Jian Ma *et. al.*, and a script of my supervisor to his lecture entitled "Quantum Interferometry." I also tried to give as many relevant references to the literature as possible. I tried to pick up the most exciting aspects of these theories from the viewpoint of quantum metrology and my research; thus many other things are just briefly mentioned in this dissertation. Otherwise, the first part would be much longer, and I found it unnecessary to write such a long introduction.

The second part is devoted to my research in the field of quantum metrology. I decided to base this thesis on three somewhat connected topics. I begin with metrology with ultracold atoms, then I switch to metrology with photons, and finally, I deal with a hybrid system composed of atoms and photons. First two chapters in the second part are based on my publications with a short introduction. The third chapter of the second part describes on-going research, and the last chapter of the second part contains the conclusions.

Finally, I would like to thank all the people who directly or indirectly contributed to the creation of this dissertation and who supported me during my studies. Many thanks to my fellow PhD students Michał Jachura and Maciek Konieczka with whom I shared the office and with whom I conducted many interesting discussions not

only about physics. Special thanks to Michał Jachura with whom I fought countless battles in Pikachu Volleyball which helped and prepared me mentally for everything that I have encountered before the defence of this dissertation. Many thanks to Paweł Bączyk, although we did not share the office, I felt as if he was a substantial part of it. Many thanks to professor Helmut Ritsch who hosted me in his group in Innsbruck nine months in total and who showed me the beauty of physics and the beauty of being a physicist. Many thanks to doctor Francesco Piazza who helped me a lot during my last year when we were working on the quantum chaos. Many thanks to my parents for support during these hard but exciting years. Many thanks to my crazy girlfriend without whom I would not be the person I am. Finally, many thanks to Jan Chwedeńczuk and Tomasz Wasak for careful reading and helpful comments that improved the quality of this manuscript.

Introduction

Contents

0.1 Development of quantum metrology in a nutshell

Quantum metrology [1] is a branch of physics which exploits quantum-mechanical formalism to describe physical systems [2] in order to perform exact measurements of physical parameters. With the help of quantum effects, especially entanglement, it is possible to overcome the limit of precision set by classical physics [3]. One of the most paradigmatic examples is the use of squeezed states of light in the Mach-Zehnder interferometer to perform accurate phase measurements [4].

Interferometry, in general, is a whole group of techniques in which electromagnetic waves or matter waves are superimposed giving rise to interference. To extract information about the system under investigation, one analyses the interferometric signal which depends on the relative phase between the interfering waves. In optical interferometry, this phase shift is typically caused by a difference in the optical path that light passes in the arms of the interferometer. According to this principle, Albert Michelson and Edward Morley showed in 1887 that the theory of aether, a medium in which the light was supposed to propagate, cannot be correct [5]. This surprising for those times result contributed to the development of a variety of new theories trying to explain the outcome of the so-called Michelson-Morley experiment. The most profound was, proposed by Albert Einstein, the special theory of relativity.

Another notable example of utilisation of interferometry is the aforementioned Mach-Zehnder interferometer, which initially served to study the influence of air pressure on the index of refraction of water and to study gas dynamics in one of the interferometer's arms [6, 7]. This simple apparatus is currently one of the most commonly used optical interferometers, and what is more, it has been successfully implemented with waves of matter [8]. Besides its numerous applications in optics, this interferometer can also be used to investigate one of the least intuitive predictions of quantum mechanics, a phenomenon known as entanglement [9, 10].

Interferometers are also used in the observation of ripples in the curvature of space-time propagating with the speed of light, known as gravitational waves. This phenomenon, predicted theoretically in 1916 by Albert Einstein [11], was experimentally corroborated only 100 years later by the LIGO scientific collaboration [12]. The first-ever detected gravitational waves originated from a merger of two black holes with masses of about 29 and 36 mass of the Sun. The coalescence of the two black holes took place some 1.3 ± 0.6 billion years ago, and as a result mass of about three solar masses was converted into gravitational waves. For theoretically predicated waves, the order of deformation of a 400 km object is less than 10^{-19} m. Such a minute deformation was possible to observe only with the help of a very precise

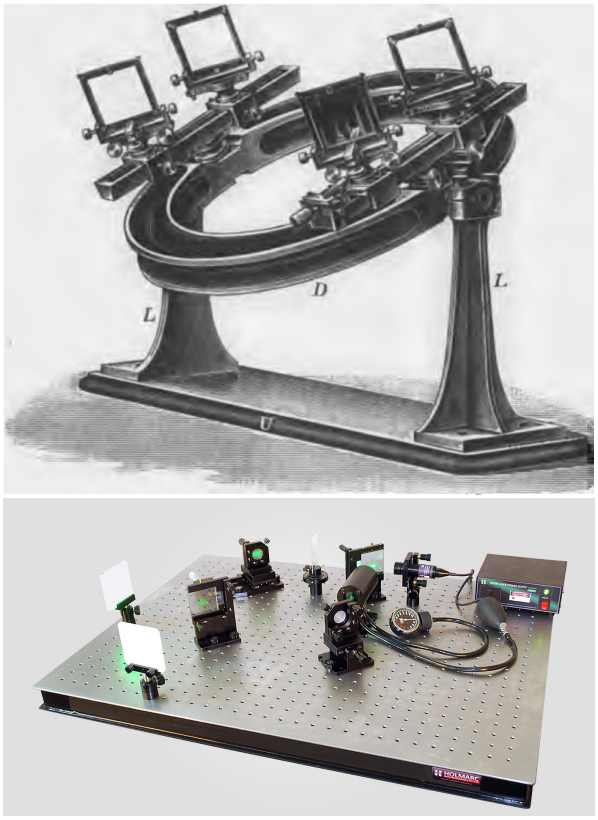

FIGURE 1: A scheme presenting the Mach-Zehnder interferometer. Print (top) taken from the original work of Ludwig Mach [7] and its modern version (bottom). A light beam enters the interferometer through a balanced beam-splitter and thereupon splits into two beams. Subsequently, two beams are reflected from the mirrors and enter another balanced beam-splitter. If the beams passed different optical paths, for instance, as a result of different index of refraction in one of the interferometer's arms, the interference pattern would change its shape.

laser interferometer. This ground-breaking event heralded the dawn of gravitational wave astronomy.

Contrary to photons, atoms couple to inertial forces [13]. This feature prompted physicists to build atom interferometers which are sensitive to rotations and accelerations. Similarly to optical interferometers, their atomic counterparts measure the phase difference between matter waves travelling along different paths. In most of the atom interferometers, atoms are ejected upwards and interfere while falling in free flight. The use of atoms in interferometric apparatuses enabled to measure gravitational acceleration [14], Earth's rotation rate [15], atomic polarisability [16], physical constants [17] with extraordinary precision, and with the help of Ramsey interferometry [18] a frequency standard for atomic clocks has been determined [19].

In quantum mechanics, there is no hermitian phase operator [20], thus phase, similarly to time, is only a parameter. To find the phase, one has to use the theory of estimation. This process typically involves selection of a certain measurable quantity (in the language of quantum mechanics: an observable) which depends in on the phase and subsequent decryption of the gathered measurement results. The primary role of interferometry is to specify an initial state, interferometer (transformation of

the initial state), an observable (for instance the number of particles measured at each of the output ports of an interferometer), and an estimator in a way that enables the inference of the unknown parameter with the lowest possible uncertainty. A significant limitation is the time of the experiment and available resources, *i.e.*, photons or atoms which are injected in the interferometer. In particular, systems with a too large number of particles are more susceptible to decoherence, a process leading to loss of quantum features [21].

The sensitivity of phase estimation in two-mode interferometry—when two modes are interfered as in the case of the Mach-Zehnder interferometer—exploiting classical states is limited by the so-called shot-noise limit

$$\Delta\theta_{SNL} = 1/\sqrt{N \cdot m},$$

where N is the mean number of particles in the initial state, m is the number of measurement repetitions performed on the copy of the initial state, and θ is the phase. For a long time, the shot-noise limit was considered to be the fundamental bound on the precision of estimating an unknown parameter. In 1981, to overcome this limitation, Carlton Caves proposed to inject a squeezed vacuum state into one port of the interferometer [22]. This concept triggered search for physical systems that would be capable of surpassing the classical limit of precision [23–27], but only in few of them a connection between some non-classical correlations and sensitivity improvement has been spotted [28–30]. A necessary condition to overcome the shot-noise limit is the use of non-classical, in terms of correlations, particles in the interferometer's input ports [1, 3, 31, 32]. Non-classical correlations, or, to be more specific, quantum entanglement is capable of improving the interferometer's sensitivity beyond the shot-noise limit up to the Heisenberg limit [33]

$$\Delta\theta_{\mathrm{HL}} = 1/\sqrt{N^2 \cdot m}.$$

This theoretical result is a subject of intense experimental activity with photons [34–37], trapped ions [38, 39], cold atoms [40–42], ultra-cold atoms [43–45], and Bose-Einstein condensates [46–48].

In the previous set, Bose-Einstein condensates deserve a separate paragraph. These macroscopic many-body quantum systems posses a fundamental feature which photons lack. Namely, the interaction among bosons in a condensate leads to natural nonlinearities which are a powerful tool to create non-classical states such as spin-squeezed states [29, 48, 49] and Schrödinger cats [46, 50]. These many-body entangled states [51] are generated inside condensates in analogy to non-classical states of light created by the non-linear Kerr effect. Moreover, a remarkable feature of condensate is the possibility of tuning the interactions by external magnetic field exploiting Feshbach resonances [52]. Furthermore, the spatial control over a condensate is an additional tool by which the interactions can be modified. By manipulating the trapping potential, one can change the density and system dimension and thus alter the effective two-body interaction strength (scattering length) [53].

0.2 The importance of conducted research

The importance of research conducted in this dissertation is twofold. First, as demonstrated by the Michelson-Morley experiment and the recent detection of gravitational waves, the breakthroughs in physics are often the result of increased sensitivity of measuring instruments. By constructing more accurate measuring devices, we are able not only to discover new physical phenomena but also to determine the limits of the already existing theoretical models or even refute them. Combining quantum metrology with interferometry, in particular, the use of entangled states may lead in future to the emergence of a new generation of extremely precise instruments based on the foundations of quantum mechanics. Theoretically, such devices would allow for observations of gravitational waves in an average-sized laboratory, as opposed to the currently used 4 km long interferometer [12]. Second, thanks to its versatility, interferometry offers many approaches that can examine the most fundamental aspects of quantum mechanics. One of the many examples is the ability to study such an extraordinary phenomenon as entanglement, in such a simple device as the Mach-Zehnder interferometer (see Figure 1).

Interferometry is the field of physics that may provide the most accurate measurements. Consequently, there is a need for new ideas and techniques to further increase the sensitivity of interferometers. The majority of current atomic and optical interferometers are based on linear elements such as beam-splitters and phase-shifting elements, and linear transformations when considering atoms in Bose-Einstein condensates. As described already in the previous Section 0.1, the classical limit of precision can only be exceeded if entangled states are harnessed. Experiments that have been conducted in recent years with the use of such states of atoms [54–61] and photons [36, 62–66] were aimed only to display a possibility to measure a certain parameter with a precision exceeding the shot-noise limit, or, in other words, they were proofs of principle. The main reason for such a state of affairs is the decoherence and experimental noise limiting the creation and use of entangled states [67–69]. Therefore, it is important to look for new methods of creating these states and to search for alternative interferometric protocols.

Part I

Theoretical Background

Chapter 1

Quantum Optics

Quantum optics is a branch of physics which studies the nature of quantised light (photons) and its interaction with matter. Its beginnings reach the explanation of the blackbody radiation spectrum by Planck in 1899. He assumed that light is emitted in portions of energy [70]. Initially, this explanation was not accepted by the scientific community, because it stood in stark contrast with what was known at that time. Even Max Planck himself did not attribute any physical significance to his hypothesis but instead proposed it as a mathematical trick that enabled him to derive a single expression for the blackbody spectrum [71]. Five years had to pass until the new light was shed on the Planck's heuristic assumption of abstract elements of energy. In 1905, Einstein managed to explain the photoelectric effect by proposing a model and formula whereby light was emitted, absorbed, and propagated in free space in energy quanta [72]. Later on, Niels Bohr showed that the Planck's hypothesis agreed with his model of an atom, and with the emission spectrum of hydrogen. The understanding of the light-matter interaction following these discoveries set foundations for quantum mechanics.

After Maiman built the first laser in 1960 [73], the study of design, principles, and application of these new devices became an important field. The theory underlying the laser's principles was studied with more emphasis on the quantum properties of light, and the term quantum optics became ubiquitous. Sudarshan [74], Glauber [75, 76], and Mandel [77] harnessed quantum theory to describe the electromagnetic radiation which shed completely new *nomen omen* light on the theory of electromagnetic field, and led to the concept of a coherent state of light being the most classic out of the quantum states. In 1977, a single-photon emitter was reported by Kimble [78] which was another evidence for the Planck's hypothesis. Following this, new quantum states of light with characteristics reaching far beyond the scope of classical physics, such as squeezed light [79], were discovered.

Contents

1.1 Coherent state of light

In quantum optics, the concept of a coherent state refers to a state of quantised electromagnetic wave and is often regarded as the most classical quantum state. It was first derived by Erwin Schrödinger in 1926 [80] as a minimum uncertainty Gaussian

wavepacket with respect to the position $\hat{x}$ and momentum $\hat{p}$, and therefore it saturates the Heisenberg uncertainty principle

$$\Delta\hat{x}\Delta\hat{p} = \frac{\hbar}{2}.$$

When inserted into the quantum linear harmonic oscillator, its time evolution is focused along the classical trajectories. Moreover, the expectation value of the electric field has the form of the classical expression, the fluctuations of the electric field are the same as for the vacuum state, the relative uncertainty for the photon number and the phase uncertainty decreases with the increasing average number of photons. However, despite these classical-like features, they are still fully quantum states.

A coherent state $|\alpha\rangle$ is defined as an eigenstate of the annihilation operator $\hat{a}$ with a complex eigenvalue α

$$\hat{a}\,|\alpha\rangle = \alpha\,|\alpha\rangle\,.$$

In the literature, the state $|\alpha\rangle$ is called a canonical coherent state to distinguish it from other types of coherent states, *e.g.*, a coherent spin state $|\theta,\phi\rangle$, which is introduced in the next Chapter. Nonetheless, throughout this dissertation, we call $|\alpha\rangle$ simply a coherent state.

Physically, formula 1.1 means that the annihilation of a photon, or generally field excitation, does not change the state. This state can be expressed in the Fock basis in the following form

$$|\alpha\rangle = e^{-\frac{|\alpha|^2}{2}} \sum_{n=0}^{\infty} \frac{\alpha^n}{\sqrt{n!}}\,|n\rangle\,,$$

where $|n\rangle$ is the a vector from the Fock space representing n-photon state. The probability of measuring n photons is then

$$P(n) = |\langle n|\alpha\rangle|^2 = e^{-|\alpha|^2}\frac{|\alpha|^{2n}}{n!},$$

which corresponds to the Poissonian distribution with average $|\alpha|^2$. Examples of distributions can be seen in Figure 1.1.

Mathematically, coherent states can be obtained by letting the unitary displacement operator $\hat{D}(\alpha)$ operate on the vacuum. This can be seen by manipulating formula 1.1 in the following way

$$\begin{aligned}|\alpha\rangle &= e^{-\frac{|\alpha|^2}{2}} \sum_{n=0}^{\infty} \frac{\alpha^n}{\sqrt{n!}}\,|n\rangle = e^{-\frac{|\alpha|^2}{2}} \sum_{n=0}^{\infty} \frac{(\alpha\hat{a}^\dagger)^n}{n!}\,|0\rangle = e^{-\frac{|\alpha|^2}{2}} e^{\alpha\hat{a}^\dagger}\,|0\rangle \\ &= e^{-\frac{|\alpha|^2}{2}} e^{\alpha\hat{a}^\dagger} e^{-\alpha^*\hat{a}}\,|0\rangle = e^{\alpha\hat{a}^\dagger - \alpha^*\hat{a}}\,|0\rangle = \hat{D}(\alpha)\,|0\rangle\,,\end{aligned}$$

where we have used the fact that $e^{-\alpha^*\hat{a}}\,|0\rangle = |0\rangle$ and the Baker-Campbell-Hausdorff formula [81]

$$e^{\hat{A}+\hat{B}} = e^{\hat{A}}e^{\hat{B}}e^{-\frac{1}{2}\left[\hat{A},\hat{B}\right]} = e^{\hat{B}}e^{\hat{A}}e^{\frac{1}{2}\left[\hat{A},\hat{B}\right]}.$$

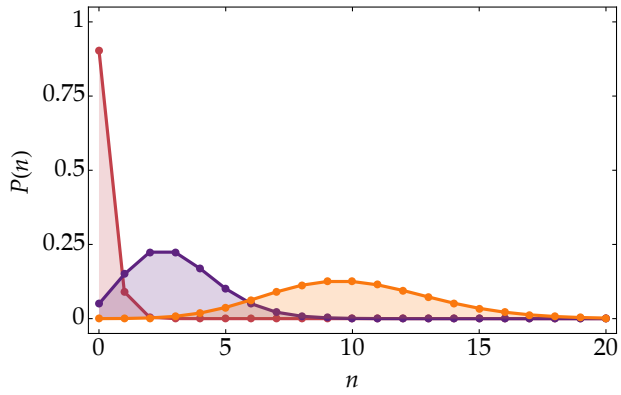

FIGURE 1.1: Probability distribution of measuring n photons for 3 different coherent states. The red, blue, and green lines correspond to a coherent state with α equal to $\sqrt{0.1}$, $\sqrt{3}$, and $\sqrt{10}$, respectively. For $|\alpha| \gg 1$ the distribution tends to a Gaussian distribution.

Coherent states are not orthogonal, the overlap between coherent states $|\alpha\rangle$ and $|\beta\rangle$ is

$$\langle\beta|\alpha\rangle = e^{-\frac{|\beta|^2}{2}} e^{-\frac{|\alpha|^2}{2}} \sum_{m=0}^{\infty}\sum_{n=0}^{\infty} \frac{\beta^{*m}\alpha^n}{\sqrt{m!n!}} \langle m|n\rangle = e^{-\frac{|\beta|^2}{2}} e^{-\frac{|\alpha|^2}{2}} \sum_{n=0}^{\infty} \frac{(\beta^*\alpha)^n}{n!}$$
$$= e^{-\frac{|\beta|^2}{2}} e^{-\frac{|\alpha|^2}{2}} e^{\beta^*\alpha} = e^{\frac{1}{2}(\beta^*\alpha - \beta\alpha^*)} e^{-\frac{1}{2}|\beta-\alpha|^2}.$$

The first factor is only a phase, and thus

$$|\langle\beta|\alpha\rangle|^2 = e^{-|\beta-\alpha|^2} \neq 0.$$

One would say, however, that if $|\beta - \alpha|^2 \gg 1$, the states are distinguishable (orthogonal). Although, as we just showed, coherent states are not orthogonal, they constitute an overcomplete basis. The completeness relation for the coherent state reads

$$\frac{1}{\pi}\int \mathrm{d}\,\alpha\, |\alpha\rangle\langle\alpha| = \hat{I},$$

and thus any state can be decomposed on the set of coherent states:

$$|\psi\rangle = \frac{1}{\pi}\int \mathrm{d}\alpha\ |\alpha\rangle\langle\alpha|\psi\rangle = \frac{1}{\pi}\int \mathrm{d}\alpha\, \psi_\alpha |\alpha\rangle,$$

where $\psi_\alpha = \langle\alpha|\psi\rangle$. The above Equation is the foundation of the Sudarshan-Glauber P representation [74] which we will not elaborate on in this dissertation. More about coherent states, Sudarshan-Glauber P representation, and other phase-space pictures of quantum states can be found in any introductory quantum optics textbook, *e.g.* in Reference [82].

1.2 Husimi Q representation

The Husimi Q representation (also known as the Q function) is a quasiprobability distribution introduced by Husimi in 1940 [83] used to depict the phase space distribution of quantum states. The Husimi Q function is relatively easy to calculate. For a general state represented by a density matrix $\hat{\rho}$, it can be calculated according to the formula

$$Q_{\hat{\rho}}(\alpha) = \frac{1}{\pi} \langle \alpha | \hat{\rho} | \alpha \rangle = \frac{1}{\pi} \mathrm{Tr} \left[\hat{\rho} \left| \alpha \right\rangle \left\langle \alpha \right| \right].$$

One of its simplest example is the Husimi Q function of a coherent state, presented in Figure 1.2.

$$Q_{|\beta\rangle}(\alpha) = \frac{1}{\pi} e^{-|\beta - \alpha|^2},$$

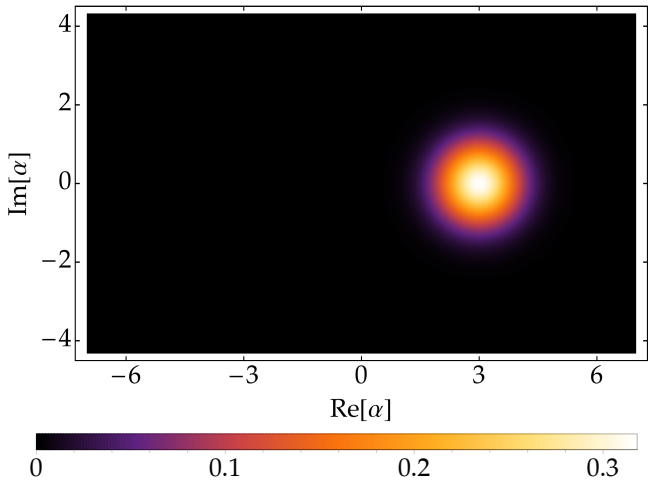

FIGURE 1.2: Husimi Q representation for a coherent state $|\beta\rangle$ with $\beta = 3$. Since the coherent state can be expressed as a displaced vacuum $\hat{D}(\alpha) |0\rangle = |\alpha\rangle$, the vacuum state would correspond to a similar picture with origin simply at $\alpha = 0$ point. Again, since the displacement operator only moves the state from the origin, the phase uncertainty, or the angular size, decreases with the increase of displacement.

Another neat examples are the Husimi Q function of a Fock state (Figure 1.3), which is simply

$$Q_{|n\rangle}(\alpha) = \frac{1}{\pi n!} e^{-|\alpha|^2} |\alpha|^{2n},$$

and the Husimi Q function of a thermal state [84]

$$Q_{\hat{\rho}_{th}}(\alpha) = \frac{1}{\pi} \langle \alpha | \frac{1}{1+\bar{n}} \sum_{n=0}^{\infty} \left(\frac{\bar{n}}{1+\bar{n}} \right)^n |n\rangle \langle n|\alpha\rangle = \frac{1}{\pi(1+\bar{n})} \exp\left(-\frac{|\alpha|^2}{1+\bar{n}} \right).$$

Husimi Q function is normalised to unity

$$\int \mathrm{d}\alpha \, Q_{|\psi\rangle}(\alpha) = 1,$$

is also non-negative, and bounded

$$0 \leq Q_{|\psi\rangle}(\alpha) \leq \frac{1}{\pi}.$$

Despite this fact, Husimi Q distribution does not represent the probability. Coherent states are not orthogonal, and thus it is a quasiprobability distribution.

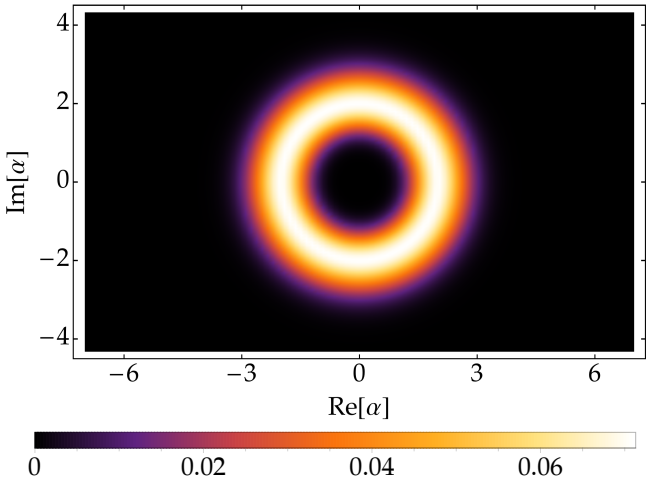

FIGURE 1.3: Husimi Q representation for a Fock state with $n = 4$. The higher the Fock state, the larger the radius of the ring.

The Husimi Q function can also be expressed as

$$Q_{|\psi\rangle}(\alpha) = \frac{2}{\pi} \int \mathrm{d}\beta \, W_{|\psi\rangle}(\beta) e^{-2|\alpha-\beta|^2},$$

where $W_{|\psi\rangle}(\beta)$ is the Wigner quasiprobability distribution, which is defined in Section 1.3, and therefore the Husimi Q function provides a mathematically equivalent phase-space description of quantum mechanics to that provided by the Wigner distribution. However, the Wigner function has one major advantage over the Husimi Q function. Namely, a certain class of non-classical states can be easily identified, and pure states can be distinguished (visually) from incoherent mixtures, *e.g.*, a superposition of coherent states with opposite amplitudes cannot be distinguished from an incoherent mixture of two coherent states with opposite amplitudes. On the other hand, the Husimi Q distribution function is found to be a better representation than the Wigner distribution function when studying chaotic systems [85–87].

1.3 Wigner function

The Wigner function also called the Wigner quasiprobability distribution was introduced by Wigner in 1932 [88]. The Wigner function of an arbitrary state can be

calculated from its density matrix according to

$$W_{\hat{\rho}}(q,p) = \frac{1}{2\pi\hbar}\int_{-\infty}^{\infty} \mathrm{d}x\ \langle q + \frac{x}{2}|\hat{\rho}|q - \frac{x}{2}\rangle\, e^{ipx/\hbar},$$

where $|q \pm \frac{x}{2}\rangle$ are eigenstates of position operator x. For a pure state $|\psi\rangle$, we obtain

$$W_{|\psi\rangle}(q,p) = \frac{1}{2\pi\hbar}\int_{-\infty}^{\infty} \mathrm{d}x\, \psi^*\left(q - \frac{x}{2}\right)\psi\left(q + \frac{x}{2}\right) e^{ipx/\hbar},$$

where $\psi^*\left(q - \frac{x}{2}\right) = \langle\psi|q - \frac{x}{2}\rangle$ and $\psi\left(q + \frac{x}{2}\right) = \langle q + \frac{x}{2}|\psi\rangle$. Integration of this formula with respect to the momentum p yields

$$\begin{aligned}\int_{-\infty}^{\infty} \mathrm{d}p\, W_{|\psi\rangle}(q,p) &= \frac{1}{2\pi\hbar}\int_{-\infty}^{\infty}\mathrm{d}p\int_{-\infty}^{\infty}\mathrm{d}x\,\psi^*\left(q - \frac{x}{2}\right)\psi\left(q + \frac{x}{2}\right)e^{ipx/\hbar}\\ &= \int_{-\infty}^{\infty}\mathrm{d}x\,\psi^*\left(q - \frac{x}{2}\right)\psi\left(q + \frac{x}{2}\right)\delta\left(x\right) = |\psi(q)|^2,\end{aligned}$$

where $\delta(x) = \frac{1}{2\pi\hbar}\int_{-\infty}^{\infty}\mathrm{d}p e^{ipx/\hbar}$ is the Dirac's delta function, and $\psi(q)$ is the wavefunction in position representation. Similarly, integration with respect to the position q yields

$$\int_{-\infty}^{\infty}\mathrm{d}q\, W_{|\psi\rangle}(q,p) = |\psi(p)|^2,$$

where $\psi(p)$ is the wavefunction in the momentum representation. Equations 1.3 and 1.3 are probability densities but the Wigner function itself, likewise the Husimi Q function, is not a proper probability density (for instance, it can take negative values for non-classical states). Alternatively, to calculate the Wigner function of a coherent state $|\alpha\rangle$, we would have to first find the position representation of a coherent state $\psi_\alpha(x) = \langle x|\alpha\rangle$. This can be done, but for the purpose of this dissertation it is more elegant to introduce the Wigner characteristic function [89] defined as

$$C_{\mathrm{W}} = \mathrm{Tr}\left[\hat{\rho}e^{\lambda\hat{a}^\dagger - \lambda^*\hat{a}}\right] = \mathrm{Tr}\left[\hat{\rho}\hat{D}(\lambda)\right],$$

and to write the Wigner function as

$$W_{\hat{\rho}}(\alpha) = \frac{1}{\pi^2}\int \mathrm{d}\lambda\ \exp\left(\lambda^*\alpha - \lambda\alpha^*\right) C_{\mathrm{W}}.$$

Since C_W can be understood as an average value of $\hat{D}(\alpha)$ on a state $\hat{\rho}$, for a pure state $|\psi\rangle$ we have

$$\begin{aligned}W_{|\psi\rangle}(\alpha) &= \frac{1}{\pi^2}\int \mathrm{d}\lambda\ \exp\left(\lambda^*\alpha - \lambda\alpha^*\right)\langle\psi|\hat{D}(\lambda)|\psi\rangle\\ &= \frac{1}{\pi^2}\int \mathrm{d}\lambda\ \langle\psi|\exp\left(\lambda^*\alpha - \lambda\alpha^*\right)\exp\left(\lambda\hat{a}^\dagger - \lambda^*\hat{a}\right)|\psi\rangle\\ &= \frac{1}{\pi^2}\int \mathrm{d}\lambda\ \langle\psi|\exp\left(\lambda^*\left(\alpha - \hat{a}\right) - \lambda\left(\alpha^* - \hat{a}^\dagger\right)\right)|\psi\rangle\end{aligned}$$

Therefore, the Wigner function of a coherent state $|\beta\rangle$ (depicted in Figure 1.4) is

$$W_{|\beta\rangle}(\alpha) = \frac{2}{\pi}e^{-2|\alpha-\beta|^2},$$

a very similar expression to the Husimi Q function of a coherent state from Equation 1.2, which can be retrieved following Formula 1.2.

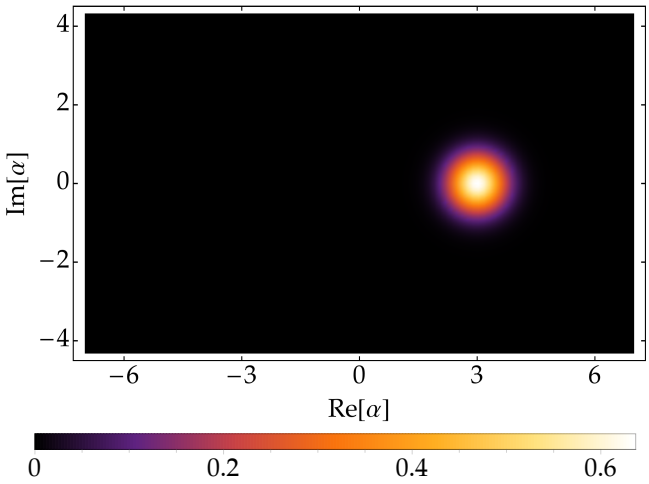

FIGURE 1.4: The Wigner function of a coherent state $|\beta\rangle$ with $\beta = 3$. For comparison with the Husimi Q function, see Figure 1.2

As can be seen from Figure 1.4, the Wigner function of a coherent state is very similar to its Husimi Q function. Let us now check whether this similarity also applies to the Fock state. For a Fock state $|n\rangle$, we have

$$W_{|n\rangle}(\alpha) = \frac{2}{\pi}(-1)^n L_n(4|\alpha|^2)e^{-2|\alpha|^2},$$

where $L_n(\zeta)$ is the Laguerre polynomial [90]. This function is very different from the Husimi Q function of a Fock state, which also manifests itself in its visual representation, presented in Figure 1.5 and 1.6. A conspicuous feature of Wigner function of a Fock state is its negativity, which, as already mentioned, is a signature of non-classicality. Here, we would like to stress that this is not that surprising as it may seem at a first glance. Fock states are states with well-defined number of particles, and the price that has to be paid for that is a complete randomness of phase. This interplay between the conjugate variables can be also regarded as a signature of non-classicality, which will become apparent when we focus on the squeezed states. The Wigner function of these states is positive, and yet they can be extremely non-classical. Therefore, the negativity of the Wigner function is not a necessary condition for non-classicality. Another important feature of the Wigner function is the possibility of its reconstruction from the experimental data, a procedure known as quantum-state tomography [91–93].

1.4 Squeezed state of light

Originally, squeezed states of light were introduced as generalised minimum uncertainty states. Their features were discovered independently by several groups and have been described variously as new coherent states [94], ideal squeezed states [22], two-photon coherent states [95], and pulsating wave packets [96]. The first experimentally generated squeezed light was reported by Slusher [97].

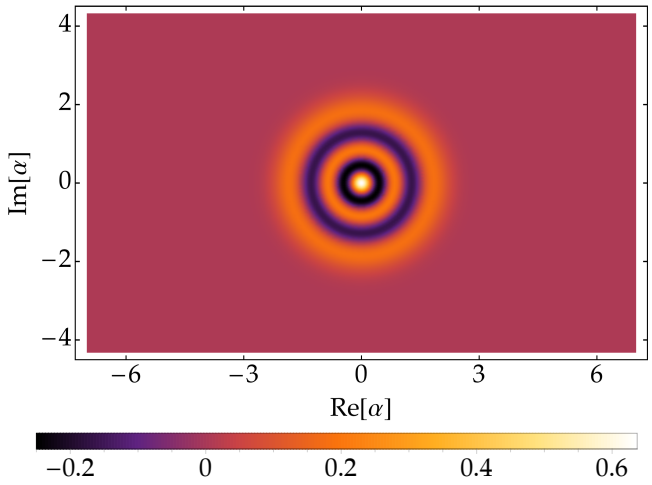

FIGURE 1.5: The Wigner function of a Fock state with $n = 4$. For comparison to the Husimi Q function, see Figure 1.3.

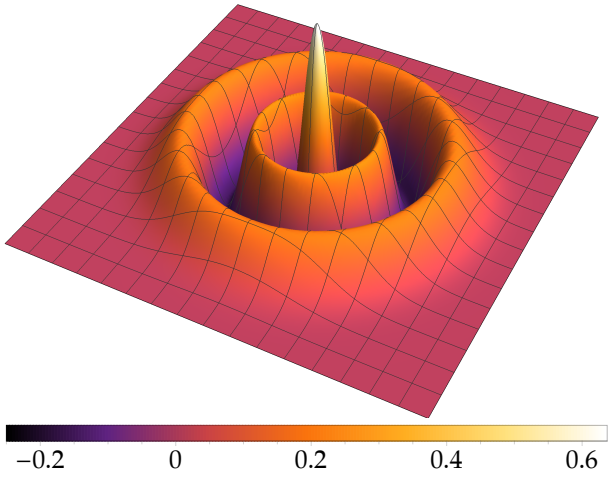

FIGURE 1.6: The Wigner function of a Fock state with $n = 4$. The Figure presents a 3D zoom on the centre of the Wigner function from the Figure above. For comparison to the Husimi Q function, see Figure 1.3.

To introduce the concept of squeezing, we first need to have a closer look at fluctuations in some observable $\hat{O}$, which are defined by

$$\Delta^2\hat{O} \equiv \langle\hat{O}^2\rangle - \langle\hat{O}\rangle^2,$$

where $\langle\hat{O}\rangle = \mathrm{Tr}\left[\hat{\rho}\hat{O}\right]$. The variances of two observable quantities $\hat{A}$ and $\hat{B}$ satisfy the uncertainty relation

$$\Delta^2\hat{A}\Delta^2\hat{B} \geq \frac{1}{4}|\langle\left[\hat{A},\hat{B}\right]\rangle|^2,$$

and if the equality holds, the state $\hat{\rho}$ is said to be a minimum uncertainty state. A straightforward calculation shows that the vacuum state $|0\rangle$ is a minimum-uncertainty

state with respect to the operators $\hat{p}$ and $\hat{x}$ for which

$$\Delta^2\hat{p}\Delta^2\hat{x} = \frac{\hbar^2}{4}.$$

Since $\hat{p}$ and $\hat{x}$ have different units, it is convenient to introduce the quadrature operators

$$\hat{X} = \left(\frac{\omega}{2\hbar}\right)^{1/2}\hat{x} = \frac{1}{2}\left(\hat{a} + \hat{a}^\dagger\right)$$

and

$$\hat{P} = (2\hbar\omega)^{-1/2}\,\hat{p} = \frac{1}{2i}\left(\hat{a} - \hat{a}^\dagger\right),$$

where ω is the frequency of single-mode field. These quadratures may be linked with the coordinates of the Husimi Q function. For a coherent state, we obtain

$$\langle\hat{X}\rangle = \mathrm{Re}\,[\alpha] \quad \text{and} \quad \langle\hat{P}\rangle = \mathrm{Im}\,[\alpha]\,.$$

The quadrature operators satisfy the commutation relation

$$\left[\hat{X}, \hat{P}\right] = \frac{i}{2}.$$

For a coherent state, the variances of the quadratures are

$$\Delta^2\hat{X} = \Delta^2\hat{P} = \frac{1}{4}$$

and because of that they are sometimes also considered as squeezed states. In this dissertation, however, a state is considered to be squeezed if one of its quadratures is less than $1/2$. For this reason, it is convenient to introduce a general quadrature operator

$$\hat{Q}(\theta) = \frac{1}{2}\left(\hat{a}e^{-i\theta} + \hat{a}^\dagger e^{i\theta}\right),$$

where for $\theta = 0$ we retain the $\hat{X}$ quadrature, and for $\theta = \pi/2$ we retain the $\hat{P}$ quadrature. Now, a state is said to be squeezed if there exists θ such that

$$\Delta^2\hat{Q}(\theta) < \frac{1}{4}.$$

This kind of squeezing is often referred to as the quadrature squeezing, but the notion of squeezing is more general; for example, one can postulate a somewhat artificial commutation relation

$$\left[\hat{n}, \hat{\phi}\right] = i,$$

where $\hat{n} = \hat{a}^\dagger\hat{a}$ is the photon number operator and $\hat{\phi}$ is the phase operator. The problem with this relation is the lack of hermitian phase operator $\hat{\phi}$, but in the regime of large average photon number it leads to the heuristically correct number-phase

uncertainty relation [98]

$$\Delta^2\hat{n}\Delta^2\hat{\phi} \geq \frac{1}{4}.$$

For a coherent state $|\alpha\rangle$, for which $\Delta^2\hat{n} = |\alpha|^2$, it can be shown that $\Delta^2\phi = 1/4|\alpha|^2$, and thus this uncertainty relation can be saturated.

Another important type of squeezing is the number squeezing. A state is said to be number squeezed if the so-called Mandel's Q-parameter [99]

$$Q = \frac{\Delta^2\hat{n}}{\langle\hat{n}\rangle} - 1$$

is less than 0. The extreme case of a number squeezed state is the Fock state for which the Mandel's Q-parameter is equal to -1. For a state with Q in the range $-1 \leq Q < 0$ the statistics are sub-Poissonian, and if $Q > 0$ they are super-Poissonian. For a coherent state, we obtain $Q = 0$.

Let us now consider methods of creating squeezed states. One of the most common ways is via the degenerate parametric down-conversion [100], where a certain kind of nonlinear medium is pumped by a field of frequency ω_p and some photons of that field are converted into pairs of identical photons of frequency $\omega = \omega_p/2$ each. Mathematically, this process corresponds to a squeeze operator

$$\hat{S}(\xi) = \exp\left[\frac{1}{2}\left(\xi^*\hat{a}^2 - \xi\hat{a}^{\dagger 2}\right)\right],$$

where $\xi = re^{i\theta}$ with $0 \leq r < \infty$ being the squeeze parameter and $0 \leq \theta \leq 2\pi$ indicates the direction of squeezing.

The most general squeezed state can be obtained by squeezing the vacuum state and its subsequent displacement:

$$|\alpha, \xi\rangle = \hat{D}(\alpha)\hat{S}(\xi)\,|0\rangle\,.$$

For a squeezed state $|\alpha, \xi\rangle$ the quadratures are

$$\Delta^2\hat{X} = \frac{1}{4}\left(\cosh^2 r + \sinh^2 r - 2\sinh r\cosh r\cos\theta\right)$$

and

$$\Delta^2\hat{P} = \frac{1}{4}\left(\cosh^2 r + \sinh^2 r + 2\sinh r\cosh r\cos\theta\right).$$

For $\theta = 0$, we obtain squeezing along the real axis (and anti-squeezing along the imaginary axis)

$$\Delta^2\hat{X} = \frac{1}{4}e^{2r}$$
$$\Delta^2\hat{P} = \frac{1}{4}e^{-2r},$$

and for $\theta = \pi/2$, we obtain squeezing along the imaginary axis (and anti-squeezing along the real axis). Note that squeezed states need not, and usually do not, saturate the uncertainty relation.

In order to gain a further insight into the nature of squeezed states, we can decompose $|\alpha, \xi\rangle$ in the basis of Fock states

$$\begin{aligned}|\alpha, \xi\rangle =& \frac{1}{\sqrt{\cosh r}} \exp\left[-\frac{1}{2}|\alpha|^2 - \frac{1}{2}\alpha^{*2} e^{i\theta} \tanh r\right] \\ & \times \sum_{n=0}^{\infty} \frac{\left(\frac{1}{2} e^{i\theta} \tanh r\right)^{n/2}}{\sqrt{n!}} H_n\left(\gamma \left(e^{i\theta} \sinh(2r)\right)^{-1/2}\right) |n\rangle ,\end{aligned}$$

where $H_n(x)$ are the Hermite polynomials [101], and $\gamma = \alpha \cosh r + \alpha^* e^{i\theta} \sinh r$, and calculate its Husimi Q function (depicted in Figure 1.7)

$$\begin{aligned}Q_{|\alpha,\xi\rangle}(\beta) &= \frac{1}{\pi} |\langle \beta | \alpha, \xi \rangle|^2 \\ &= \frac{1}{\pi \cosh r} \exp\Bigg[- |\alpha - \beta|^2 \\ &\qquad - \frac{\tanh r}{2} \left(e^{i\theta} (\alpha^* - \beta^*)^2 + e^{-i\theta} (\alpha - \beta)^2 \right) \Bigg],\end{aligned}$$

and also calculate its Wigner function (depicted in Figure 1.8)

$$\begin{aligned}W_{|\alpha,\xi\rangle}(\beta) =& \frac{2}{\pi} \exp\Bigg[- 2 \left(\mathrm{Re}\left[\beta - \alpha\right] \cos\left(\frac{\theta}{2}\right) + \mathrm{Im}\left[\beta - \alpha\right] \sin\left(\frac{\theta}{2}\right) \right)^2 e^{2r} \\ & - 2 \left(\mathrm{Im}\left[\beta - \alpha\right] \cos\left(\frac{\theta}{2}\right) - \mathrm{Re}\left[\beta - \alpha\right] \sin\left(\frac{\theta}{2}\right) \right)^2 e^{-2r} \Bigg].\end{aligned}$$

Note that the Wigner function of a squeezed state $|\alpha, \xi\rangle$ is non-negative. It can be shown that squeezed states of that form, are the only pure quantum states whose Wigner function is non-negative [102]. From Figures 1.7 and 1.8 it is obvious why this kind of states are called squeezed. The Husimi Q distribution and the Wigner distribution of the same squeezed state are very similar except the Wigner distribution is more squeezed.

The average number of photons in a squeezed state $|\alpha, \xi\rangle$ is

$$\langle \hat{n} \rangle = |\alpha|^2 + \sinh^2 r,$$

which means that the squeezed vacuum $|0, \xi\rangle$ is a state with non-zero number of photons. This superficial paradox disappears when we evoke the discussion about the generation of squeezed states and look again at Equation 1.4. A typical distribution of photons for the squeezed vacuum is given in Figure 1.9.

Some states can be simultaneously quadrature squeezed and number squeezed. It can be shown that for a squeezed state $|\xi\rangle$, we obtain

$$\Delta^2 \hat{n} = |\alpha \cosh r - \alpha^* e^{i\theta} \sinh r|^2 + 2 \sinh^2 r \cosh^2 r.$$

With a proper choice of α and ξ, *e.g.* by making them real, we get

$$\Delta^2 \hat{n} = |\alpha|^2 e^{-2r} + 2 \sinh^2 r \cosh^2 r,$$

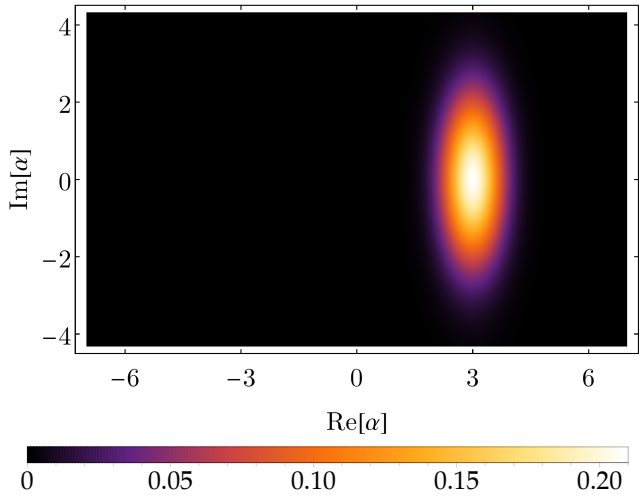

FIGURE 1.7: The Husimi Q function of a squeezed state $|\beta, \xi\rangle$ with $\beta = 3$ and $\xi \equiv re^{i\theta} = 1$. The squeezing occurs along $\hat{X}$ quadrature, and the anti-squeezing occurs along $\hat{P}$ quadrature. In general, a state can be squeezed along an arbitrary quadrature $\hat{Q}(\vartheta)$ by properly choosing the phase of the squeezing parameter ξ.

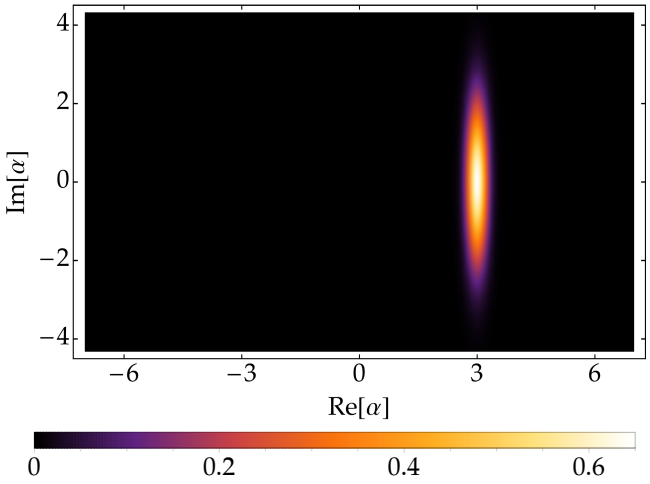

FIGURE 1.8: The Wigner function of the same state as in Figure 1.7. The distributions are similar except the Wigner function is narrower along the squeezed quadrature. The family of squeezed states $|\beta, \xi\rangle$, including a coherent state $|\beta, 0\rangle$, the vacuum $|0, 0\rangle$, and a squeezed vacuum $|0, \xi\rangle$, is the only kind of pure states whose Wigner function is non-negative.

which exhibits number squeezing for large $|\alpha|^2$ and small r such that $\sinh r \approx 0$ and $\langle \hat{n} \rangle \approx |\alpha|^2$:

$$\Delta^2 \hat{n} \approx \langle \hat{n} \rangle e^{-2r},$$

and thus the Mandel's Q parameter is less than 0. The first convincing observation of sub-Poissonian statistics (number squeezing) was reported in 1983 by Short and

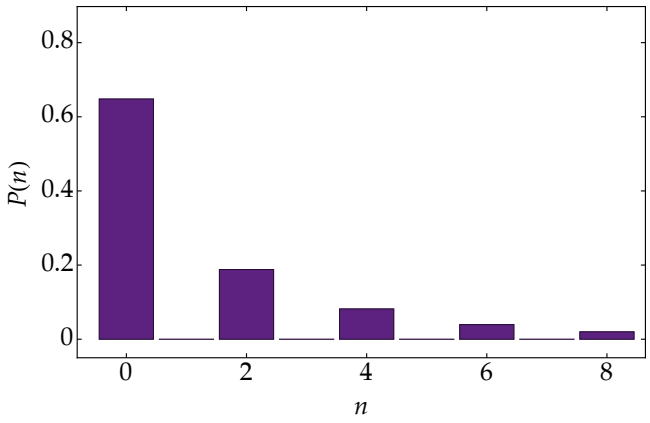

FIGURE 1.9: Histogram for the photon number distribution for squeezed vacuum state. The characteristic appearance of the distribution reflects how the squeezed vacuum state is generated by Equation 1.4 with multiple of 2 photon excitations.

Mandel [103]. The squeezed states $|\alpha, \xi\rangle$ are only one of the examples of possible squeezed states. As we already mentioned, some states can exhibit both quadrature and number squeezing; some may exhibit quadrature squeezing but not number squeezing or *vice versa*. We have only described the iceberg tip of squeezing. Other methods of generating squeezed states include two-mode squeezing [104], high-order squeezing [105], broadband squeezing [106], *etc.* Squeezed states do not exhaust all possibilities of non-classical states of light. It is even possible to have non-classical states that are neither quadrature nor number squeezed. One example of such states is the Schrödinger's cat state which is the subject of the next Subsection.

1.5 Schrödinger's cat state

Schrödinger's cat states are important type of non-classical single-mode states [107]. A Schrödinger's cat state is a superposition of two coherent states with equal amplitudes but shifted in phase by π:

$$|\psi\rangle = \mathcal{N}\left(|\alpha\rangle + e^{i\theta}\,|-\alpha\rangle\right),$$

where the normalisation factor $\mathcal{N}$ is

$$\mathcal{N} = 1/\sqrt{2 + 2\exp\left(-2\alpha^2\right)\cos\theta}.$$

For large $|\alpha|$, we obtain a superposition of two macroscopical and distinguishable states $|\alpha\rangle$ and $|-\alpha\rangle$. The name of this state comes from very renown thought experiment by Erwin Schrödinger [108], of which purpose was to criticise the Copenhagen interpretation of quantum mechanics. Schrödinger wrote [109]:

> One can even set up quite ridiculous cases. A cat is penned up in a steel chamber, along with the following device (which must be secured against direct interference by the cat): in a Geiger counter there is a tiny bit of radioactive substance, so small, that perhaps in the course of the hour one of the atoms decays, but also, with equal probability, perhaps none;

> if it happens, the counter tube discharges and through a relay releases a hammer which shatters a small flask of hydrocyanic acid. If one has left this entire system to itself for an hour, one would say that the cat still lives if meanwhile no atom has decayed. The psi-function of the entire system would express this by having in it the living and dead cat (pardon the expression) mixed or smeared out in equal parts.
>
> It is typical of these cases that an indeterminacy originally restricted to the atomic domain becomes transformed into macroscopic indeterminacy, which can then be resolved by direct observation. That prevents us from so naively accepting as valid a "blurred model" for representing reality. In itself it would not embody anything unclear or contradictory. There is a difference between a shaky or out-of-focus photograph and a snapshot of clouds and fog banks.

In fact, this seemingly simple thought experiment poses a very profound question: what is the mechanism by which certain superpositions (not only macroscopic) are not observable? We are not going to focus on this question in this dissertation, but for further insight into this topic, we recommend Reference [110].

Depending on the choice of the relative phase θ, we can distinguish three important cat states [111, 112]. For $\theta = 0$, we obtain the even cat state

$$|\psi_e\rangle = (|\alpha\rangle + |-\alpha\rangle) / \sqrt{2 + 2\exp(-2\alpha^2)},$$

for $\theta = \pi$, we obtain the odd cat state

$$|\psi_o\rangle = (|\alpha\rangle - |-\alpha\rangle) / \sqrt{2 - 2\exp(-2\alpha^2)},$$

and for $\theta = \pi/2$, we obtain the Yurke-Stoler state [112]

$$|\psi_{YS}\rangle = (|\alpha\rangle + i\,|-\alpha\rangle) / \sqrt{2}.$$

These three states, in fact all cat states, are the eigenstates of the square of the annihilation operator $\hat{a}^2$ with eigenvalue α^2. For brevity, let us focus now on the Yurke-Stoler state. The Husimi Q function of this state

$$Q_{|\psi_{YS}\rangle}(\beta) = \frac{1}{2\pi} e^{-|\alpha+\beta|^2} \left(e^{2\beta\alpha^*} - i\right)\left(e^{2\alpha\beta^*} + i\right)$$

is of course always positive and does not signal its extreme non-classical nature. As a matter of fact, the Husimi Q function of the Yurke-Stoler state cannot be distinguished (see Fig 1.10) from the mixture of coherent states with opposite amplitudes

$$\hat{\rho} = |\alpha\rangle\langle\alpha| + |-\alpha\rangle\langle-\alpha|,$$

because the fringes that arise due to the interference terms are few orders of magnitude lower than the Gaussians of the coherent states $|\alpha\rangle$ and $|-\alpha\rangle$.

However, the Wigner function, with its feature to take negative values, is a perfect tool to examine the non-classical character of the Yurke-Stoler state.

$$\begin{aligned} W_{|\psi_{YS}\rangle}(\beta) =& \frac{1}{\pi} e^{-|\alpha-\beta|^2} + \frac{1}{\pi} e^{-|\alpha+\beta|^2} \\ &+ \frac{1}{\pi} e^{-2|\alpha|^2} \left(i e^{-2(\beta+\alpha)(\beta^*-\alpha^*)} - i e^{-2(\beta-\alpha)(\beta^*+\alpha^*)}\right), \end{aligned}$$

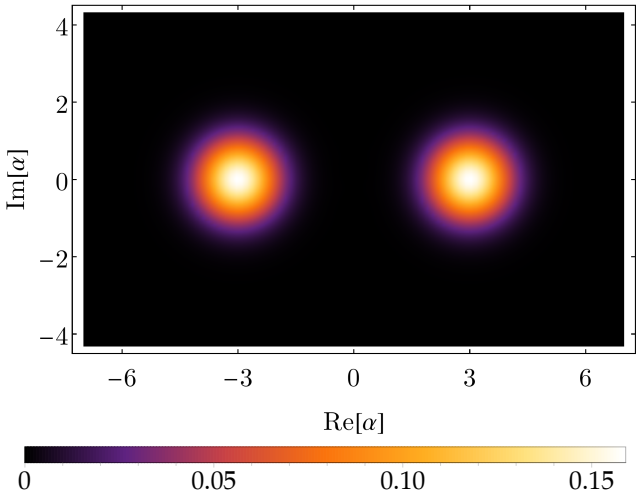

FIGURE 1.10: The Husimi Q function of Yurke-Stoler state $(|\beta\rangle + i\,|-\beta\rangle)/2$ for $\beta = 3$. Visually there is nothing that signals non-classicality of this state.

where the last line contains interference terms which causes the Wigner function to become highly oscillatory and take negative values. The difference between Formulas 1.5 and 1.5 is seemingly subtle, but the distributions (presented in Figure 1.10 and 1.11) are strikingly different.

The Yurke-Stoler state can be created from the unitary evolution of a coherent state in a nonlinear Kerr-like medium [112]. Another way of generating the cat states is a non-unitary method based on the so-called quantum non-demolition measurement [113] where the cat state is generated inside an optical cavity by measuring the state of the atom that was earlier interacting with the field in the cavity. This type of non-classical light was first observed by the group of Serge Haroche in superconducting microwave optical cavities [114]. Similar experiments were proposed in the regime of visible radiation [115–117] where it is possible to use the light, *e.g.* in optical interferometry.

1.6 Optical interferometer

Typically, optical interferometry relies on superimposing light (even from a single source) to perform extremely accurate measurements. The simplicity and versatility of optical interferometry give rise to its numerous applications in many fields starting from astronomy and reaching even particle physics [118]. One of the most renowned optical interferometers is the Mach-Zehnder interferometer in which the light injected into one of the input ports is being split, at the first beam-splitter, into two beams which propagate along different optical paths and thus acquire a relative phase shift θ. The beams meet again at a second beam-splitter where they interfere with each other. The information about the relative phase shift θ can be read out from the interference fringes.

The simplest interferometers, similarly to the Mach-Zehnder interferometer, are constructed from linear devices such as beam-splitters and phase-shifters. Let $\hat{a}$ and $\hat{b}$ denote the bosonic annihilation operators for two light beams, *e.g.*, light beams entering or exiting a beam-splitter. Any linear transformation of such a two-mode

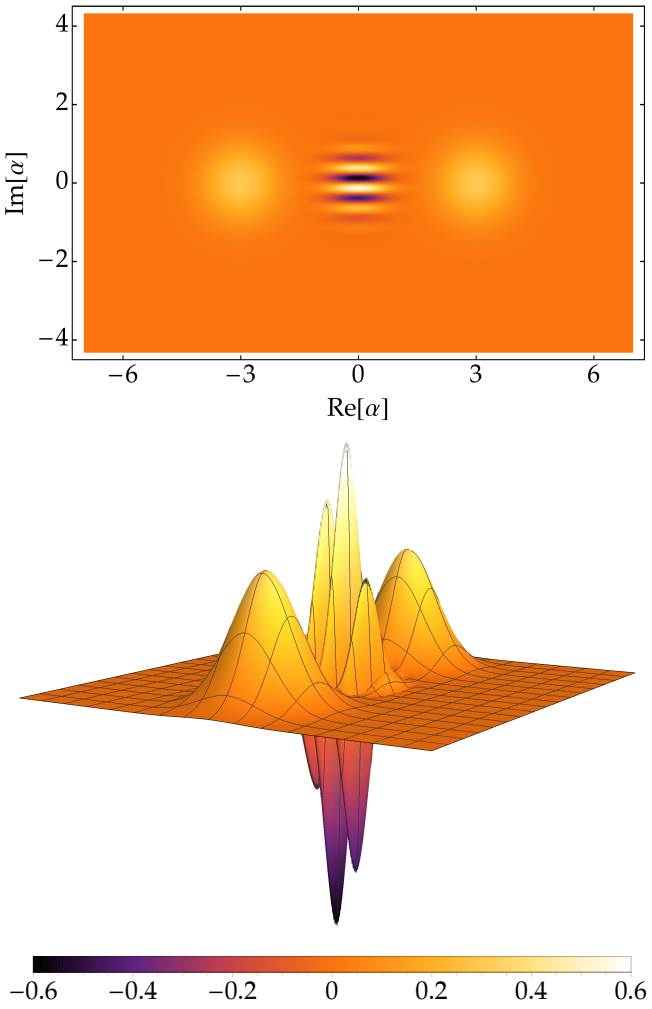

FIGURE 1.11: The Wigner function of the Yurke-Stoler state with $\beta = 3$. The top panel is the density function, and the bottom panel is a 3D zoom on the centre of the Wigner function. For comparison to the Husimi Q function, see Figure 1.10. The most peculiar feature of this Wigner function is the negativity and oscillations similar to interference fringes.

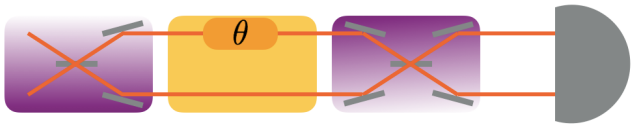

FIGURE 1.12: A sketch of the Mach-Zehnder interferometer. In the beginning, two sources of light are mixed on a beam-splitter. Next, the light goes along two different optical paths (phase imprint). Then, the modes are mixed again, and finally the light is being registered by the detector (grey semicircle)

system, or two-path system as in the case of the Mach-Zehnder interferometer, can

be expressed by

$$\begin{pmatrix} \hat{a}_{\text{out}} \\ \hat{b}_{\text{out}} \end{pmatrix} = \begin{pmatrix} e^{-i\phi_t} \cos\frac{\theta}{2} & -e^{-i\phi_r} \sin\frac{\theta}{2} \\ e^{i\phi_r} \sin\frac{\theta}{2} & e^{i\phi_t} \cos\frac{\theta}{2} \end{pmatrix} \begin{pmatrix} \hat{a}_{\text{in}} \\ \hat{b}_{\text{in}} \end{pmatrix},$$

where $0 \leq \theta \leq \pi$ and $0 \leq \phi_t$, $\phi_r \leq 2\pi$, and with $\hat{a}_{\text{out}}$, $\hat{b}_{\text{out}}$ and $\hat{a}_{\text{in}}$, $\hat{b}_{\text{in}}$ being the annihilation operators of the output and input modes, respectively. The transformation matrix

$$\begin{pmatrix} e^{-i\phi_t} \cos\frac{\theta}{2} & -e^{-i\phi_r} \sin\frac{\theta}{2} \\ e^{i\phi_r} \sin\frac{\theta}{2} & e^{i\phi_t} \cos\frac{\theta}{2} \end{pmatrix}$$

spans the whole SU(2) group, and therefore two-mode interferometry is sometimes referred to as SU(2) interferometry [119]. Since SU(2) group is homomorphous to the rotation group in three dimensions SO(3), the linear transformations can be visualised as rotations of the generalised Bloch sphere [120] with the help of the compact Schwinger formalism [121]. The transformation from Equation 1.6 can be viewed as a rotation of a vector

$$\hat{\mathbf{J}} \equiv \begin{pmatrix} \hat{J}_x \\ \hat{J}_y \\ \hat{J}_z \end{pmatrix} = \begin{pmatrix} \frac{1}{2}\left(\hat{a}^\dagger \hat{b} + \hat{b}^\dagger \hat{a}\right) \\ \frac{1}{2i}\left(\hat{a}^\dagger \hat{b} - \hat{b}^\dagger \hat{a}\right) \\ \frac{1}{2}\left(\hat{a}^\dagger \hat{a} - \hat{b}^\dagger \hat{b}\right) \end{pmatrix},$$

mathematically analogous to the angular momentum in three dimensions. These three operators satisfy the commutation relations for the Lie algebra of SU(2):

$$\left[\hat{J}_a, \hat{J}_b\right] = i\epsilon_{abc}\hat{J}_c,$$

where ϵ_{abc} is the antisymmetric Levi-Civita symbol (Einstein summation convention). The Casimir invariant for this group is

$$\hat{\mathbf{J}}^2 = \hat{J}_x^2 + \hat{J}_y^2 + \hat{J}_z^2 = \frac{\hat{N}}{2}\left(\frac{\hat{N}}{2} + 1\right),$$

where $\hat{N} = \hat{a}^\dagger \hat{a} + \hat{b}^\dagger \hat{b}$ is the particle number operator, in this case the number of photons in the two modes. To see how $\hat{\mathbf{J}}$ transforms under linear operations given by Equation 1.6, let us first consider a general, not necessarily balanced, beam-splitter. The transformation matrix for this kind of operation can be written as

$$\hat{U}_{\text{BS}} = \begin{pmatrix} \cos\frac{\theta}{2} & -i\sin\frac{\theta}{2} \\ -i\sin\frac{\theta}{2} & \cos\frac{\theta}{2} \end{pmatrix}.$$

This matrix transforms $\hat{\mathbf{J}}$ according to

$$\begin{pmatrix} \hat{J}_x \\ \hat{J}_y \\ \hat{J}_z \end{pmatrix}_{\text{out}} = \begin{pmatrix} 1 & 0 & 0 \\ 0 & \cos\theta & -\sin\theta \\ 0 & \sin\theta & \cos\theta \end{pmatrix} \begin{pmatrix} \hat{J}_x \\ \hat{J}_y \\ \hat{J}_z \end{pmatrix}_{\text{in}},$$

which is a rotation of the abstract angular momentum vectors around the x axis by an angle θ. This transformation can be expressed in a compact form as

$$\begin{pmatrix} \hat{J}_x \\ \hat{J}_y \\ \hat{J}_z \end{pmatrix}_{\text{out}} = e^{i\theta\hat{J}_x} \begin{pmatrix} \hat{J}_x \\ \hat{J}_y \\ \hat{J}_z \end{pmatrix}_{\text{in}} e^{-i\theta\hat{J}_x},$$

which can be verified by using the Baker-Campbell-Hausdorff formula from Equation 1.1. Alternatively, the same transformation can be evaluated in the Schrödinger picture where the operators $\hat{J}_x$, $\hat{J}_y$, and $\hat{J}_z$ remain unchanged. After interacting with the beam-splitter, the initial state of the light $|\text{in}\rangle$ becomes

$$|\text{out}\rangle = e^{-i\theta\hat{J}_x} |\text{in}\rangle .$$

Throughout this dissertation, depending on the convenience, we hop between the Heisenberg picture where $\hat{\mathbf{J}}$ is rotated and the Schrödinger picture where $\hat{\mathbf{J}}$ remains fixed.

Another linear element which we focus on is a phase-shifter. The unitary matrix associated with this element is

$$\hat{U}_{\text{PS}} = \begin{pmatrix} e^{i\theta_a} & 0 \\ 0 & e^{i\theta_b} \end{pmatrix},$$

where θ_a and θ_b are the phase shifts that light beams $\hat{a}$ and $\hat{b}$ experience, respectively. A more convenient way of writing this kind of transformation is to factor out $e^{i\theta_a}$ and express the transformation in terms of the relative phase shift $\theta = \theta_b - \theta_a$

$$\hat{U}_{\text{PS}} = \begin{pmatrix} 1 & 0 \\ 0 & e^{i\theta} \end{pmatrix}.$$

Under this type of transformation, $\hat{\mathbf{J}}$ transforms according to

$$\begin{pmatrix} \hat{J}_x \\ \hat{J}_y \\ \hat{J}_z \end{pmatrix}_{\text{out}} = \begin{pmatrix} \cos\theta & -\sin\theta & 0 \\ \sin\theta & \cos\theta & 0 \\ 0 & 0 & 1 \end{pmatrix} \begin{pmatrix} \hat{J}_x \\ \hat{J}_y \\ \hat{J}_z \end{pmatrix}_{\text{in}},$$

which represents a rotation around the z axis by the angle θ. This transformation can be also expressed as

$$\begin{pmatrix} \hat{J}_x \\ \hat{J}_y \\ \hat{J}_z \end{pmatrix}_{\text{out}} = e^{i\theta\hat{J}_z} \begin{pmatrix} \hat{J}_x \\ \hat{J}_y \\ \hat{J}_z \end{pmatrix}_{\text{in}} e^{-i\theta\hat{J}_z},$$

or alternatively in the Schrödinger picture as a

$$|\text{out}\rangle = e^{-i\theta\hat{J}_z} |\text{in}\rangle .$$

It is worth noting that operators $\hat{a}^\dagger\hat{a}$ and $\hat{b}^\dagger\hat{b}$, characterising the number of photons counted by a photodetector, can be expressed in terms of $\hat{N}$ and $\hat{J}_z$; thus interferometry can be thought of as a process of measuring angles of rotations of $\hat{\mathbf{J}}$.

So far, we have managed to show that a beam-splitter can be associated with $\hat{J}_x$ operator and a phase-shifter can be associated with $\hat{J}_z$. We could check now what kind of transformation corresponds to $\hat{J}_y$ operator, but first of all, let us focus on the

Mach-Zehnder interferometer which is constructed from just two balanced beam-splitters and a phase-shifter. For a balanced beam-splitter, θ must take on the value of $\pi/2$ or $-\pi/2$. If there was no phase shifter between the beam-splitters, then the initial state $|\text{in}\rangle$ should remain unchanged. Therefore we choose the first beam-splitter to have $\theta = \pi/2$ and the second one $\theta = -\pi/2$. The state after leaving the interferometer is thus

$$|\text{out}\rangle = e^{i\frac{\pi}{2}\hat{J}_x} e^{-i\theta\hat{J}_z} e^{-i\frac{\pi}{2}\hat{J}_x} |\text{in}\rangle ,$$

which is a rotation of the $e^{-i\theta\hat{J}_z}$ around the x axis by the angle $\pi/2$ which is equivalent to writing

$$|\text{out}\rangle = e^{i\frac{\pi}{2}\hat{J}_x} e^{-i\theta\hat{J}_z} e^{-i\frac{\pi}{2}\hat{J}_x} |\text{in}\rangle = e^{-i\theta\hat{J}_y} |\text{in}\rangle .$$

We arrive at the result that the Mach-Zehnder transformation corresponds to $\hat{J}_y$ operator.

Now, the question is how to infer the value of θ. Since we can measure the number of photons at each of the output ports of the interferometer, we can, in principle, measure the $\hat{J}_z$ operator. Its average value calculated on the output state is

$$\langle \hat{J}_z \rangle = \langle \text{out}|\hat{J}_z|\text{out}\rangle = \langle \text{in}|e^{i\theta\hat{J}_y} \hat{J}_z e^{-i\theta\hat{J}_y}|\text{in}\rangle ,$$

which by using the Baker-Campbell-Hausdorff formula can be simplified to

$$\langle \hat{J}_z \rangle = \langle \text{out}|\hat{J}_z|\text{out}\rangle = \cos\theta \langle \text{in}|\hat{J}_z|\text{in}\rangle - \sin\theta \langle \text{in}|\hat{J}_x|\text{in}\rangle .$$

Therefore, we have an indirect access to θ simply by measuring the average number of photons at each of the output ports and thus measuring the average value of $\hat{J}_z$. In such a case the uncertainty of θ is given by the error propagation formula

$$\Delta^2\theta = \frac{\Delta^2 \hat{J}_z}{\left(\partial_\theta \langle \hat{J}_z \rangle\right)^2},$$

where all the quantities are calculated on the output state $|\text{out}\rangle$. We can now also calculate the average value of $\hat{J}_z^2$

$$\begin{aligned}\langle \hat{J}_z^2 \rangle &= \langle \text{out}|\hat{J}_z^2|\text{out}\rangle \\ &= \cos^2\theta \langle \text{in}|\hat{J}_z^2|\text{in}\rangle - \cos\theta\sin\theta \langle \text{in}|\{\hat{J}_x, \hat{J}_z\}|\text{in}\rangle + \sin^2\theta \langle \text{in}|\hat{J}_x^2|\text{in}\rangle ,\end{aligned}$$

where $\{\hat{J}_x, \hat{J}_z\} = \hat{J}_x\hat{J}_z + \hat{J}_z\hat{J}_x$ is the anti-commutator, and calculate the uncertainty of θ for a Fock state $|n\rangle$

$$\Delta^2\theta = \frac{\frac{n}{4}\sin^2\theta}{\sin^2\theta\frac{n^2}{4}} = \frac{1}{n},$$

which is the shot-noise limit from Equation 0.1. Interestingly, one of the simplest types of measurement can already give the shot-noise scaling of the uncertainty. We come back to this result again in Chapter 3, but now we want to focus on one more thing. As we wrote in the introduction, the classical limit of precision can be only surpassed by using non-classical states. Here, we used the Fock state which is non-classical, however, the shot-noise limit has not been surpassed. The explanation for this may be two-fold. First, we do not know yet whether this simple type of

measurement allows for breaking the classical limit of precision, and second, the non-classicality of the single Fock state may be not sufficient or not of the type that allows for sub-shot-noise interferometry. This issue is also addressed in Chapter 3, but already now, we can identify a class of states that for this type of measurement can give scaling of uncertainty better than $1/n$. If we found a state which is somehow squeezed on the generalised Bloch sphere in a way that $\langle \hat{J}_z \rangle$ is of the order of n, but $\Delta^2 \hat{J}_z$ is constant, it would be possible to achieve $\Delta^2\theta < 1/n$. As it is pointed out in Chapter 3, the sensitivity of an interferometer can be extremely improved if photons are allowed to enter both input ports provided the photons are prepared in the appropriate quantum state.

The states that allow for sub-shot-noise interferometry must be entangled, which becomes evident in Chapter 3. The single mode states of light cannot be entangled because there is only a single mode and therefore there is nothing to be entangled with. However, non-classical single mode states are promising candidates to create entangled states of two modes as in the case of the interferometer's input state. Then the state is said to be entangled in terms of interferometer's modes.

An interesting example is an input state composed from a coherent state and a squeezed vacuum state [27]

$$|\psi\rangle = |\alpha\rangle \otimes |0\rangle \,.$$

Now, we can easily calculate the uncertainty of θ by evaluating expression from Equation 1.6

$$\Delta^2\theta = \frac{|\alpha|^2 e^{-2r} + \sinh^2 r}{(|\alpha|^2 - \sinh^2 r^2)} + \frac{|\alpha|^2 + 2\sinh^2 r \cosh^2 r}{(|\alpha|^2 - \sinh^2 r^2)\tan^2\theta}.$$

According to the above Equation, phase sensitivity can only overcome the shot-noise limit when the true value of the phase is approximately equal to the optimal value $\theta = \pi/2$ where $\langle \hat{J}_z \rangle = 0$. Asymptotically, when $|\alpha|^2 \gg \sinh^2 r$, the above Equation predicts at the optimal point the following sub shot-noise sensitivity

$$\Delta\theta = \frac{e^{-r}}{\sqrt{\bar{n}}},$$

where $\bar{n} = |\alpha|^2 + \sinh^2 r \approx |\alpha|^2$ is the average photon number at input ports of the Mach-Zehnder interferometer. However, if we choose to measure the number of particles on each of the output ports, so not only the difference, then it can be shown that the phase sensitivity of the Mach-Zehnder interferometer fed with the state from Equation 1.6 is

$$\Delta\theta = \frac{1}{\sqrt{|\alpha|^2 e^{2r} + \sinh^2 r}},$$

which is independent of the value of an unknown parameter θ and reaches the Heisenberg scaling when $|\alpha|^2 \simeq \sinh^2 r \simeq \bar{n}/2 \gg 1$

$$\Delta\theta = \frac{1}{\bar{n}}.$$

The estimation from the average population imbalance is not the optimal type of measurement. The phase estimate based only on the analysis of the average relative

number of particles does not benefit from all the available information. In particular, it does not consider information contained in the fluctuations of the number of particles and in higher moments. Further details on the optimal choice of estimation protocol are given in Chapter 3.

Chapter 2

Ultracold Quantum Gases in Optical Lattices

Due to the recent technological advancement in trapping and controlling ultracold quantum gases [122], these systems are currently one of the most interesting and versatile physical systems with a variety of applications, *e.g.* in probing fundamental condensed-matter physics [123–134], atomic and molecular physics [135], quantum optics, and quantum information processing. The possibility of creating artificial crystals by storing ultracold quantum gases in periodic potentials of light enabled experimentalist to build systems acting like quantum simulators which can be used to imitate dynamics of some other complex quantum system [136].

From the perspective of quantum metrology, one of the most interesting physical systems that can be stored in an optical lattice is a Bose-Einstein condensate, a state of matter where bosons, which constitute the condensate, occupy the lowest accessible quantum state, and where quantum effects become apparent on a macroscopic scale. Its first experimental realisation [137–139], after almost seventy years from its theoretical prediction by Bose and Einstein [140, 141], started a new era in the field of atomic physics. Since that time, many experiments have been carried out with Bose-Einstein condensates including the observation of interference of two independent condensates [142, 143], long-range phase coherence [125], four-wave mixing for the atomic field [144], superradiance [145], amplification [146, 147], atom laser [148, 149], dark and bright solitons [150–153], quantised vortices and vortex lattice [154–156], and spin squeezing and spin-nematic squeezing [126, 157]. Furthermore, various potential applications have been identified, in particular, quantum interferometry where by storing a Bose-Einstein condensate in a two-site optical lattice, one can create a two-mode interferometer analogous to the optical interferometer that was described in the previous Chapter.

Contents

2.1 Bose-Hubbard Hamiltonian

Ultracold bosonic atoms are usually stored in the dipole traps, where the oscillating electric field from a laser induces an oscillating atomic dipole moment simultaneously interacting with it, thus creating the trapping potential for the atoms

$$V_{\mathrm{dip}}(\mathbf{r}) = -\mathbf{d} \cdot \mathbf{E}(\mathbf{r}) \propto \alpha(\omega_{\mathrm{L}})|\mathbf{E}(\mathbf{r})|^2,$$

where $\alpha(\omega_L)$ is the atomic polarisability and $|E(\mathbf{r})|^2$ is the laser light intensity with $|E(\mathbf{r})|$ being its electric field amplitude at position $\mathbf{r}$, and $\mathbf{d}$ is the atomic dipole moment. To prevent from atomic excitations and spontaneous emission, the laser is typically tuned far away from the atomic transition frequency.

The 1D optical lattice is formed by overlapping counter-propagating laser beams, which interfere and create an optical standing wave with periodicity $\lambda_{\mathrm{L}}/2$. 2D and 3D lattices are also possible to create by interfering more beams (see Figure 2.1). By changing the intensity of laser beams, their frequency, and the angle at which they cross, it is possible to change the geometry and depth of optical lattices, even dynamically during an ongoing experiment.

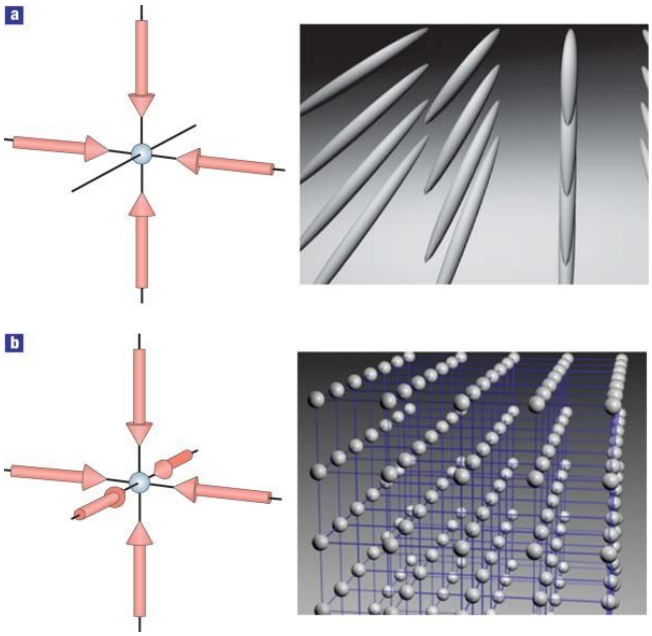

FIGURE 2.1: **a**, in a 2D optical lattice, the atoms are confined to an array of potential tubes. **b**, In the 3D case, the optical lattice can be approximated by a 3D simple cubic array of harmonic potentials at each lattice site. Figure reprinted from Reference [122].

A standing wave creates a periodic potential which has the following form

$$V_{\mathrm{lat}} = V_0 \sin^2(k_{\mathrm{L}} x),$$

where $k_{\mathrm{L}} = 2\pi/\lambda_{\mathrm{L}}$ is the laser light wave vector, and V_0 is the depth of the potential. The motion of particles in such periodic potentials can be described in terms of Bloch waves, but if one considers only the lowest Bloch band, the dynamics of interacting

bosons is governed by the Bose-Hubbard Hamiltonian [123]

$$\hat{H} = -J \sum_{\langle i\, j \rangle} \hat{a}_i^\dagger \hat{a}_j + \frac{U}{2} \sum_i \hat{n}_i \left(\hat{n}_i - 1 \right).$$

Let us now focus on each term of this Hamiltonian in order to get insight in what they amount to. The first term (kinetic energy) describes the tunnelling between neighbouring lattice sites $\langle i, j \rangle$, where $\hat{a}_i^\dagger$ and $\hat{a}_i$ are the creation and annihilation operators of a particle on lattice site i. The second term in the Hamiltonian describes the onsite interactions between the bosons, where $\hat{n}_i = \hat{a}_i^\dagger \hat{a}_i$ is the operator that describes the number of particles on site i, with U being the interaction strength. Notice that this interaction is only possible when atoms are present on the same lattice site. Despite its simplicity, this Hamiltonian captures the essence of competing linear and non-linear interactions, leading to interesting, non-trivial dynamics.

A system that is described by the Bose-Hubbard Hamiltonian exhibits two important ground states, and according to this, we can distinguish two prominent regimes depending on the parameters. The superfluid phase regime is the limit where the kinetic energy is dominating ($U/J \ll 1$), and atoms can easily move between the lattice sites. In this regime, the system energy is minimised when atoms delocalise over the entire lattice, and the ground state is a superposition of atoms sitting on each lattice site. In other words, the system forms a Bose-Einstein condensed state of matter with atoms delocalised over the entire lattice:

$$|\mathrm{BEC}\rangle \propto \left(\sum_{i=1}^{M} \hat{a}_i^\dagger \right)^N |0\rangle ,$$

where N is the number of atoms, M is the number of lattice sites, and $|0\rangle$ is the atomic vacuum state. On the other hand, if the tunnelling is suppressed ($U/J \gg 1$), atoms will occupy individual lattice sites, and the system becomes a strongly correlated state known as the Mott insulator:

$$|\mathrm{MOTT}\rangle \propto \prod_{i=1}^{M} \left(\hat{a}_i^\dagger \right)^n |0\rangle ,$$

where n is the number of atoms per each lattice site.

The transition of this quantum many-body state between Bose-Einstein condensate phase and Mott-insulator phase [125] remains an active and intriguing field of research, possibly with connections to cosmological phase transitions [158].

A Bose-Einstein condensate can also be confined to just two wells of a periodic potential, creating a double-well or two-mode Bose-Einstein condensate [159]. This kind of system can be effectively described by a single Josephson junction [160] for ultracold atomic gases.

2.2 Two-site Bose-Hubbard model

The two-site Bose-Hubbard model, also known as canonical Josephson Hamiltonian [161], reads as follows

$$\hat{H} = -2J\hat{J}_x + \frac{U}{2} \left(2\hat{J}_z^2 + \frac{\hat{N}^2}{2} - \hat{N} \right),$$

where $\hat{J}_x$ and $\hat{J}_y$ are operators from Equation 1.6, and $\hat{N}$ is the total atom number operator. Since the Hamiltonian conserves the total number of bosons, the operators $\hat{N}$ and $\hat{N}^2$ result in a global phase factor only and can be safely neglected. Thus, we can focus now simply on the simplified version of this Hamiltonian which reads

$$\hat{H} = -2J\hat{J}_x + U\hat{J}_z^2.$$

Before going to the fully quantum picture, let us first look at the two-site Bose-Hubbard Hamiltonian from the perspective of the mean-field theory. Under this semi-classical approximation, the state of the system is described as a tensor product of coherent states each identical to the canonical coherent state

$$|\psi\rangle = |\alpha_1\rangle \otimes |\alpha_2\rangle ,$$

such that $\hat{a}_i |\alpha_i\rangle = \alpha_i |\alpha_i\rangle$, where $\alpha_i = \sqrt{N_i(t)}e^{i\theta_i(t)}$ with $N_i(t)$ being the average number of atoms in the ith well at time t and $\theta_i(t)$ is the corresponding phase of the atoms. Note that this approximation is valid only if the number of atoms is large enough so that

$$\hat{a}_i |N_i\rangle = \sqrt{N_i} |N_i - 1\rangle \approx \sqrt{N_i} |N_i\rangle .$$

Now, we can define the variables

$$z \equiv \frac{N_1 - N_2}{N}$$
$$\theta \equiv N\frac{\theta_1 - \theta_2}{2},$$

where z represents the fractional occupation difference, or the population imbalance, and θ represents the phase difference, and we may consider a classical Hamiltonian

$$H = \langle\psi|\hat{H}|\psi\rangle = -JN\sqrt{1-z^2}\cos\left(\frac{2\theta}{N}\right) + \frac{UN^2}{4}z^2,$$

equivalent to the classical nonrigid pendulum Hamiltonian [162], where (z, θ) are canonically conjugate coordinates. The classical dynamics are then given by Hamilton's equation of motion

$$\dot{\theta} = \frac{\partial H}{\partial z} = JN\frac{z}{\sqrt{1-z^2}}\cos\left(\frac{2\theta}{N}\right) + \frac{UN^2}{2}z$$
$$\dot{z} = -\frac{\partial H}{\partial \theta} = -2J\sqrt{1-z^2}\sin\left(\frac{2\theta}{N}\right).$$

We will need these semi-classical result later to compare with the quantum one. The most convenient way to calculate the dynamics in the fully quantum model is to switch to the Heisenberg picture and calculate the evolution of operators according to the Heisenberg equation of motion

$$\frac{\mathrm{d}}{\mathrm{d}t}\hat{O}(t) = \frac{i}{\hbar}\left[\hat{H}, \hat{O}(t)\right].$$

It is straightforward to show that

$$\frac{\mathrm{d}}{\mathrm{d}t}\hat{a}_1 = -J\hat{a}_2 + \frac{U}{2}\hat{a}_1^\dagger\hat{a}_1\hat{a}_1 - 2U\hat{a}_1\hat{a}_2^\dagger\hat{a}_2,$$
$$\frac{\mathrm{d}}{\mathrm{d}t}\hat{a}_2 = -J\hat{a}_1 + \frac{U}{2}\hat{a}_2^\dagger\hat{a}_2\hat{a}_2 - 2U\hat{a}_2\hat{a}_1^\dagger\hat{a}_1.$$

Now, we are in the position to compare the mean-field and the fully quantum model. First, let us have a look at the case without the on-site interaction term, *i.e*, $U = 0$, so the atoms can only tunnel between the two wells. It is straightforward to show that the evolution of operators from Equation 1.6 reads

$$\hat{J}_x \to \frac{N}{2}\sqrt{1-z^2}\cos\left(\frac{2\theta}{N}\right)$$
$$\hat{J}_y \to \frac{N}{2}\sqrt{1-z^2}\sin\left(\frac{2\theta}{N}\right)$$
$$\hat{J}_z \to \frac{N}{2}z.$$

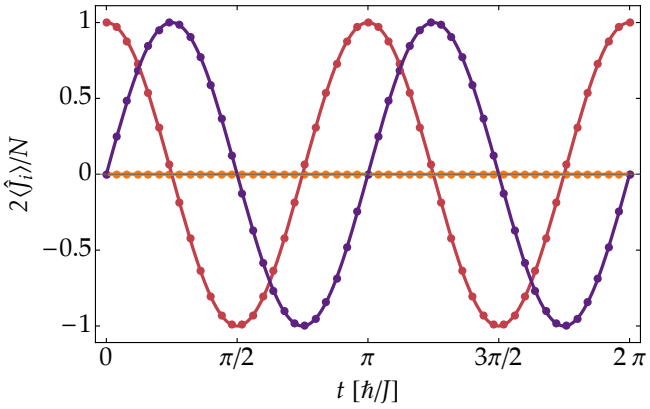

FIGURE 2.2: Tunnelling in a Bose-Einstein condensate in a double-well potential. Initially, the atoms are all in one well $\hat{J}_z|\psi\rangle = \frac{N}{2}|\psi\rangle$. The y (violet) and z (burgundy) components oscillate, while the x (orange) component stays constant. This is because the state is rotated around the x axis. Solid lines and dots represent quantum and mean-field approach, respectively. There are no differences between those two approaches. Simulation performed for $N = 10$ atoms.

In Figure 2.2, we see quantum and mean-field trajectories of the angular momentum operators. Since the atoms do not interact with each other, the state of the atoms gets only rotated around the x axis. Now let us have a look at a case where the on-site interaction energy is nonzero, but still is dominated by the tunnelling term.

In Figure 2.3, we see that there is a small discrepancy between quantum and mean-field approaches when atoms are interacting. The difference arises because the on-site interaction creates a non-classical state of atoms which is impossible in the mean-field where atoms are treated in a classical fashion. The difference becomes even more apparent when we increase the strength of the on-site interaction (see Figure 2.4).

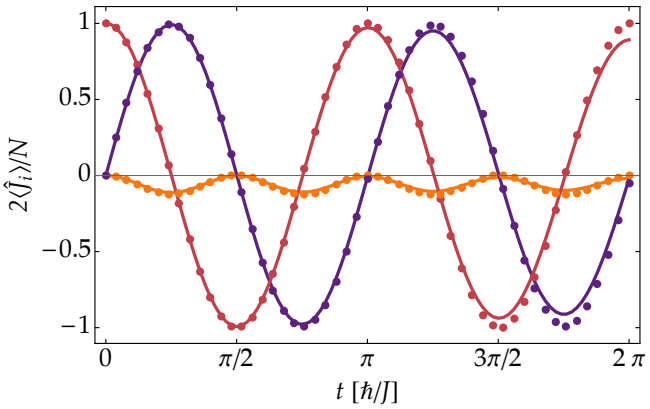

FIGURE 2.3: Tunnelling in a Bose-Einstein condensate in a double-well potential accompanied by on-site interaction $U = 0.05J$. Initially the atoms are all in one well $\hat{J}_z\,|\psi\rangle = \frac{N}{2}\,|\psi\rangle$. The y (violet), z (burgundy), and x (orange) components are oscillating. Solid lines and dots represent quantum and mean-field approach, respectively. The mean-field approach (dotted) does not completely follow the quantum trajectory (solid). Simulation performed for $N = 10$ atoms.

Finally, we can change the type of the interactions between the atoms from repulsive $U > 0$ to attractive $U < 0$, and see how the mean-field approach copes with this change. In Figure 2.5, we see that the two approaches are similar, but oscillations in the mean-field are faster. The discrepancies between mean-field and quantum approaches are not extreme, and one can learn a lot from the semi-classical picture, especially when it comes to the classification of solutions, delocalisation, and self-trapping [163]. However, one essential part of quantum dynamics is elusive to the mean-field approach. The semi-classical approach can never generate a non-classical state of atoms inside the two-well potential. This special non-classicality that arises from the interaction between atoms in the quantum description is called entanglement [108, 164], and as we shall see in the next Chapter this special type of non-classicality plays the key role in quantum metrology. Before that, we first need to see the difference between a classical state of atoms, *i.e.*, a coherent spin state, and any other pure two-mode atomic state.

2.3 Spin coherent states

Coherent spin states [165] are analogous to the canonical coherent states introduced in the previous Chapter. They can be used to describe spin $\frac{1}{2}$ ensembles and in general single $\frac{N}{2}$ spins. In the seminal work by Radcliffe in 1971 [165], he wrote

> It is still an open question as to whether the spin states defined here will prove useful. They may, at the very least, give some physical insight into problems involving spins and their correlations.

Nowadays, coherent spin states are extremely useful wherever one has to do something with a collection of two-level atoms, or two mode systems in general. For instance, one of their numerous applications is to study quantum chaos [166].

Let us consider a collection of N spin $\frac{1}{2}$, for instance, two-level atoms, or equivalently an abstract single $\frac{N}{2}$ spin [167]. We define the ground state as an eigenvector

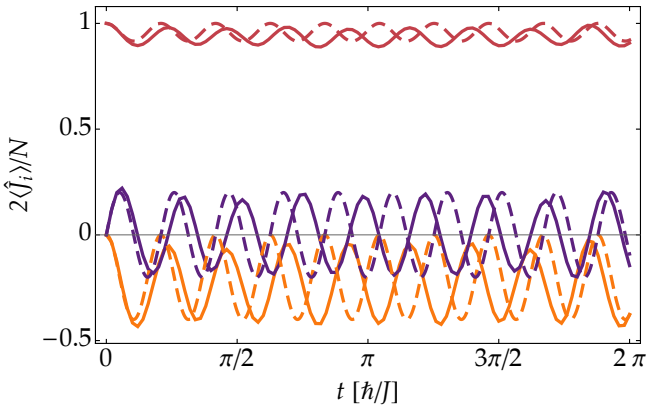

FIGURE 2.4: Tunnelling in a Bose-Einstein condensate in a double-well potential accompanied by on-site interaction $U = J$. Initially, the atoms are all in one well $\hat{J}_z |\psi\rangle = \frac{N}{2} |\psi\rangle$. The y (violet), z (burgundy), and x (orange) components are oscillating. Solid lines and dashed lines represent quantum and mean-field approach, respectively. Now, the mean-field approach (dashed) does not follow the quantum trajectory (solid). Simulation performed for $N = 10$ atoms.

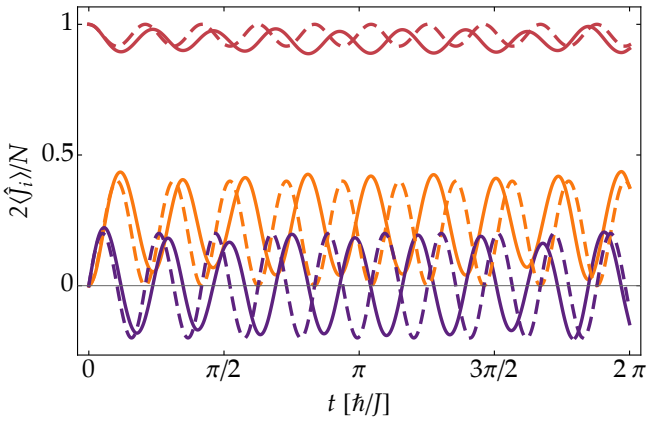

FIGURE 2.5: Tunnelling in a Bose-Einstein condensate in a double-well potential accompanied by on-site interaction $U = -J$. In this case, the atoms attract each other. Initially, the atoms are all in one well $\hat{J}_z |\psi\rangle = \frac{N}{2} |\psi\rangle$. The y (violet), z (burgundy), and x (orange) components are oscillating. Solid lines and dashed lines represent quantum and mean-field approach, respectively. Now, the mean-field approach (dashed) does not follow the quantum trajectory (solid). Simulation performed for $N = 10$ atoms.

of the the $\hat{J}_z$ operator with eigenvalue $N/2$. According to this, we can introduce the Dickie basis $\{|j, j'\rangle\}$ with $j = \frac{N}{2}$ and j' ranging from $-\frac{N}{2}$ to $\frac{N}{2}$, where

$$\hat{J}_z |j, j'\rangle = j' |j, j'\rangle .$$

Therefore the ground state in the Dickie basis is simply $|j, j\rangle$. A coherent spin state is defined then as

$$|z\rangle = \frac{1}{(1+|z|^2)^j} \exp\left(z\hat{J}_-\right)|j, j\rangle ,$$

where $z = \tan\frac{\theta}{2}e^{i\phi}$ with θ ranging from 0 to π and with ϕ ranging from 0 to π, and $\hat{J}_- = \hat{J}_x - i\hat{J}_y$ is the ladder operator defined as

$$\hat{J}_-|j, j'\rangle = \sqrt{j(j+1) - j'(j'-1)}\,|j, j'-1\rangle .$$

The coherent spin states are normalised and their overlap is

$$\langle z|\zeta\rangle = \frac{(1+z^*\zeta)^{2j}}{(1+|z|^2)^j\,(1+|\zeta|^2)^j},$$

and the completeness relation reads

$$\frac{2j+1}{\pi}\int \frac{\mathrm{d}^2 z}{(1+|z|^2)^2}\,|z\rangle\langle z| = \hat{I}.$$

In the limit of $j \gg 1$, we can perform the so-called high-spin limit of the Holstein-Primakoff transformation [168] and write

$$\hat{J}_- \to \sqrt{2j}\hat{a}^\dagger$$
$$z \to \frac{\alpha}{\sqrt{2j}}.$$

The normalised states $|\alpha, j\rangle$ are then

$$|\alpha, j\rangle = \left(1 + \frac{|\alpha|^2}{2j}\right)^{-j} \exp\left(\alpha\hat{a}^\dagger\right)|0\rangle ,$$

where in the limit

$$\lim_{j\to\infty}\left(1 + \frac{|\alpha|^2}{2j}\right)^{j} = \exp\left(\frac{1}{2}|\alpha|^2\right),$$

and finally

$$\lim_{j\to\infty}|\alpha, j\rangle = \exp\left(\frac{1}{2}|\alpha|^2\right)\exp\left(\alpha\hat{a}^\dagger\right)|0\rangle ,$$

which is exactly the canonical coherent state from Equation 1.1.

An alternative parametrisation can be copied from the description of a qubit. A state of a qubit can be parametrised by two angles θ and ϕ being the colatitude with respect to the z axis and the longitude with respect to the x axis, respectively (see Figure 2.6). Therefore a general qubit can be represented by

$$|\psi\rangle = \cos\frac{\theta}{2}e^{-i\frac{\phi}{2}}|0\rangle + \sin\frac{\theta}{2}e^{i\frac{\phi}{2}}|1\rangle ,$$

where $0 \leq \theta \leq \pi$ and $0 \leq \phi < 2\pi$. Except in the case where $|\psi\rangle$ is one of the states $|0\rangle$ or $|1\rangle$, the representation is unique.

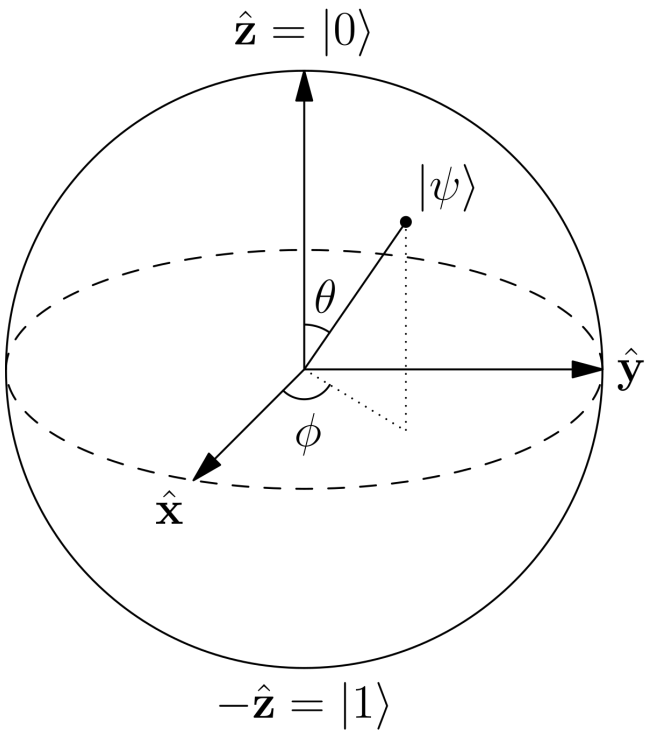

FIGURE 2.6: Bloch sphere representing a state of a qubit. Here $|\psi\rangle = \cos\frac{\theta}{2}|0\rangle + \sin\frac{\theta}{2}e^{i\phi}|1\rangle$, but since the global phase is of no relevance, this description is equivalent to the one from Equation 2.3. Figure taken from Reference [169].

A coherent spin state is a state that can be written as a tensor product of N qubits

$$|\theta,\phi\rangle = \left(\cos\frac{\theta}{2}e^{-i\frac{\phi}{2}}|0\rangle + \sin\frac{\theta}{2}e^{i\frac{\phi}{2}}|1\rangle\right)^{\otimes N},$$

which by using the creation operators $\hat{a}^\dagger$ and $\hat{b}^\dagger$ can be rewritten in the following way

$$\begin{aligned}|\theta,\phi\rangle &= \left(\cos\frac{\theta}{2}e^{-i\frac{\phi}{2}}\hat{a}^\dagger + \sin\frac{\theta}{2}e^{i\frac{\phi}{2}}\hat{b}^\dagger\right)^N|0\rangle \\ &= \sum_{n=0}^{N}\sqrt{\binom{N}{n}}\left(e^{\frac{i\phi}{2.}}\cos\frac{\theta}{2}a^\dagger\right)^{N-n}\left(e^{\frac{-i\phi}{2}}\sin\frac{\theta}{2}b^\dagger\right)^n|0\rangle,\end{aligned}$$

and finally can be expressed as

$$|\theta,\phi\rangle = \left(\cos\frac{\theta}{2}\right)^{2j}\exp\left(\tan\frac{\theta}{2}e^{i\phi}\hat{J}_-\right)|j,j\rangle,$$

where $j = N/2$, which is exactly the coherent spin state from Equation 2.3 with $z = \tan\frac{\theta}{2}e^{i\phi}$. The completeness relation using these states is

$$\frac{2j+1}{4\pi}\int \mathrm{d}\phi\mathrm{d}\theta \sin\theta \,|\theta,\psi\rangle\,\langle\theta,\psi| = \hat{I},$$

and the overlap between two states $|\theta,\phi\rangle$ and $|\theta',\phi'\rangle$ is

$$\langle\theta',\psi'|\theta,\psi\rangle = \left(\cos\frac{\theta'}{2}\cos\frac{\theta}{2} + \sin\frac{\theta'}{2}\sin\frac{\theta}{2}e^{i(\phi-\phi')}\right)^{2j},$$

and so

$$|\langle\theta',\psi'|\theta,\psi\rangle| = \left(\frac{1+\mathbf{n}\cdot\mathbf{n}'}{2}\right)^{j},$$

where $\mathbf{n}$ and $\mathbf{n}'$ are two unit vectors with directions specified by (θ,ϕ) and (θ',ϕ'), respectively. There exists a simple geometrical construction that relates z and the variables (θ,ϕ). If we write $z = \rho e^{i\phi'}$ and draw the z plane tangental to a sphere of unit diameter where the z axis meets the sphere, then the point z is the projection onto the z plane of the point (θ,ϕ) on the sphere from the opposite pole. Clearly $\phi' = \phi$, $\rho = \tan\frac{\theta}{2}$ [170].

Coherent spin states are advantageous when it comes to the visualisation of quantum states and to some extent when it comes to quantifying their properties, for example, their entanglement. In analogy to the Husimi Q function, it is possible to create a similar function for two-mode systems. Since the coherent spin states are states with finite Hilbert space, the Husimi Q function is confined to a sphere, and because of that, it is called the SU(2) Husimi Q function. Obviously, in the limit of a large number of spins, it can be approximated by a plane.

2.4 SU(2) Husimi Q function

Any state of a two-mode system, pure or mixed, can be visualised through SU(2) Husimi Q function according to

$$Q_{\hat{\rho}}(\theta,\phi) = \frac{2j+1}{4\pi}\langle\theta,\phi|\hat{\rho}|\theta,\phi\rangle,$$

where

$$\int \mathrm{d}\Omega\, Q_{\hat{\rho}} = 1,$$

with $\mathrm{d}\Omega = \mathrm{d}\phi\,\mathrm{d}\theta\sin\theta$ being the solid angle. One of the simplest SU(2) Husimi Q function is the one for a coherent spin state. For a coherent spin state $|\pi/2,0\rangle$, by using Equation 2.3, it is straightforward to show that

$$Q_{|\pi/2,0\rangle}(\theta,\phi) = \frac{2j+1}{4\pi}\left(\frac{1}{2}(\sin\theta\cos\phi+1)\right)^{2j}.$$

In Figure 2.7, we can see two alternative projections of the Husimi Q function. Similarly to the Husimi Q function for coherent states, it is relatively easy to calculate, but it does not reveal too much details about the quantum state. However, this is not the case of the SU(2) Wigner function.

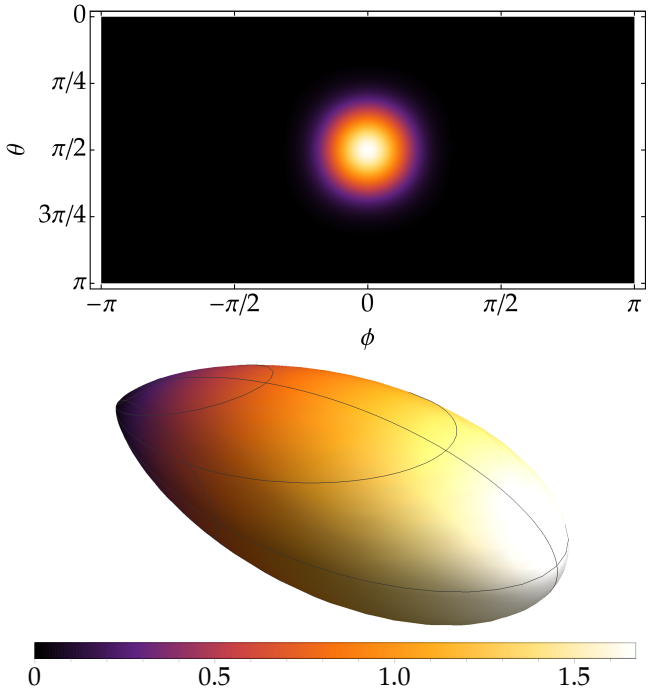

FIGURE 2.7: Two alternative visualisations of the SU(2) Husimi Q function for a coherent spin state $|\pi/2, 0\rangle$. In the upper panel, we see the Mercator projection, while in the lower panel, we see the 3D visualisation of the SU(2) Husimi Q function. Here $j = 10$. Notice that the values of this function strongly depend on j.

2.5 SU(2) Wigner function

To arrive at the SU(2) Wigner function [171], we first need to introduce the general theory of multipole operators [172]. An arbitrary atomic or angular-momentum operator $\hat{G}$ can be expanded as

$$\hat{G} = \sum_{k=0}^{2j} \sum_{q=-k}^{k} G_{kq} \hat{T}_{kq},$$

where the $\hat{T}_{kq}$ is the multipole operator defined by

$$\hat{T}_{kq} = \sum_{m=-j}^{j} \sum_{m'=-j}^{j} (-1)^{j-m} \sqrt{2k+1} \begin{pmatrix} j & k & j \\ -m & q & m' \end{pmatrix} |j, m\rangle \langle j, m'| ,$$

where

$$\begin{pmatrix} j & k & j \\ -m & q & m' \end{pmatrix}$$

is the Wigner $3j$ symbol [172]. The expansion coefficients G_{kq} are obtained from the orthogonality of the multipole operators

$$G_{kq} = \mathrm{Tr}\left[\hat{G}\hat{T}_{kq}^{\dagger}\right].$$

The Wigner function associated with the atomic operator $\hat{G}$ is then defined by

$$W(\theta,\phi) = \sum_{k=0}^{2j} \sum_{q=-k}^{k} Y_{kq}(\theta,\phi) G_{kq},$$

where Y_{kq} are the spherical harmonics. Unfortunately there is no simple way of deriving a compact expression for the SU(2) Wigner function of any state. In Figure 2.8, we can see the SU(2) Wigner function for a coherent spin state $|\pi/2, 0\rangle$.

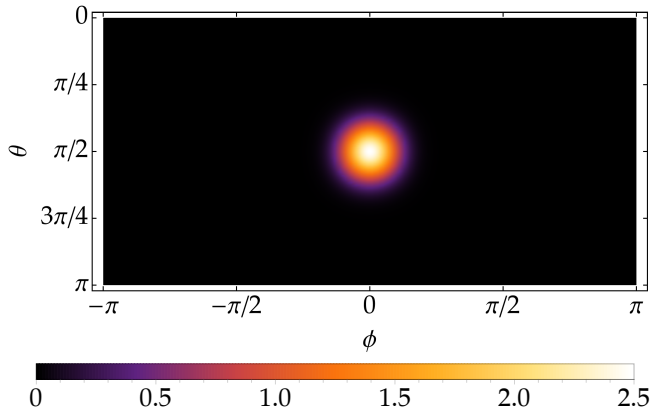

FIGURE 2.8: SU(2) Wigner function for a coherent spin state $|\pi/2, 0\rangle$ and $j = 10$. Similarly as in the case of canonical coherent state, the SU(2) Wigner function of a coherent spin state is almost identical to its SU(2) Husimi Q function.

2.6 Spin-squeezing

Spin-squeezing is a very broad topic, and here we only focus on its certain aspects relevant to quantum metrology. A comprehensive review on spin-squeezing can be found in Reference [173]. Depending on the context, the spin-squeezing parameter can be defined in various manners. One of its simplest definition is analogous to quadrature squeezing from Equation 1.4. The angular momentum operators uncertainty relation results from their commutation relation (Equation 1.6) and reads

$$\Delta^2 \hat{J}_a \Delta^2 \hat{J}_b \geq \frac{|\langle \hat{J}_c \rangle|^2}{4}.$$

According to this, spin-squeezing can be defined if one of the fluctuations on the left-hand side of the above equation satisfies

$$\Delta^2 \hat{J}_{a/b} \leq \frac{|\langle \hat{J}_c \rangle|}{2},$$

and therefore the squeezing parameter can be generally defined as

$$\xi_H^2 = \frac{2\Delta^2 \hat{J}_{\hat{n}}}{|\langle \hat{J}_{\hat{n}'} \rangle|},$$

where $\hat{n}$ and $\hat{n}'$ are two orthogonal unit vectors. This definition, however, is not practical since for certain choice of directions $\hat{n}$ and $\hat{n}'$ and a coherent spin state $|\theta, \phi\rangle$ it is below 1, which is not expected for coherent spin states since they should not be squeezed. This paradox appears because unlike the case of single-mode light where the variance of a canonical coherent state is direction invariant, the angular momentum operators variance for a coherent spin state depends on its direction $\hat{n}$, and therefore there exists the mean direction of the spin exactly along the $\hat{n}$ direction.

Another definition of spin-squeezing introduced by Kitagawa and Ueda in their seminal paper [174] is based on the mean direction of the spin $\hat{n}$ and the direction perpendicular to it $\hat{n}_\perp$. The variance of the angular momentum perpendicular to the mean direction of a coherent spin state is $\Delta^2 \hat{J}_{\hat{n}_\perp} = \frac{j}{2} = \frac{N}{4}$, therefore a state is said to be squeezed if the squeezing parameter defined as

$$\xi_S^2 = \frac{4 \min \Delta^2 \hat{J}_{\hat{n}_\perp}}{N},$$

is less than unity. For a coherent spin state, which is uncorrelated, we get $\xi_S^2 = 1$, and only in the presence of quantum correlations the squeezing parameter can be less than 1. A close relation between the squeezing parameter ξ_S^2 and quantities such as concurrence [175] and negative correlations [176] can be established.

The next important squeezing-parameter (ξ_R^2) was introduced by Wineland and his coworkers [177, 178] and is related to the Ramsey spectroscopy. In contrast to ξ_S^2, which is the analogue of quadrature squeezing, ξ_R^2 is related to the sensitivity of states to rotations. As it will be shown in Section 2.9 the sensitivity of a phase measurement can be equal to

$$\Delta\theta = \frac{\Delta \hat{J}_{\hat{n}_\perp}}{|\langle \hat{J}_{\hat{n}} \rangle|}.$$

The above Equation, for a coherent spin state turns into

$$\Delta\theta = \frac{1}{\sqrt{N}},$$

which is the shot-noise limit or standard quantum limit, the limit of precision in atomic interferometry with uncorrelated atoms. On this basis the squeezing parameter ξ_R^2 is defined as

$$\xi_R^2 = \frac{N \Delta^2 \hat{J}_{\hat{n}_\perp}}{|\langle \hat{J}_{\hat{n}} \rangle|^2},$$

which can be understood as the ratio of the phase sensitivity of a generic state versus that of a coherent spin state. When ξ_R^2 is less than unity, a state is said to be spin squeezed, and, moreover, its phase sensitivity is improved over the shot noise. As a consequence, the phase sensitivity can be written as

$$\Delta\theta = \frac{\xi_R}{\sqrt{N}}.$$

The lower bound of the phase sensitivity can be read out from the Heisenberg uncertainty relation

$$\Delta^2 \hat{J}_{\hat{n}_\perp} \Delta^2 \hat{J}_{\hat{n}'_\perp} \geq \frac{|\langle \hat{J}_{\hat{n}} \rangle|^2}{4},$$

and therefore

$$\xi_R^2 \frac{4\Delta^2 \hat{J}_{\hat{n}'_\perp}}{N} \geq 1.$$

The left side of the above equation has a maximal value for a state that is a superposition of eigenstates with maximal and minimal eigenvalues of $\hat{J}_{\hat{n}'_\perp}$ operator, for which $\Delta^2 \hat{J}_{\hat{n}'_\perp} = N^2/4$, and thus we get

$$\xi_R^2 \geq \frac{1}{N},$$

the so-called Heisenberg limit [179].

Lastly, let us introduce the spin-squeezing parameter (ξ_E^2) related to many-body entanglement [180]. This parameter ξ_E^2 is defined as follows

$$\xi_E^2 = \frac{N\Delta^2 \hat{J}_{\hat{n}_1}}{\langle \hat{J}_{\hat{n}_2} \rangle^2 + \langle \hat{J}_{\hat{n}_3} \rangle^2},$$

where $\hat{n}_1$, $\hat{n}_2$, and $\hat{n}_3$ are three mutually orthogonal directions. Spin 1/2 many-body ensembles, such as two-mode Bose-Einstein condensates, are said to be entangled if $\xi_E^2 < 1$. According to this, spin squeezing is connected to many-body entanglement but not *vice versa*. An entangled state does not have to be squeezed. For a certain choice of directions, the ξ_E^2 parameter reduces to ξ_R^2.

2.7 Generation of spin-squeezed states

In this Section, we focus on two methods of generating spin-squeezed states which were proposed by Masahiro Kitagawa and Masahito Ueda [174]. These methods are called one-axis twisting and two-axis twisting, named after its characteristic effect when applied to coherent spin states.

The one-axis twisting is one of the most commonly studied mechanisms of generating spin-squeezed state [181–190]. It is analogous to the photonic squeezing operator from Equation 1.4 and was implemented in Bose-Einstein condensates via atomic collisions [126, 180, 181, 191, 192] and in atomic ensembles [182, 183, 185, 188, 190, 193]. Furthermore, one-axis twisting can be studied analytically.

The original one-axis twisting Hamiltonian [174] reads

$$\hat{H}_{\mathrm{OAT}} = \chi \hat{J}_z^2,$$

but, in principle, any Hamiltonian proportional to $\hat{J}_{\hat{n}}^2$ is, up to a rotation, equivalent to the original one. This Hamiltonian also describes a non-linear quantum rotor [194]. The action of this Hamiltonian can be pictured by choosing the initial state to be the eigenstate of the $\hat{J}_x$ operator with eigenvalue $\frac{N}{2}$, *i.e.* $|\pi/2, 0\rangle$ depicted in Figure 2.7 and 2.8. The effect of the one-axis twisting Hamiltonian on a general state

$|\psi\rangle = \sum_{m=-j}^{j} c_m |j,m\rangle$ is

$$|\psi(\mu)\rangle = \sum_{m=-j}^{j} c_m e^{-it\hat{H}/\hbar} |j,m\rangle = \sum_{m=-j}^{j} c_m e^{-i\mu m^2} |j,m\rangle ,$$

with $\mu = \chi t/\hbar$ and c_m being the decomposition coefficients in the Dickie basis. From the Equation above, it is clear that every Dickie state in the decomposition experience a phase shift that is proportional to m^2, so there is symmetry with respect to state with positive m and negative m. Moreover, the phase shift is proportional to the second power of m, therefore it is not linear, and states with high m will acquire phase shift faster than states with low m, leading to a characteristic twisting, visible in Figure 2.9. The relevant quantities and the squeezing parameter ξ_R^2 for a state from Equation 2.7 with initial condition $|\pi/2, 0\rangle$ as a function of μ are shown in Figure 2.10 and, 2.11 respectively.

The means and variances of the angular momentum operators can be analytically calculated [174], and they become

$$\langle \hat{J}_x \rangle = \frac{N}{2} \cos^{N-1} \mu, \qquad \langle \hat{J}_y \rangle = 0, \qquad \langle \hat{J}_z \rangle = 0,$$

and

$$\begin{aligned}
\Delta^2 \hat{J}_x &= \frac{N}{4} \left[N \left(1 - \cos^{2(N-1)} \mu \right) - \frac{1}{2}(N-1)A \right] \\
\Delta^2 \hat{J}_y &= \frac{N}{4} \left[1 + \frac{1}{4} (N-1) \left(A + \sqrt{A^2 + B^2} \cos(2\delta) \right) \right] \\
\Delta^2 \hat{J}_z &= \frac{N}{4} \left[1 + \frac{1}{4} (N-1) \left(A - \sqrt{A^2 + B^2} \cos(2\delta) \right) \right],
\end{aligned}$$

where we defined $A = \left(1 - \cos^{N-2}(2\mu)\right)$, $B = 4 \sin\mu \cos^{N-2}\mu$, and $\delta = \frac{1}{2} \arctan \frac{B}{A}$. As can be seen from the above Equations and Figure 2.9, these variances, specifically these of $\hat{J}_y$ and $\hat{J}_z$, are not minimal nor maximal. These are given when we rotate the state around the x axis by angle $\nu = \frac{\pi}{2} - \delta$ or $\nu = -\delta$, so that we have

$$\begin{aligned}
\Delta^2 \hat{J}_x &= \frac{N}{4} \left[N \left(1 - \cos^{2(N-1)} \mu \right) - \frac{1}{2}(N-1)A \right] \\
\Delta^2 \hat{J}_{\perp \max} &= \frac{N}{4} \left[1 + \frac{1}{4} (N-1) \left(A + \sqrt{A^2 + B^2} \right) \right] \\
\Delta^2 \hat{J}_{\perp \min} &= \frac{N}{4} \left[1 + \frac{1}{4} (N-1) \left(A - \sqrt{A^2 + B^2} \right) \right].
\end{aligned}$$

A variation of the one-axis twisting Hamiltonian was studied in Reference [186], where the quadratic term was accompanied by a transverse control field

$$\hat{H} = \chi \hat{J}_z^2 + \Omega \hat{J}_x,$$

which is exactly the Bose-Hubbard model from Equation 2.2. It has been shown [195] that this type of Hamiltonian provides an optimal mechanism for creating spin-squeezed states regarding phase sensitivity of the Ramsey spectroscopy and in terms of linear interferometry whatsoever.

The two-axis twisting (originally two-axis counter-twisting) relies on a simultaneous twisting of the initial coherent clockwise and counterclockwise with respect

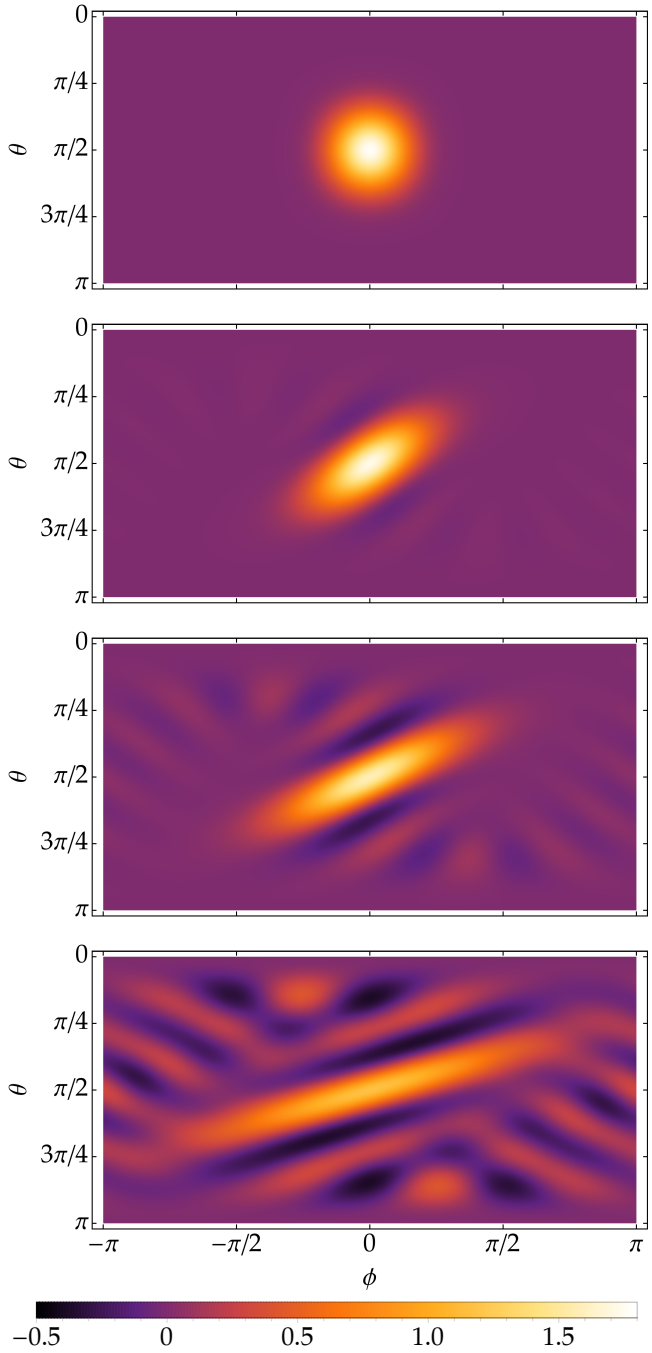

FIGURE 2.9: The evolution of SU(2) Wigner function of the coherent spin state $|\pi/2, 0\rangle$ under the action of one-axis twisting Hamiltonian. The panel depicts twisted coherent spin state for four different values of μ. In the top panel, we see the initial coherent spin state with $\mu = 0$. In the second panel, we see a moderately squeezes state for $\mu = 0.1$. The third panel shows almost maximally squeezed state $\mu = 0.2$. Finally, the bottom panel shows a states that is no longer squeezed $\mu = 0.4$. In contrast to the Wigner function from Equation 1.3, the SU(2) Wigner function of squeezed spin states exhibits interference fringes. See also Figure 2.11. The simulation performed for $N = 10$ atoms.

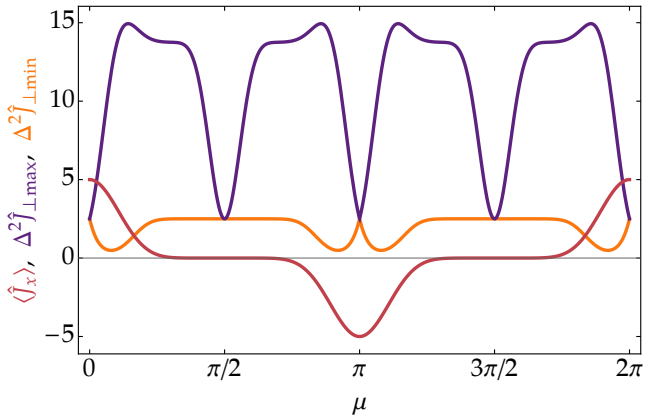

FIGURE 2.10: The average value of $\hat{J}_x$ operator from Equation 2.7 and maximal and minimal variances from Equation 2.7 as a function of μ. The evolution has a periodicity of 2π. The optimally spin-squeezed state is generated 4 times during a full period. Simulation performed for $N = 10$ atoms.

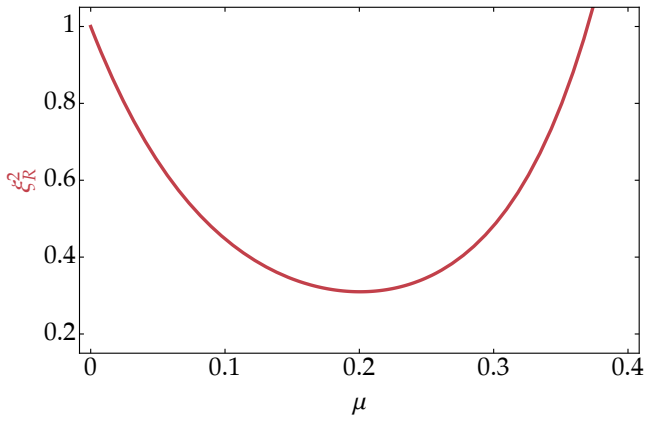

FIGURE 2.11: The spin-squeezing parameter ξ_R^2 as a function of μ. Simulation performed for $N = 10$ atoms. The squeezing parameter is optimised for μ such that the the average value of $\hat{J}_x$ operator is still of the order of $\frac{N}{4}$ and the minimal variance is almost at its minimal value. In the limit of $N \gg 1$, we obtain $\xi_R^2 \sim N^{-2/3}$.

two orthogonal directions in the plane perpendicular to the direction of the main spin. The original two-axis twisting Hamiltonian squeezes the initial coherent spin state $|0, \phi\rangle$ with respect to $\hat{J}_x$ and $\hat{J}_y$ by twisting it about the two axes in the $\theta = \frac{\pi}{2}$, $\phi = \pm\frac{\pi}{4}$ directions. The Hamiltonian of two-axis counter-twisting can be written as

$$\hat{H}_{\mathrm{TAT}} = \frac{\chi}{2i}\left(\hat{J}_+^2 - \hat{J}_-^2\right),$$

which is analogous to the squeeze operator from Equation 1.4. For the purpose of this dissertation, however, we will rotate our system around the y axis [196] and squeeze the initial coherent state $|\pi/2, 0\rangle$ with the two-axis twisting Hamiltonian of

the following form

$$\hat{H}_{\mathrm{TAT}} = \chi \left(\hat{J}_x^2 + \hat{J}_y^2 \right).$$

The two-axis twisting model is not solvable analytically for an arbitrary number of atoms N. Nevertheless, it has three advantages over the one-axis twisting. First, directions of the minimal and the maximal variances are fixed, which can be seen in Figure 2.14. Second, the level of squeezing is higher than that of the one-axis twisting. Last, the squeezing is faster. The relevant quantities and the squeezing parameter ξ_R^2 for two-axis twisting with initial condition $|\pi/2, 0\rangle$ as a function of μ are shown in Figure 2.12 and, 2.13 respectively.

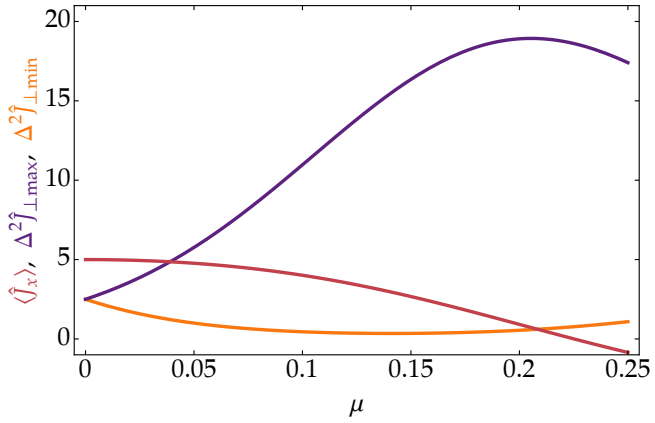

FIGURE 2.12: The average value of $\hat{J}_x$ operator and maximal and minimal variances as a function of μ. The evolution has no periodicity. Simulation performed for $N = 10$ atoms. For comparison see Figure 2.10

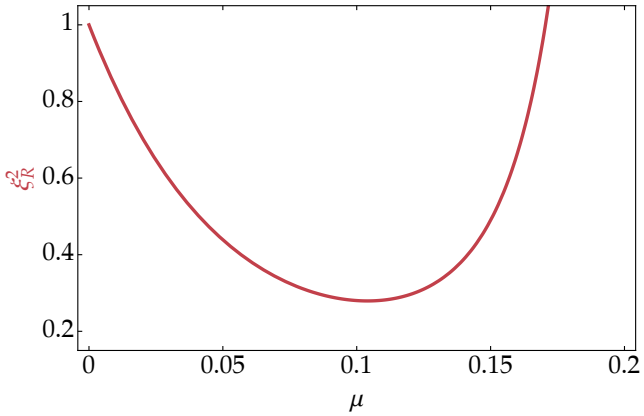

FIGURE 2.13: The spin-squeezing parameter ξ_R^2 as a function of μ for two-axis twisting Hamiltonian. Simulation performed for $N = 10$ atoms. When N is large, we get $\xi_R^2 \sim N^{-1}$. For comparison see Figure 2.11.

Despite its advantages in spin squeezing, the two-axis twisting Hamiltonian is not easy to treat experimentally. Various approaches to this problem were studied,

for instance, with Bose-Einstein condensed atoms [197], with collective spin states [198], with virtually excited Rydberg states [199], with multi-qubit systems [200], and even with dark-state polaritons [201].

The presented mechanisms do not exhaust the methods of creating spin-squeezed states and serve only to give some basic intuition about the phenomenon of spin squeezing. A more elaborated model should take into account decoherence [202], which is induced by interactions with the environment. In general, the decoherence effects can be described by three types of channels [203]: the amplitude damping, the phase damping, and the depolarisation. These prototype models of decoherence are relevant to various experimental setups and often lead to theoretical predictions in a good agreement with experimental data.

For example, a detailed analysis of squeezing dynamics in a two-mode Bose-Einstein condensate in the presence of particle loss was studied in Reference [204], where the authors derive the time evolution of the squeezing parameter

$$\xi_R^2(t,\Gamma_\mathrm{s}) = \xi_R^2(t)\left(1+\frac{1}{3}\frac{\Gamma_\mathrm{s} t}{\xi_R^2(t)}\right),$$

where $\xi_R^2(t)$ is the squeezing parameter without particle losses, and $\Gamma_\mathrm{s} = \sum_m \Gamma_\mathrm{s}^{(m)}$, and $\Gamma_\mathrm{s}^{(m)} = m\cdot\Gamma^{(m)}$, with $\Gamma^{(m)}$ being the m-body loss rate. In the limit of $N\to\infty$, for one-body losses ($m=1$), the optimal spin squeezing scales as

$$\xi_R^2 \propto N^{-4/15},$$

for two-body losses the optimal squeezing is independent of the number of particles, while for the three-body losses it scales as

$$\xi_R^2 \propto N^{4/15}.$$

Thus, only for one-body losses one can obtain arbitrarily small squeezing parameter.

2.8 Many-body entanglement

As discussed previously, the spin-squeezed states are entangled, but not every entangled state is spin-squeezed. A state of N particles in two modes is non-entangled (separable) when it can be written as [164, 205, 206]

$$\hat{\rho}_\mathrm{sep} = \sum_k p_k \hat{\rho}_k^{(1)}\otimes\hat{\rho}_k^{(2)}\otimes\ldots\otimes\hat{\rho}_k^{(N)},$$

where $p_k>0$, $\sum_k p_k = 1$, and $\hat{\rho}_k^{(i)}$ is the density matrix of the ith particle. In Reference [3], it has been shown that if a quantum state $\hat{\rho}$ satisfies

$$\chi^2 \equiv \frac{N}{F_Q\left[\hat{\rho},\hat{J}_{\hat{n}}\right]} < 1,$$

it is particle entangled, where

$$F_Q\left[\hat{\rho},\hat{J}_{\hat{n}}\right] = 4\Delta^2\hat{R}$$

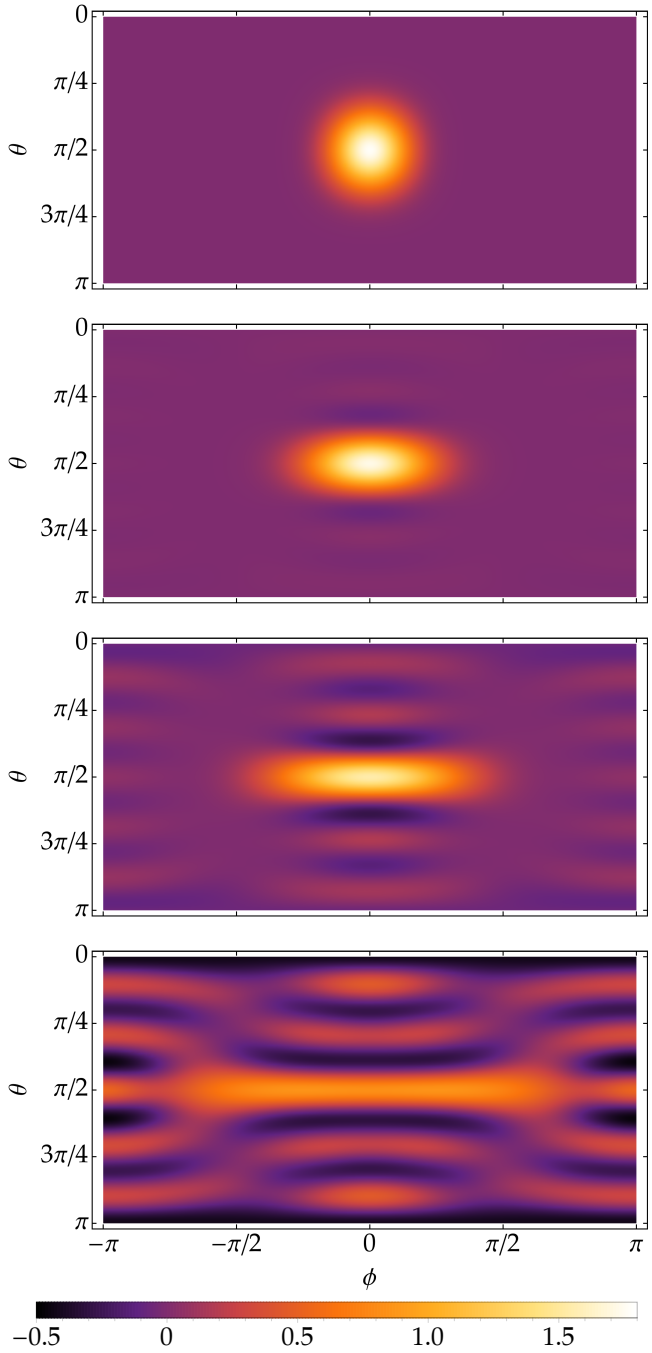

FIGURE 2.14: The evolution of SU(2) Wigner function of the coherent spin state $|\pi/2, 0\rangle$ under the action of two-axis twisting Hamiltonian. The panel depicts twisted coherent spin state for four different values of μ. In the top panel, we see the initial coherent spin state with $\mu = 0$. In the second panel, we see a moderately squeezed state for $\mu = 0.05$. The third panel shows almost optimally squeezed state $\mu = 0.1$. Finally, the bottom panel shows a states that is no longer squeezed $\mu = 0.2$. See also Figure 2.13. The simulation performed for $N = 10$ atoms.

is the quantum Fisher information [2, 207, 208] and $\hat{n}$ is an arbitrary direction. Equation 2.8 recognises a family of states that are entangled $\chi^2 < 1$ and not spin squeezed

$\xi_R^2 > 1$ such as the maximally entangled state [176]. The Hermitian operator $\hat{R}$ is the solution of the equation

$$\{\hat{R}, \hat{\rho}\} = i\left[\hat{J}_{\hat{n}}, \hat{\rho}\right].$$

For pure states, this Equation is solved by

$$\hat{R} = i\left[\hat{J}_{\hat{n}}, \hat{\rho}\right],$$

therefore, we have $\Delta^2 \hat{R} = \Delta^2 \hat{J}_{\hat{n}}$ [209–211] and consequently

$$\chi^2 \equiv \frac{N}{4\Delta^2 \hat{J}_{\hat{n}}},$$

which resembles squeezing parameters ξ_S^2. The quantum Fisher information is naturally related to the problem of phase estimation, which is further studied in the next Chapter.

Let us now focus on the following inequality

$$F_Q\left[\hat{\rho}, \hat{J}_{\hat{n}}\right] \leq 4\Delta^2 \hat{J}_{\hat{n}}.$$

The fictitious angular momentum operator can be written as a sum of Pauli matrices acting on every particle

$$\hat{J}_n = \frac{1}{2}\sum_{i=1}^{N} \hat{\sigma}_{\hat{n}}^{(i)},$$

where $\hat{\sigma}_{\hat{n}}^{(i)}$ is a Pauli matrix operating on the ith particle. For a product state

$$\hat{\rho}_k = \hat{\rho}_k^{(1)} \otimes \hat{\rho}_k^{(2)} \otimes \ldots \otimes \hat{\rho}_k^{(N)},$$

we have

$$4\Delta^2 \hat{J}_{\hat{n}} = N - \sum_{i=1}^{N} \left\langle \sigma_{\hat{n}}^{(i)} \right\rangle^2 \leq N,$$

and therefore, we have $\chi^2 \geq 1$ where the equality sign can be saturated only with pure states. On the other hand, we have

$$4\Delta^2 \hat{J}_{\hat{n}} \leq 4\left\langle \hat{J}_{\hat{n}}^2 \right\rangle \leq N^2,$$

and therefore in general $\chi^2 \geq N$ where the equality sign can be saturated only with maximally entangled states.

Note that the condition from Equation 2.8 depends not only on the initial state but also on the direction $\hat{n}$. A particle-entangled state can have $\chi^2 > 1$ if the direction $\hat{n}$ is chosen inappropriately, and thus $\chi^2 < 1$ is not a necessary condition for particle entanglement. The problem of inconclusive condition for entanglement disappears when one introduces the dynamical susceptibility [212] defined as

$$\mathcal{F}\left[\hat{\rho}\right] = \max_{\hat{n}} F_Q\left[\hat{\rho}, \hat{J}_{\hat{n}}\right].$$

The name is inspired by the interpretation of quantum Fisher information as a susceptibility of the state to change due to a linear rotation, which will be further discussed in the next Chapter.

It turns out that the one-axis twisting Hamiltonian is an excellent tool for creating particle-entangled states [213]. This is presented in detail in Chapter 4. The spin-squeezing parameter $\hat{\xi}_R^2$, quantum Fisher information with respect to x direction $F_Q\left[\hat{\rho}, \hat{J}_{\hat{x}}\right]$, and the dynamical susceptibility $\mathcal{F}\left[\hat{\rho}\right]$ for the state from Equation 2.7 with initial condition $\langle \pi/2, 0|$ are presented in Figure 2.15

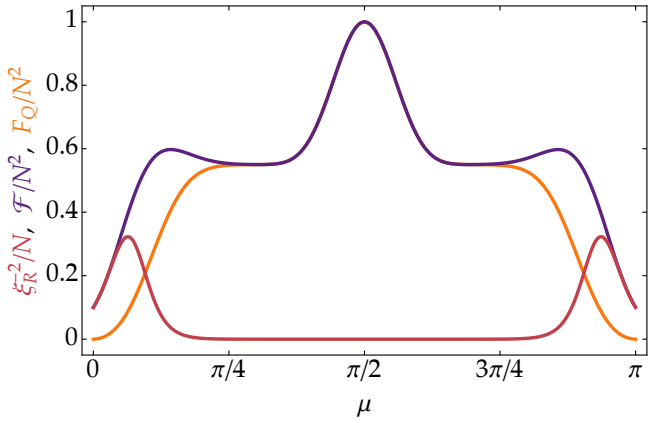

FIGURE 2.15: The spin-squeezing parameter $\hat{\xi}_R^2$, quantum Fisher information with respect to x direction $F_Q\left[\hat{\rho}, \hat{J}_{\hat{x}}\right]$, and the dynamical susceptibility $\mathcal{F}\left[\hat{\rho}\right]$ for the state from Equation 2.7 with initial condition $\langle \pi/2, 0|$ normalised to 1 as a function of μ. The squeezing parameter is able initially to sense the correlations with the state, but its not able to grasp the correlations in the maximally entangled state for $\mu = \pi/2$.

2.9 Atomic quantum interferometry

Finally, let us consider atomic interferometry. First, we give a brief description of the Ramsey scheme [18], shown in Figure 2.16. Consider a system of N two-level particles which interact with an external magnetic field $\mathbf{B}$. Then, The Hamiltonian of the system reads

$$\hat{H} = -\mu_0 \mathbf{J} \cdot \mathbf{B},$$

where $\mu_0 \mathbf{J}$ stands for the magnetic moment and

$$\mathbf{B} = B_0 \hat{n}_z + \mathbf{B}_1,$$

is a magnetic field with a static part

$$B_0 = -\hbar\omega_0/\mu_0, \quad \mu_0 < 0,$$

and a time dependent part

$$\mathbf{B}_1 = B_1 \left(\hat{n}_y \sin(\omega t) + \hat{n}_x \cos(\omega t)\right).$$

The Hamiltonian in the rotating wave approximation becomes

$$\hat{H} = \hbar\left(\omega_0 - \omega\right)\hat{J}_z + \hbar\Omega\hat{J}_x,$$

where $\Omega = |\mu_0 B_1|/\hbar$ is the Rabi frequency. Since $\Omega \gg |\omega_0 - \omega|$, the above Hamiltonian is approximated as

$$\hat{H}_R = \hbar\Omega\hat{J}_x.$$

The Ramsey interferometry, shown in Figure 2.16, can be described in the following way. Initially, all the particles are in the ground state and $\mathbf{B}_1 = 0$, so the system is in the eigenstate of the Hamiltonian and only acquires a global phase. Next, the $\mathbf{B}_1$ field is turned on for a time of length $t_{\pi/2} = \pi/\left(2\Omega\right)$ acting effectively as a $\pi/2$-pulse that rotates the state on the equator, and therefore the state of the system is in the equal superposition of being in the ground and excited state. After the pulse, the state is rotating around z axis and acquires a relative phase $\phi = \left(\omega_0 - \omega\right)t$. Finally, there is another $\pi/2$ pulse. According to this, the evolution of the state can be written as

$$|\psi(t)\rangle = \hat{U}(t)\,|\psi(0)\rangle$$

with the unitary evolution operator

$$\begin{aligned}\hat{U}(t) &= e^{-i\frac{\pi}{2}\hat{J}_x}e^{i\phi\hat{J}_z}e^{-i\frac{\pi}{2}\hat{J}_x}\\ &= e^{-i\phi\hat{J}_y}e^{-i\pi\hat{J}_x}.\end{aligned}$$

Therefore the Ramsey interferometry is equivalent to the Mach-Zehnder interferometry from Equation 1.6 modulo a rotation of the probe state around the x axis by π which effectively amounts to the flip of the Bloch sphere or the transformation $x \to x$, $y \to -y$, and $z \to -z$. The Ramsey interferometry and Mach-Zehnder interferometry are equivalent [177, 214]. The balanced beam splitters are identical in effect to $\pi/2$ pulses, while the phase shift accumulated during the precession of the magnetic moment around the z axis between the two $\pi/2$ pulses amounts to the relative phase shift. Usually, in Ramsey spectroscopy, the two modes are the two internal atomic levels [18] which can be coupled to external motional degrees of freedom [215]. In Mach-Zehnder interferometry, on the contrary, the two modes are the separated regions in space [216] as in the case of a double-well Bose-Einstein condensate.

In order to estimate ϕ, we could now, for instance, measure the occupation of the excited state, which amounts to measuring the average value of $\hat{J}_z$

$$\langle\hat{J}_z(t)\rangle = \langle\hat{J}_x\rangle\sin\phi - \langle\hat{J}_z\rangle\cos\phi,$$

calculated analogously to Equation 1.6. For small ϕ such that $\sin\phi \approx 0$, the ϕ is related to the measurement of $\langle\hat{J}_z(t)\rangle$ via

$$\phi = \arccos\left(-\frac{\langle\hat{J}_z(t)\rangle}{\langle\hat{J}_z\rangle}\right),$$

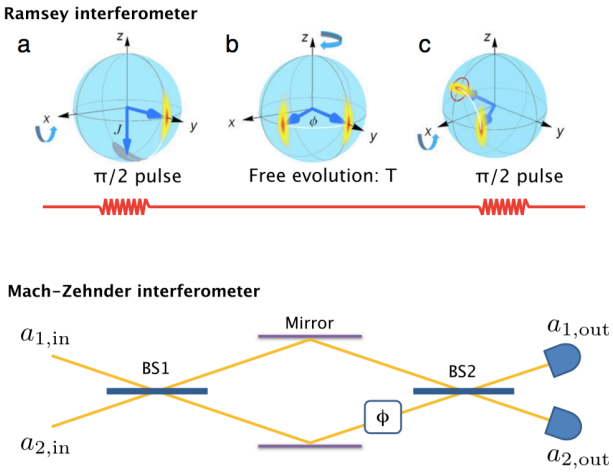

FIGURE 2.16: Schematic representation of the Ramsey (top) and Mach-Zehnder (bottom) interferometry. The blue arrows inside the Bloch sphere represent the initial and final direction of the mean spin. The multi-colour disks represent the uncertainty of the spin components. The red circle in (c) is the uncertainty of a coherent spin state. In the Mach-Zehnder interferometer, the two beams are injected both input ports of the first beam splitter, BS1. The relative phase difference gained between the input and output beamsplitters is denoted with ϕ. After the second beam splitter, BS2, detectors measure the relative number of photons (or atoms) which is related to the phase difference ϕ. The beam splitters correspond to the two $\pi/2$ pulses in the Ramsey process (a) and (c). The scheme reprinted from Reference [173].

and thus if one wanted to estimate ω_0 it would be related to $\langle \hat{J}_z(t) \rangle$ via

$$\omega_0 = \omega + \frac{1}{t} \arccos\left(-\frac{\langle \hat{J}_z(t) \rangle}{\langle \hat{J}_z \rangle} \right).$$

In practice, the experiment is repeated m times, and the total time of the experiment is $T = m \cdot t$. Then, we can estimate the value of ϕ with the uncertainty according to the error propagation formula

$$\Delta^2 \phi = \frac{1}{m} \frac{\Delta^2 \hat{J}_z(t)}{\left(\partial_\phi \langle \hat{J}_z(t) \rangle \right)^2},$$

which for $\phi \ll 1$ becomes

$$\Delta^2 \phi = \frac{1}{m} \frac{\Delta^2 \hat{J}_z(t)}{\langle \hat{J}_x \rangle^2}.$$

This result can be rewritten using the squeezing parameter ξ_R^2 from Equation 2.6 yielding

$$\Delta^2 \phi = \frac{1}{m} \frac{\xi_R^2}{N}.$$

For coherent spin states the above Equation can give minimally the shot-noise limit

$$\Delta^2\phi = \frac{1}{m}\frac{1}{N},$$

which can be overcome with using the squeezed spin states.

Now, we can ask whether the estimation from the population imbalance is the optimal choice of the estimation procedure. As it is clear from the above equation, the estimation from population imbalance is connected with the squeezing parameter ξ_R. However, there are far more exotic states than the squeezed spin states, with respect to non-classical correlations as can be seen in Figure 2.15. In principle, there might exist a measurement, different from measuring the population imbalance, which can fully benefit from the non-classical correlations present in a given quantum state. Furthermore, we can ask in general how precise a statistical estimation can be, whether there is some fundamental limit, and what are the factors that limit the precision of estimation of an unknown parameter. To answer this type of questions, we need to delve into the theory of estimation, which is the subject of the next Chapter.

Chapter 3

Theory of Estimation

The theory of estimation aims at determining the values of unknown parameters based on a set of measured data that is governed by probability distribution dependent on the parameters of interest. This objective is achieved by using the so-called estimator which attempts to approximate the unknown parameter with the highest possible accuracy. What kind of estimators gives the best accuracy? Is there a fundamental limit of accuracy? What kind of measurements are best suited for estimating an unknown parameter? These are the key questions in statistical inference, first answered by Rao [217], Cramér [218], Fréchet [219], and Darmois [220], who independently found a lower bound on the variance of an arbitrary estimator, generally known as the Cramér-Rao lower bound. It is innately connected with the Fisher information, first introduced by Fisher [221]. Thus, the Fisher information plays a key role in the theory of estimation.

In the quantum kingdom, the choice of possible measurements is overwhelming. The optimisation of the Fisher information over quantum measurements leads to the quantum Fisher information [2, 222], and consequently the quantum Cramér-Rao bound [207, 223, 224].

Contents

3.1 Measurement, probability, and estimator

The first step of the process of estimation is the measurement from which one can deduce the value of an unknown parameter. In quantum theory, the most general measurement is given by a positive-operator valued measure, *i.e.*, a set of non-negative hermitian operators $\hat{M}(m)$ which are normalised

$$\sum_m \hat{M}(m) = \hat{I},$$

where m denotes the possible measurement outcomes. The conditional probability of observing the result m for a given unknown parameter θ, also known as likelihood function [225], is

$$P(m|\theta) = \mathrm{Tr}\left[\hat{M}(m)\hat{\rho}(\theta)\right],$$

where $\hat{\rho}(\theta)$ is the output quantum state dependent on the unknown parameter θ (see Section 2.9 and 1.6). The measurement is usually repeated many times, and if the probe state consists of n uncorrelated (separable) parts

$$\hat{\rho} = \hat{\rho}^{(1)} \otimes \hat{\rho}^{(2)} \otimes \ldots \otimes \hat{\rho}^{(n)},$$

and we perform local operations (operations that do not entangle the initial state) on the probe state, such that

$$\hat{\rho} = \hat{\rho}^{(1)}(\theta) \otimes \hat{\rho}^{(2)}(\theta) \otimes \ldots \otimes \hat{\rho}^{(n)}(\theta),$$

and statistically independent measurements

$$\hat{M}(\mathbf{m}) = \hat{M}^{(1)}(m_1) \otimes \hat{M}^{(2)}(m_2) \otimes \ldots \otimes \hat{M}^{(n)}(m_n),$$

where $\mathbf{m} = \{m_1, m_2, \ldots, m_n\}$, the likelihood becomes a product of the single measurement probabilities

$$P(\mathbf{m}|\theta) = \prod_{i=1}^{n} P(m_i|\theta) = \prod_{i=1}^{n} \mathrm{Tr}\left[\hat{M}^{(i)}(m_i)\hat{\rho}^{(i)}(\theta)\right].$$

In analytical calculations it is sometimes convenient to introduce the log-likelihood function

$$L(\mathbf{m}|\theta) \equiv \ln P(\mathbf{m}|\theta).$$

Another relevant object in the phase estimation is the so-called estimator $\Theta(\mathbf{m})$, which is a mapping from the space of $\mathbf{m}$ into the space of θ. In other words, the estimator is a function that takes as an argument the set of outcomes $\mathbf{m}$ and yields an estimate of θ. From the practical point of view, the estimator should be chosen cautiously. An important example of an estimator is the maximum-likelihood estimator which we go back to in Section 3.3. Since an estimator is a function of outcomes $\mathbf{m}$ that are random, it constitutes itself a random variable and characterised by its mean value which is dependent on θ

$$\langle\Theta\rangle = \sum_{\mathbf{m}} P(\mathbf{m}|\theta)\Theta(\mathbf{m})$$

and its variance

$$\Delta^2\Theta = \sum_{\mathbf{m}} P(\mathbf{m}|\theta)\left(\Theta(\mathbf{m}) - \langle\Theta\rangle\right).$$

The exemplary estimation data is presented in histogram in Figure 3.1.

The best estimators are unbiased and provide the smallest uncertainty. An estimator is unbiased if its statistical average converges to the true value of the unknown parameter θ

$$\langle\Theta\rangle = \theta.$$

for all values of θ. Thus, for unbiased estimators

$$\partial_\theta \langle\Theta\rangle = 1,$$

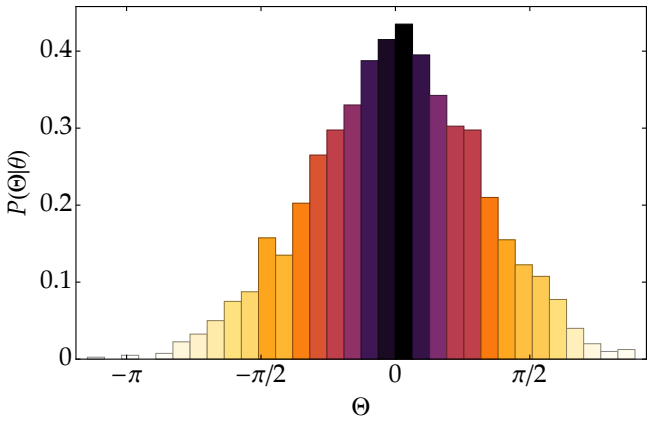

FIGURE 3.1: A histogram presenting exemplary data of Θ . The average value of the histogram $\langle\Theta\rangle$ is the estimate of the unknown parameter θ, whilst its width reflects the uncertainty. For large n the histogram tends to a Gaussian distribution which is a consequence of the central limit theorem, which states that in most situations, when independent random variables are added, their properly normalised sum tends toward a Normal distribution even if the original variables themselves are not normally distributed. Here $n = 2000$.

otherwise an estimator is biased. Another important feature of an estimator is consistency. An estimator $\Theta(\mathbf{m})$ is consistent if it converges in probability to θ, *i.e.*

$$\lim_{n\to\infty} \Theta(\mathbf{m}) - \theta = 0, \quad \forall\theta,$$

where n is the sample size (number of measurements). Consequently, a consistent estimator is asymptotically unbiased

$$\lim_{n\to\infty} \langle\Theta\rangle = \theta.$$

3.2 Cramér-Rao bound

The Cramér-Rao bound is essential in the theory of phase estimation since it sets a lower bound on the variance of an arbitrary estimator

$$\Delta^2\Theta \geq \frac{\left(\partial_\theta \langle\Theta\rangle\right)^2}{F(\theta)},$$

which for unbiased estimators simply reads

$$\Delta^2\Theta \geq \frac{1}{F(\theta)},$$

with $F(\theta)$ being the classical Fisher information

$$F(\theta) = \sum_{\mathbf{m}} \frac{1}{P(\mathbf{m}|\theta)} \left(\partial_\theta P(\mathbf{m}|\theta)\right)^2,$$

whose quantum counterpart was introduced in the previous Chapter.

An estimator which saturates the Cramér-Rao bound is called efficient. Although there is no proof that it exists for an arbitrary number of measurements, it can be shown that in the limit of a large number of measurements the maximum likelihood estimator is always efficient.

To derive the Cramér-Rao bound, let us take a derivative of Equation 3.1 with respect to θ

$$\begin{aligned}\partial_\theta \langle\Theta\rangle &= \partial_\theta \sum_{\mathbf{m}} P(\mathbf{m}|\theta)\Theta(\mathbf{m}) \\ &= \sum_{\mathbf{m}} P(\mathbf{m}|\theta)\Theta(\mathbf{m})\partial_\theta L(\mathbf{m}|\theta) \\ &= \langle\Theta(\mathbf{m})\partial_\theta L(\mathbf{m}|\theta)\rangle\,,\end{aligned}$$

where we have used the fact that

$$\partial_\theta L(\mathbf{m}|\theta) \equiv \partial_\theta \ln P(\mathbf{m}|\theta) = \frac{1}{P(\mathbf{m}|\theta)}\partial_\theta P(\mathbf{m}|\theta),$$

and notice that ($\sum_{\mathbf{m}} P(\mathbf{m}|\theta) = 1$)

$$\partial_\theta \sum_{\mathbf{m}} P(\mathbf{m}|\theta) = \sum_{\mathbf{m}} P(\mathbf{m}|\theta)\partial_\theta L(\mathbf{m}|\theta) = \langle\partial_\theta L(\mathbf{m}|\theta)\rangle = 0.$$

According to this, we can write

$$\left(\partial_\theta \langle\Theta\rangle\right)^2 = \left\langle\left(\Theta(\mathbf{m}|\theta) - \langle\Theta\rangle\right)\partial_\theta L(\mathbf{m}|\theta)\right\rangle^2.$$

The next step is to use the Cauchy-Schwartz inequality, which states that for any two integrable real functions $f(x)$ and $g(x)$ we have

$$\langle f^2\rangle\langle g^2\rangle \geq \langle fg\rangle^2,$$

which is saturated if $f = \lambda g$, with λ independent of $\mathbf{m}$. Now if we choose

$$f = \Theta(\mathbf{m}|\theta) - \langle\Theta\rangle \quad \text{and} \quad g = \partial_\theta L(\mathbf{m}|\theta),$$

and apply the Cauchy-Schwartz inequality to Equation 3.2, we obtain

$$\left\langle\left(\Theta(\mathbf{m}|\theta) - \langle\Theta\rangle\right)^2\right\rangle\left\langle\left(\partial_\theta L(\mathbf{m}|\theta)\right)^2\right\rangle \geq \left(\partial_\theta \langle\Theta\rangle\right)^2,$$

which is equivalent to Equation 3.2. For a case from Equation 3.1 where $\mathbf{m}$ are independent and identical measurements, so also the probabilities $P(\mathbf{m}|\theta)$ are independent, the classical Fisher information can be rewritten in the following way

$$\begin{aligned}F(\theta) &= \sum_{m_i} \frac{1}{\prod_{i=1}^n P(m_i|\theta)} \left(\partial_\theta \prod_{i=1}^n P(m_i|\theta)\right)^2 \\ &= n\sum_m \frac{1}{P(m|\theta)}\left(\partial_\theta P(m|\theta)\right)^2,\end{aligned}$$

and consequently the Cramér-Rao bound for an unbiased estimator reads

$$\Delta^2\Theta \geq \frac{1}{n \cdot F(\theta)}.$$

Let us return to the the Cramér-Rao bound. The condition for its saturation becomes

$$\lambda \left(\Theta(\mathbf{m}|\theta) - \langle\Theta\rangle\right) = \frac{1}{P(\mathbf{m}|\theta)} \partial_\theta P(\mathbf{m}|\theta),$$

which can be rewritten in the following way

$$P(\mathbf{m}|\theta)\lambda \left(\Theta(\mathbf{m}|\theta) - \langle\Theta\rangle\right) = \partial_\theta P(\mathbf{m}|\theta),$$

and finally solved analytically by a Gaussian function

$$P(\mathbf{m}|\theta) \propto e^{-\frac{1}{2}\lambda(\Theta(\mathbf{m}|\theta)-\langle\Theta\rangle)^2},$$

which means that estimating from the mean value saturates the Cramér-Rao bound given the statistics are Gaussian. In general the estimator that can asymptotically saturate the Cramér-Rao bound is the aforementioned maximum likelihood estimator.

3.3 Maximum likelihood estimator

The maximum likelihood estimator is defined as

$$\hat{\Theta}(\mathbf{m}) = \arg\max_{\vartheta} P(\mathbf{m}|\vartheta),$$

which means that it is the value of ϑ that maximises the likelihood function for a given sequence of measurements outcomes $\mathbf{m}$. In order to obtain it, the probability has to be known, and then the maximum likelihood estimator $\hat{\Theta}(\mathbf{m})$ can be found with the help of the following conditions

$$\partial_\vartheta P(\mathbf{m}|\vartheta)\Big|_{\hat{\Theta}(\mathbf{m})} = 0 \quad \text{and} \quad \partial_\vartheta^2 P(\mathbf{m}|\vartheta)\Big|_{\hat{\Theta}(\mathbf{m})} < 0.$$

Since the measurement outcomes $\mathbf{m}$ are randomly distributed according to the probability $P(\mathbf{m}|\theta)$, the distribution of $\hat{\Theta}(\mathbf{m})$ is also random. In order to calculate the variance of the maximum likelihood estimator, we need to perform the estimation many times ($n \gg 1$) and construct a histogram like in Figure 3.1.

The maximum likelihood estimator is asymptotically consistent. This can be proven with the log-likelihood from Equation 3.1. Since the maximum likelihood estimator is defined as the maximum of the likelihood, we can subtract from it any constant. In particular, we can subtract the likelihood with the true value of the unknown parameter

$$\begin{aligned} L(\mathbf{m}|\vartheta) - L(\mathbf{m}|\theta) = \ln \frac{P(\mathbf{m}|\vartheta)}{P(\mathbf{m}|\theta)} &= \sum_{i=1}^{n} \ln \frac{P(m_i|\vartheta)}{P(m_i|\theta)} \\ &\xrightarrow{n\to\infty} n \int \mathrm{d}m\, P(m|\vartheta) \ln \frac{P(m|\vartheta)}{P(m|\theta)}, \end{aligned}$$

where θ is the true value of the parameter. This integral can be bounded from above by using $\ln \xi \leq \xi - 1$, thus yielding

$$\int \mathrm{d}m\, P(m|\vartheta) \ln \frac{P(m|\vartheta)}{P(m|\theta)} \leq \int \mathrm{d}m\, P(m|\vartheta) \left(\frac{P(m|\vartheta)}{P(m|\theta)} - 1 \right) = 0,$$

which means that the maximal value of thus constructed maximum likelihood estimator is 0, so when

$$L(\mathbf{m}|\vartheta) = L(\mathbf{m}|\theta),$$

which can only happen if $\vartheta = \theta$, therefore the maximum likelihood estimator is consistent in the limit of $n \to \infty$

$$\lim_{n\to\infty} \langle \hat{\Theta} \rangle = \theta.$$

For a sufficiently large number of measurements, the distribution of the maximum likelihood estimator becomes a Gaussian centred at the true value θ with the variance equal to the inverse of the Fisher information

$$P(\hat{\Theta}|\theta) = \sqrt{\frac{nF(\theta)}{2\pi}} e^{-\frac{nF(\theta)}{2}\left(\hat{\Theta}-\theta\right)^2},$$

therefore, according to Equation 3.2, the maximum likelihood estimator is asymptotically efficient. Another way of proving its efficiency is to expand the derivative of log-likelihood function with respect to ϑ in Taylor series around θ

$$\partial_\vartheta L(\mathbf{m}|\vartheta) = \partial_\vartheta L(\mathbf{m}|\vartheta)\Big|_\theta + \partial^2_\vartheta L(\mathbf{m}|\vartheta)\Big|_\theta (\vartheta - \theta) + O\left((\vartheta-\theta)^2\right).$$

Now, if we take ϑ to be the maximum likelihood estimator $\hat{\Theta}$, we can neglect the higher order terms since the maximum likelihood estimator is consistent, and thus obtain

$$(\hat{\Theta} - \theta) = -\frac{\partial_\vartheta L(\mathbf{m}|\vartheta)}{\partial^2_\vartheta L(\mathbf{m}|\vartheta)}\Big|_\theta.$$

Let us now focus on the denominator

$$\partial^2_\vartheta L(\mathbf{m}|\vartheta)\Big|_\theta = \sum_{i=1}^{n} \left[-\frac{1}{P^2(m_i|\theta)} \left(\partial_\vartheta P(m_i|\vartheta)\right)^2 \Big|_\theta + \frac{1}{P(m_i|\theta)} \partial^2_\vartheta P(m_i|\vartheta)\Big|_\theta \right],$$

which in the limit of large n can be replaced with an integral

$$\partial^2_\vartheta L(\mathbf{m}|\vartheta)\Big|_\theta = n \int \mathrm{d}m \left[-\frac{1}{P(m|\theta)} \left(\partial_\vartheta P(m|\vartheta)\right)^2 \Big|_\theta + \partial^2_\vartheta P(m|\theta)\Big|_\theta \right] = -nF(\theta).$$

With this result, we can rewrite Equation 3.3 in the following way

$$(\hat{\Theta} - \theta) = \frac{1}{nF(\theta)} \sum_{i=1}^{n} \left[\frac{1}{P(m_i|\theta)} \partial_\vartheta P(m_i|\vartheta)\Big|_\theta \right].$$

The object in the square brackets is a random variable since the outcome of the measurement is random by itself. Now, we can use the central limit theorem which states

that if an object is an average of n random variables, then for $n \to \infty$ its distribution is Gaussian with a mean

$$\langle \hat{\Theta} - \theta \rangle = \frac{1}{F(\theta)} \int \mathrm{d}n P(m|\theta) \left[\frac{1}{P(m|\theta)} \partial_\vartheta P(m|\vartheta) \Big|_\theta \right] = \frac{1}{F(\theta)} \int \mathrm{d}n \left[\partial_\vartheta P(m|\vartheta) \Big|_\theta \right] = 0$$

which means that the maximum likelihood estimator is asymptotically unbiased, and its variance is

$$\Delta^2 \hat{\Theta} = \frac{1}{n} \frac{1}{F^2(\theta)} \int \mathrm{d}n P(m|\theta) \left[\frac{1}{P(m|\theta)} \partial_\vartheta P(m|\vartheta) \Big|_\vartheta \right]^2 = \frac{1}{n \cdot F(\theta)},$$

which means that the maximum likelihood estimator is asymptotically efficient. When the number of measurements n is small or the maximum likelihood estimator is biased for finite number of measurements, it is still possible to perform a phase estimation with a Bayesian approach which we will not cover in this dissertation. For more details about the Bayesian inference, see Reference [226]. The maximum likelihood estimation has been exploited in several experiments [63, 64, 227–229].

3.4 Estimation from the mean

In order to use the maximum likelihood estimator, we need to know the probability $P(\mathbf{m}|\theta)$ for all possible values of θ and set of measurement outcomes $\mathbf{m}$. Usually, the knowledge of the probability can be provided by the underlying theory or by using the so-called calibration of the interferometer. From the practical point of view, however, the extraction of $P(\mathbf{m}|\theta)$ may be difficult within a limited amount of time or resources and in some cases practically impossible. An alternative way of estimating the value of an unknown parameter would be to measure some quantity described by an observable $\hat{O}$, with θ-dependent mean value $\langle \hat{O}(\theta) \rangle$ and θ-dependent variance $\Delta^2 \hat{O}(\theta)$, for instance, like in Section 2.9 where we used the mean value of $\hat{J}_z$ to estimate the value of the phase shift in the Ramsey scheme.

Let us revise this estimation scheme again from the perspective of Cramér-Rao bound (see Sections 1.6 and 2.9). First, imagine, we estimate the value of the unknown parameter from every single measurement of $\hat{J}_z$. This is a very naive approach, and indeed, it can be shown that such an estimator is biased since we never collect enough statistics for the central limit theorem to work properly. If the input state is the coherent state polarised along the x axis, we have

$$\langle \hat{J}_z(\theta) \rangle = \cos\theta \langle \hat{J}_z \rangle + \sin\theta \langle \hat{J}_x \rangle = \sin\theta \langle \hat{J}_x \rangle ,$$

which is only valid if we repeat the measurement many times ($n \gg 1$), therefore creating an estimator from a single measurement is incorrect.

Now, instead, let us consider n measurements of observable $\hat{J}_z$, with results $m_1, m_2, \ldots, m_n$ and take the mean value

$$J_z \equiv \frac{1}{n} \sum_{i=1}^{n} m_i.$$

From the central limit theorem, we know that for large number of measurements ($n \to \infty$), the probability distribution of J_z is

$$P(J_z|\theta) = \sqrt{\frac{n}{2\pi\Delta^2\hat{J}_z(\theta)}} e^{-\frac{n\left(J_z - \langle\hat{J}_z(\theta)\rangle\right)}{2\Delta^2\hat{J}_z(\theta)}}.$$

Since the above probability is a function of the mean $\langle\hat{J}_z(\theta)\rangle$ and the variance $\Delta^2\hat{J}_z(\theta)$, a good estimator should be the maximum of the likelihood function $P(J_z|\theta)$ with J_z being a random variable:

$$\partial_\theta \ln P(J_z|\theta)\Big|_{\hat{\Theta}(J_z)} = 0 \quad \text{and} \quad \partial_\theta^2 \ln P(J_z|\theta)\Big|_{\hat{\Theta}(J_z)} < 0.$$

The first part of the above Equation reads:

$$n\left(J_z - \langle\hat{J}_z(\theta)\rangle\right)\partial_\theta\langle\hat{J}_z(\theta)\rangle + \frac{\partial_\theta\Delta^2\hat{J}_z(\theta)\left(n(J_z - \langle\hat{J}_z(\theta)\rangle)^2 - \Delta^2\hat{J}_z(\theta)\right)}{2\Delta^2\hat{J}_z(\theta)} = 0,$$

which for large n becomes

$$\left(J_z - \langle\hat{J}_z(\theta)\rangle\right)\left(\partial_\theta\langle\hat{J}_z(\theta)\rangle + \frac{J_z - \langle\hat{J}_z(\theta)\rangle}{2\Delta^2\hat{J}_z(\theta)}\partial_\theta\Delta^2\hat{J}_z(\theta)\right) = 0,$$

which has only one solution $J_z = \langle\hat{J}_z(\theta)\rangle$ that satisfies the second part of Equation 3.4. We can now introduce the function $f(\theta) = \langle J_z(\theta)\rangle$, and say that the estimator Θ is the value for which $f(\Theta) = J_z$:

$$\Theta = f^{-1}(J_z).$$

In the limit $n \to \infty$, we have $J_z \to \langle\hat{J}_z(\theta)\rangle$ and therefore $\Theta \to \theta$. In this limit the sensitivity is given by the Cramér-Rao bound with Fisher information

$$F(\theta) = \int \mathrm{d}J_z \frac{1}{P(J_z|\theta)}\left(\partial_\theta P(J_z|\theta)\right)^2.$$

which can be evaluated to give

$$F(\theta) = n\frac{\partial_\theta\langle\hat{J}_z(\theta)\rangle^2 + \frac{1}{n}\partial_\theta\Delta^2\hat{J}_z(\theta)}{\Delta^2\hat{J}_z(\theta)},$$

and finally for large n

$$F(\theta) \approx n\frac{\partial_\theta\langle\hat{J}_z(\theta)\rangle^2}{\Delta^2\hat{J}_z(\theta)},$$

and therefore, we obtain

$$\Delta^2\theta = \frac{1}{n}\frac{\Delta^2\hat{J}_z(\theta)}{\left(\partial_\theta\langle\hat{J}_z(\theta)\rangle\right)^2}$$

which is formally the same as the error propagation formula from Equation 2.9.

Lastly, let us check how this formula compares to the fundamental bound given by the quantum Fisher information, which is derived in the next Section. Quantum

Fisher information was already defined in Section 2.8, and for the case of the Ramsey scheme (or the Mach-Zehnder interferometer) it reads

$$F_Q\left[\hat{\rho}, \hat{J}_y\right] = 4\Delta^2 \hat{J}_y$$

independent of the unknown parameter θ. For a coherent state polarised along the z axis, so the eigenstate of $\hat{J}_z$ operator, the quantum Fisher information is equal to N. The formula from Equation 3.4 seemingly depends on the unknown parameter θ, but if we perform a similar derivation as in Section 1.6, for coherent spin states, we obtain $\frac{1}{n \cdot N}$ which coincides with the value of the quantum Fisher information. At least for the case of coherent states the simple error propagation formula is the most efficient way to estimate the value of an unknown parameter. Equation 3.4 is commonly used in the literature to asses the phase sensitivity of an interferometer for various input states [22, 26, 28, 119, 216, 230–233].

3.5 Quantum Fisher information

The quantum Cramér-Rao bound is obtained by optimising the Fisher information over all possible measurements

$$F_Q\left[\hat{\rho}(\theta)\right] \equiv \max_{\{\hat{M}(\mathbf{m})\}} F\left[\hat{\rho}(\theta), \{\hat{M}(\mathbf{m})\}\right].$$

Quantum Fisher information was already defined in Section 2.8 as

$$F_Q\left[\hat{\rho}, \hat{J}_{\hat{n}}\right] = 4\Delta^2 \hat{R},$$

where the hermitian operator $\hat{R}$ is the solution of the equation

$$\{\hat{R}, \hat{\rho}\} = i\left[\hat{J}_{\hat{n}}, \hat{\rho}\right].$$

More generally, for transformations different than $\hat{J}_{\hat{n}}$, we will show that [2]

$$F_Q\left[\hat{\rho}(\theta)\right] = \mathrm{Tr}\left[\hat{\rho}(\theta)\hat{L}_\theta^2\right],$$

where the hermitian operator $\hat{L}_\theta$, called symmetric logarithmic derivative [223], is defined as the solution of the following Equation

$$\partial_\theta \hat{\rho}(\theta) = \frac{\hat{\rho}(\theta)\hat{L}_\theta + \hat{L}_\theta \hat{\rho}(\theta)}{2},$$

equivalent to Equation 3.5.

In order to derive quantum Fisher information, we will manipulate its classical counterpart

$$\begin{aligned} F(\theta) &= \sum_{\mathbf{m}} \frac{1}{P(\mathbf{m}|\theta)} \left(\partial_\theta P(\mathbf{m}|\theta)\right)^2 \\ &= \sum_{\mathbf{m}} \frac{\mathrm{Tr}\left[\hat{M}(\mathbf{m})\partial_\theta \hat{\rho}(\theta)\right]^2}{\mathrm{Tr}\left[\hat{M}(\mathbf{m})\hat{\rho}(\theta)\right]}. \end{aligned}$$

Using the definition of the symmetric logarithmic derivative (Equation 3.5), we rewrite the nominator as

$$\mathrm{Tr}\left[\hat{M}(\mathbf{m})\partial_\theta\hat{\rho}(\theta)\right] = \Re\left[\mathrm{Tr}\left[\hat{\rho}(\theta)\hat{L}_\theta\hat{M}(\mathbf{m})\right]\right],$$

where $\Re[\bullet]$ denotes the real part of an expression. For any number ξ we have

$$|\xi|^2 = \Re[\xi]^2 + \Im[\xi]^2,$$

where $\Im[\bullet]$ denotes the imaginary part of an expression, and therefore

$$\Re[\xi]^2 = |\xi|^2 - \Im[\xi]^2 \leq |\xi|^2,$$

and thus

$$\Re\left[\mathrm{Tr}\left[\hat{\rho}(\theta)\hat{L}_\theta\hat{M}(\mathbf{m})\right]\right]^2 \leq \left|\mathrm{Tr}\left[\hat{\rho}(\theta)\hat{L}_\theta\hat{M}(\mathbf{m})\right]\right|^2,$$

which is saturated when

$$\Im\left[\mathrm{Tr}\left[\hat{\rho}(\theta)\hat{L}_\theta\hat{M}(\mathbf{m})\right]\right]^2 = 0$$

The next step is to make use of the Cauchy-Schwarz inequality, that for two operators $\hat{A}$ and $\hat{B}$ reads

$$\left|\mathrm{Tr}\left[\hat{A}^\dagger\hat{B}\right]\right|^2 \leq \mathrm{Tr}\left[\hat{A}^\dagger\hat{A}\right]\mathrm{Tr}\left[\hat{B}^\dagger\hat{B}\right],$$

which is saturated for $\hat{A} = \lambda\hat{B}$, where λ is a complex number. Now, we set

$$\hat{A} = \sqrt{\hat{\rho}(\theta)}\sqrt{\hat{M}(\mathbf{m})} \quad \text{and} \quad \hat{B} = \sqrt{\hat{\rho}(\theta)}\hat{L}_\theta\sqrt{\hat{M}(\mathbf{m})},$$

and obtain

$$\left|\mathrm{Tr}\left[\hat{\rho}(\theta)\hat{L}_\theta\hat{M}(\mathbf{m})\right]\right|^2 \leq \mathrm{Tr}\left[\hat{\rho}(\theta)\hat{M}(\mathbf{m})\right]\mathrm{Tr}\left[\hat{M}(\mathbf{m})\hat{L}_\theta\hat{\rho}(\theta)\hat{L}_\theta\right],$$

which is saturated if and only if

$$\hat{\rho}(\theta) = \left(\hat{I} - \lambda_\theta\hat{L}_\theta\right)\hat{M}(\mathbf{m}) = 0,$$

with

$$\lambda_\theta = \frac{\left(\mathrm{Tr}\left[\hat{M}(\mathbf{m})\partial_\theta\hat{\rho}(\theta)\right]\right)^2}{\mathrm{Tr}\left[\hat{\rho}(\theta)\hat{M}(\mathbf{m})\right]}.$$

Therefore we can bound Equation 3.5 from above in the following way

$$\begin{aligned} F(\theta) &= \sum_{\mathbf{m}} \frac{\mathrm{Tr}\left[\hat{M}(\mathbf{m})\partial_\theta\hat{\rho}(\theta)\right]^2}{\mathrm{Tr}\left[\hat{M}(\mathbf{m})\hat{\rho}(\theta)\right]} \\ &\leq \sum_{\mathbf{m}} \mathrm{Tr}\left[\hat{M}(\mathbf{m})\hat{L}_\theta\hat{\rho}(\theta)\hat{L}_\theta\right], \end{aligned}$$

which after evaluating the sum, $\sum_{\mathbf{m}} \hat{M}(\mathbf{m}) = \hat{I}$, becomes

$$F(\theta) \leq \mathrm{Tr}\left[\hat{\rho}(\theta)\hat{L}_\theta^2\right] \equiv F_Q\left[\hat{\rho}(\theta)\right].$$

Equation 3.5 is satisfied by choosing a positive-operator valued measure made of projectors $\{|\gamma_l\rangle\langle\gamma_l|\}$ into the basis that diagonalises symmetric logarithmic derivative $\hat{L}_\theta|\gamma_l\rangle = \gamma_l|\gamma_l\rangle$ and taking $\lambda_\theta = 1/\gamma_l$ [2]. With such a choice, Equation 3.5 is also saturated since

$$\Im\left[\mathrm{Tr}\left[\hat{\rho}(\theta)\hat{L}_\theta|\gamma_l\rangle\langle\gamma_l|\right]\right] = \Im\left[\gamma_l\langle\gamma_l|\hat{\rho}(\theta)|\gamma_l\rangle\right] = 0.$$

In conclusion, there exists at least one optimal measurement. This Hermitian observable is build out of the orthonormal eigenstates of a symmetric logarithmic derivative. We should also stress that when estimating an unknown parameter one usually assumes that it only labels the available states of the system and does not influence the outcomes of the measurement used to extract the information about the parameter itself. This is a necessary assumption for the derivation of the quantum Cramér-Rao bound and the quantum Fisher information as an upper limit to the Fisher information. However, there exist estimation problems where this assumption is not satisfied. For more details see Reference [234] and [235].

Now, we calculate the quantum Fisher information explicitly in terms of complete basis $\{|k\rangle\}$ such that

$$\hat{\rho}(\theta) = \sum_k p_k|k\rangle\langle k| \quad \text{with} \quad p_k \geq 0 \quad \text{and} \quad \sum_k p_k = 1.$$

The first step is the rewrite Equation 3.5 by performing the trace in the basis of $\{|k'\rangle\}$ and by using its invariance under cyclic permutations

$$\begin{aligned} F_Q\left[\hat{\rho}(\theta)\right] &= \mathrm{Tr}\left[\hat{\rho}(\theta)\hat{L}_\theta^2\right] = \mathrm{Tr}\left[L_\theta\hat{\rho}(\theta)\hat{L}_\theta\right] \\ &= \sum_{k'}\langle k'|\hat{L}_\theta\sum_k p_k|k\rangle\langle k|\hat{L}_\theta|k'\rangle \\ &= \sum_{k,k'} p_k\left|\langle k|\hat{L}_\theta|k'\rangle\right|^2 \\ &= \sum_{k,k'}\frac{p_k+p_k'}{2}\left|\langle k|\hat{L}_\theta|k'\rangle\right|^2, \end{aligned}$$

where the last step is simply twice the sum divided by 2, written for convenience. In order to calculate the quantum Fisher information, one needs to know the matrix elements $\langle k|\hat{L}_\theta|k'\rangle$ for $p_k + p_k'$ different than 0. This can be obtained from the definition of symmetric logarithmic derivative from Equation 3.5

$$\langle k|\hat{L}_\theta|k'\rangle = \frac{2}{p_k+p_k'}\langle k|\partial_\theta\hat{\rho}(\theta)|k'\rangle, \quad \text{with} \quad p_k + p_k' \neq 0$$

therefore, we have

$$F_Q\left[\hat{\rho}(\theta)\right] = \sum_{k,k'}\frac{2}{p_k+p_k'}\left|\langle k|\partial_\theta\hat{\rho}(\theta)|k'\rangle\right|^2.$$

The next step is to calculate the derivative of the density matrix

$$\partial_\theta \hat{\rho}(\theta) = \sum_k (\partial_\theta p_k) \left|k\right\rangle \left\langle k\right| + \sum_k p_k \left|\partial_\theta k\right\rangle \left\langle k\right| + \sum_k p_k \left|k\right\rangle \left\langle \partial_\theta k\right| .$$

Calculating its matrix elements yields

$$\begin{aligned}\left\langle m|\partial_\theta \hat{\rho}(\theta)|n\right\rangle &= \sum_k \left\langle m\right| (\partial_\theta p_k) \left|k\right\rangle \left\langle k|n\right\rangle + \left\langle m\right| \sum_k p_k \left|\partial_\theta k\right\rangle \left\langle k|n\right\rangle + \sum_k p_k \left\langle m|k\right\rangle \left\langle \partial_\theta k|n\right\rangle \\ &= \partial_\theta p_m \delta_{m,n} + p_n \left\langle m|\partial_\theta n\right\rangle + p_m \left\langle \partial_\theta m|n\right\rangle ,\end{aligned}$$

which after using the following identity

$$\partial_\theta \left\langle m|n\right\rangle = \left\langle \partial_\theta m|n\right\rangle + \left\langle m|\partial_\theta n\right\rangle = 0$$

becomes

$$\left\langle m|\partial_\theta \hat{\rho}(\theta)|n\right\rangle = \partial_\theta p_m \delta_{m,n} + p_m \left\langle \partial_\theta m|n\right\rangle - p_n \left\langle \partial_\theta m|n\right\rangle .$$

Now if we plug it into Equation 3.5, we get

$$\begin{aligned}F_Q\left[\hat{\rho}(\theta)\right] &= \sum_{k,k'} \frac{2}{p_k + p'_k} \left|\partial_\theta p_k \delta_{k,k'} + (p_k - p'_k) \left\langle \partial_\theta k|k'\right\rangle \right|^2 \\ &= \sum_k \frac{(\partial_\theta p_k)^2}{p_k} + 2 \sum_{k,k'} \frac{(p_k - p'_k)^2}{(p_k + p'_k)} \left| \left\langle \partial_\theta k|k'\right\rangle \right|^2 \\ &.\end{aligned}$$

For pure states $\left|\psi(\theta)\right\rangle$, we have $\hat{\rho}(\theta) = \hat{\rho}^2(\theta)$, and therefore, we can write

$$\partial_\theta \hat{\rho}(\theta) = \partial_\theta \hat{\rho}^2(\theta) = (\partial_\theta \hat{\rho}(\theta))\, \hat{\rho}(\theta) + \hat{\rho}(\theta)\, (\partial_\theta \hat{\rho}(\theta)) ,$$

and identify the symmetric logarithmic derivative as $\hat{L}_\theta = 2\partial_\theta \hat{\rho}(\theta)$, (see Equation 3.5). Now, we can calculate the quantum Fisher information directly by inserting the above expression to quantum Fisher information formula from Equation 3.5

$$\begin{aligned}F_Q\left[\hat{\rho}(\theta)\right] &= \mathrm{Tr}\left[\hat{\rho}(\theta)\, (2\partial_\theta \hat{\rho}(\theta))^2\right] \\ &= \mathrm{Tr}\left[\left|\psi(\theta)\right\rangle \left\langle \psi(\theta)\right| (2\partial_\theta \left|\psi(\theta)\right\rangle \left\langle \psi(\theta)\right|)^2\right] \\ &= \left\langle \psi(\theta)\right| (2\partial_\theta \left|\psi(\theta)\right\rangle \left\langle \psi(\theta)\right|)^2 \left|\psi(\theta)\right\rangle \\ &= 4\left(\left\langle \partial_\theta \psi(\theta)|\partial_\theta \psi(\theta)\right\rangle + \left\langle \psi(\theta)|\partial_\theta \psi(\theta)\right\rangle^2 + \left\langle \partial_\theta \psi(\theta)|\psi(\theta)\right\rangle^2 + \left| \left\langle \partial_\theta \psi(\theta)|\psi(\theta)\right\rangle \right|^2\right) ,\end{aligned}$$

which after using $\left\langle \psi(\theta)|\partial_\theta \psi(\theta)\right\rangle = -\left\langle \partial_\theta \psi(\theta)|\psi(\theta)\right\rangle$ becomes simply

$$F_Q\left[\left|\psi(\theta)\right\rangle\right] = 4\left(\left\langle \partial_\theta \psi(\theta)|\partial_\theta \psi(\theta)\right\rangle - \left| \left\langle \partial_\theta \psi(\theta)|\psi(\theta)\right\rangle \right|^2\right) .$$

Finally, let us calculate the quantum Fisher information for unitary transformations

$$\hat{\rho}(\theta) = e^{-i\theta \hat{H}} \hat{\rho} e^{i\theta \hat{H}},$$

where $\hat{H}$ is some hermitian operator which usually describes the type on an interferometer. An important feature of unitary transformations is that they do not change the eigenvalues

$$\hat{\rho}(\theta) = \sum_k p_k e^{-i\theta\hat{H}} |k\rangle \langle k| e^{i\theta\hat{H}},$$

therefore Equation 3.5 becomes

$$F_Q[\hat{\rho}(\theta)] = 2\sum_{k,k'} \frac{(p_k - p'_k)^2}{(p_k + p'_k)} |\langle \partial_\theta k|k'\rangle|^2,$$

where the derivative can be easily evaluated to give

$$F_Q[\hat{\rho}(\theta)] = 2\sum_{k,k'} \frac{(p_k - p'_k)^2}{(p_k + p'_k)} |\langle k|\hat{H}|k'\rangle|^2,$$

which for pure states reduces to (see Equation 3.5)

$$F_Q[\psi(\theta)] = 4\left(\langle\psi|\hat{H}^2|\psi\rangle - \langle\psi|\hat{H}|\psi\rangle^2\right) = 4\Delta^2\hat{H},$$

a result independent of θ since $e^{\pm i\theta\hat{H}}$ commutes with $\hat{H}$ and calculated for the initial state.

But is the quantum Fisher information for pure states always independent of θ for a unitary transformation? In order to answer this question let us consider a transformation governed by the following Hamiltonian

$$\hat{H} = \theta\hat{H}_1 + \hat{H}_2,$$

where $\hat{H}_1$ and $\hat{H}_2$ are independent of θ. Now, we calculate the derivative of $|\psi(\theta)\rangle = e^{-i\theta\hat{H}_1+\hat{H}_2}|\psi\rangle$ with respect to θ. In order to calculate this derivative, we first expand the exponent by using the Zassenhaus formula, which states that for two operators $\hat{A}$ and $\hat{B}$, we have

$$e^{\hat{A}+\hat{B}} = e^{\hat{A}}e^{\hat{B}}e^{-\frac{1}{2}\left[\hat{A},\hat{B}\right]}e^{\frac{1}{6}\left(2\left[\hat{B},\left[\hat{A},\hat{B}\right]\right]+\left[\hat{A},\left[\hat{A},\hat{B}\right]\right]\right)}\ldots,$$

where the exponents of higher order in are likewise nested commutators. Apart from a situation where $\hat{B} = 0$ or $\left[\hat{A},\hat{B}\right] = 0$ the quantum Fisher information depends on θ and is evaluated in the initial state. For this reason, it is convenient to introduce the so-called generator of an infinitesimal change $\hat{h}$ with respect to the unknown parameter θ which is defined as

$$\hat{h}|\psi(\theta)\rangle = i\partial_\theta|\psi(\theta)\rangle,$$

therefore for unitary evolution $|\psi(\theta)\rangle = \hat{U}(\theta)|\psi\rangle$ the generator of the infinitesimal change can be calculated according to

$$\hat{h} = i\left(\partial_\theta\hat{U}(\theta)\right)\hat{U}^\dagger(\theta),$$

leading to the following expression for quantum Fisher information

$$F_Q[\psi(\theta)] = 4\left(\langle\psi(\theta)|\hat{h}^2|\psi(\theta)\rangle - \langle\psi(\theta)|\hat{h}|\psi(\theta)\rangle^2\right) = 4\Delta^2\hat{h},$$

where $\hat{h}$ can be calculated analytically, for instance, when the Zassenhaus expansion of the Hamiltonian is finite.

To conclude, we know that $F_Q\left[\hat{\rho}(\theta)\right] \leq 4\Delta^2\hat{h}$, which is saturated for pure states. Alternatively, we can derive this inequality in the following way

$$\begin{aligned} F_Q\left[\hat{\rho}(\theta)\right] &= 2\sum_{k,k'}\frac{(p_k-p'_k)^2}{(p_k+p'_k)}\left|\left\langle k|\hat{h}|k'\right\rangle\right|^2 \leq 2\sum_{k,k'}\frac{(p_k+p'_k)^2}{(p_k+p'_k)}\left|\left\langle k|\hat{h}|k'\right\rangle\right|^2 \\ &= 2\sum_{k,k'}(p_k+p'_k)\left|\left\langle k|\hat{h}|k'\right\rangle\right|^2 = 4\sum_{k,k'}p_k\left|\left\langle k|\hat{h}|k'\right\rangle\right|^2 = 4\Delta^2\hat{h}, \end{aligned}$$

where the equality holds only for pure states. Summarising, for a unitary evolution, we have

$$F(\theta) \leq F_Q\left[\hat{\rho}(\theta),\hat{h}\right] \leq 4\Delta^2\hat{h}.$$

Let us now consider an interesting situation where we can find the optimal state in terms of the highest quantum Fisher information. For pure states, we can find the optimal state by noticing that any linear rotation can be expressed as $\hat{J}_{\hat{n}} = \hat{n}\cdot\hat{\mathbf{J}}$ and therefore rewriting the variance as 3×3 covariance matrix

$$\Delta\hat{J}^2_{\hat{n}} = \hat{n}^T\left\langle\left(\hat{\mathbf{J}}-\left\langle\hat{\mathbf{J}}\right\rangle\right)\left(\hat{\mathbf{J}}-\left\langle\hat{\mathbf{J}}\right\rangle\right)\right\rangle\hat{n},$$

where the T superscript stands for the transposition. Now, we can express the quantum Fisher information in the following way

$$F_Q\left[\psi,\hat{J}_{\hat{n}}\right] = 4\hat{n}^T\gamma_C\hat{n},$$

where γ_C is a real matrix defined as

$$\left[\gamma_C\right]_{i,j} = \frac{\left\langle\hat{J}_i\hat{J}_j\right\rangle+\left\langle\hat{J}_j\hat{J}_i\right\rangle}{2} - \left\langle\hat{J}_i\right\rangle\left\langle\hat{J}_j\right\rangle.$$

This expression can be maximised by choosing $\hat{n} = \hat{n}_{\max}$ as the eigenvector corresponding to the maximal eigenvalue $\lambda_{\max}$ of the γ_C matrix. Therefore, the maximal quantum Fisher information is given

$$F_Q\left[\psi,\hat{J}_{\hat{n}_{\max}}\right] = 4\lambda_{\max},$$

with optimal direction given be $\hat{n}_{\max}$. The maximal value $\lambda_{\max}$ is constructed from the minimum and maximum eigenvalue states of $\hat{J}_{\hat{n}}$ operator

$$\lambda_{\max} = \frac{1}{4}\left(\epsilon_{\max}-\epsilon_{\max}\right)^2,$$

where $\epsilon_{\max}$ and $\epsilon_{\min}$ are the maximum and minimum eigenvalues of $\hat{J}_{\hat{n}}$ operator, respectively. For instance, for $\hat{J}_y$, so the Mach-Zehnder interferometer, the optimal state, which is the superposition of maximum and minimum eigenstates, gives quantum Fisher information equal to N^2, so the Heisenberg limit.

Finally, we can ask whether it is possible to have quantum Fisher information higher than N^2 or what is the condition for overcoming the Heisenberg limit. Let us consider a non-linear interferometer, for instance, we can treat the one-axis twisting Hamiltonian as an interferometer and try to estimate the interaction strength. This

operation is expressed by

$$\hat{U}(\theta) = e^{-i\theta \hat{J}_z^2},$$

where the interaction strength θ plays now the role of the phase that we want to estimate with the highest possible precision. According to Equation 3.5, it is straightforward to calculate the generator of the infinitesimal change $\hat{h}$ which in this case is simply $\hat{J}_z^2$, and therefore, the quantum Fisher information can scale as N^4. Note, however, that even though quantum Fisher information is higher than N^2, it does not mean that the Heisenberg limit was overcome. This is because we have used a nonlinear phase imprint which changes the definition of the Heisenberg limit exactly to N^4.

In a general case, for an interferometer described by $\hat{J}_{\hat{n}}^p$, the quantum Fisher information dependence on the number of system constituents scales like N^{2p}. A detailed analysis of scaling with N can be found in Reference [236].

Part II

Conducted Research

Chapter 4

Quantum-Enhanced Interferometry and the Structure of Twisted States

The notion of twisted states was already introduced in Section 2.6. The one-axis twisting Hamiltonian was proposed for squeezing the coherent spin states and thus creating spin squeezing, for instance, in an ensemble of atoms. As a matter of fact, spin-squeezed states created by one-axis twisting are only a small fraction of a large family of entangled states that can be generated with this method. One of the most peculiar states that belong to the family of twisted states is the atomic Schrödinger's cat state, which is a macroscopic superposition of two spin-coherent states that are located on the antipodes of the generalised Bloch sphere.

Twisted states are promising candidates for performing quantum enhanced measurements. The reason for this is their complex structure which changes significantly when a state is being rotated allowing for high distinguishability from neighbouring states. This Chapter is based on Reference [213].

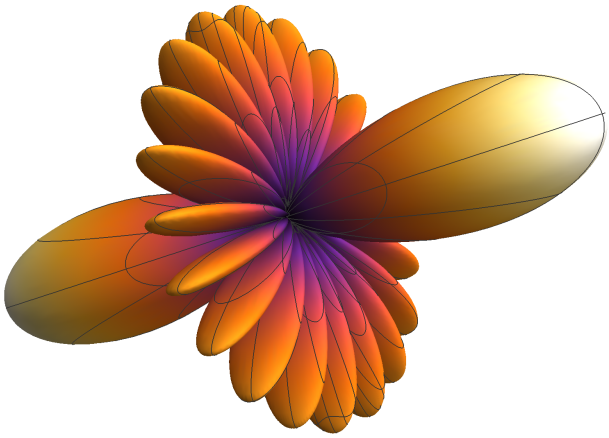

FIGURE 4.1: SU(2) Wigner function of a maximally entangled twisted state, *i.e.*, the atomic Schrödinger's cat state.

Contents

4.1 Twisted states

Some details about twisted states were already introduced in Section 2.6. Nevertheless, for clarity, let us recall some of them again. The family of twisted states constitutes of coherent spin states twisted along the axis perpendicular to the axis of the main spin. Therefore, the one-axis twisting Hamiltonian

$$\hat{H}_{\mathrm{OAT}} = \xi \hat{J}_z^2,$$

can generate twisted states out of the coherent-spin states polarised along x or y axis. In principle, any spin-coherent state can be squeezed by the one-axis twisting Hamiltonian since almost any spin-coherent state has non zero x or y component. The only exception is the states that are the eigenstates of the one-axis twisting Hamiltonian, so the spin-coherent states polarised along the z axis. More generally, the one-axis twisting Hamiltonian can be defined as

$$\hat{H}_{\mathrm{OAT}} = \xi \hat{J}_{\hat{n}}^2,$$

so the square of the abstract momentum vector in the direction given by $\hat{n}$.

For brevity, we focus on the twisted states of the following form ($j = N/2$)

$$|\psi(\mu)\rangle = \sum_{m=-j}^{j} c_m e^{-i\mu m^2} |j, m\rangle ,$$

where c_m's are that of the $|\pi/2, 0\rangle$ state (see Section 2.7). As we have already seen, these states exhibit entanglement and spin-squeezing for $\mu < 2 \cdot 24^{1/6} \left(\frac{N}{2}\right)^{-2/3}$ [174]. Nevertheless, after this time the state remains entangled but not spin squeezed reaching the maximally entangled state at $\mu = \pi/2$ as depicted in Figures 4.2 and 4.3.

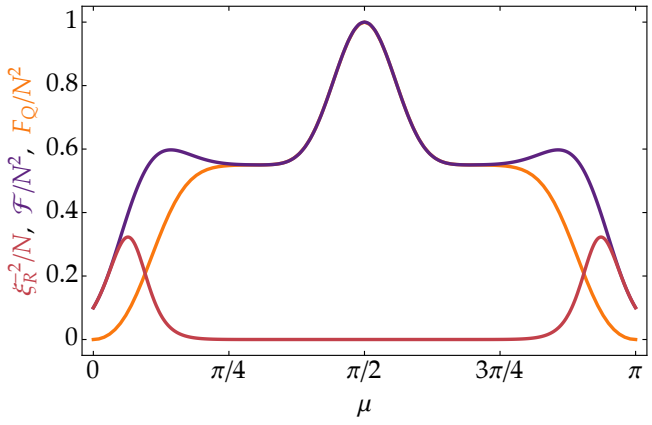

FIGURE 4.2: The spin-squeezing parameter ξ_R^{-2}, quantum Fisher information with respect to x direction $F_Q\left[\hat{\rho}, \hat{J}_{\hat{x}}\right]$, and the dynamical susceptibility $\mathcal{F}\left[\hat{\rho}\right]$ for the state from Equation 2.7 with initial condition $|\pi/2, 0\rangle$ normalised to 1 as a function of μ. The squeezing parameter is able initially to sense the correlations with the state, but its not able to grasp the correlations in the maximally entangled state for $\mu = \pi/2$. Here $N = 10$.

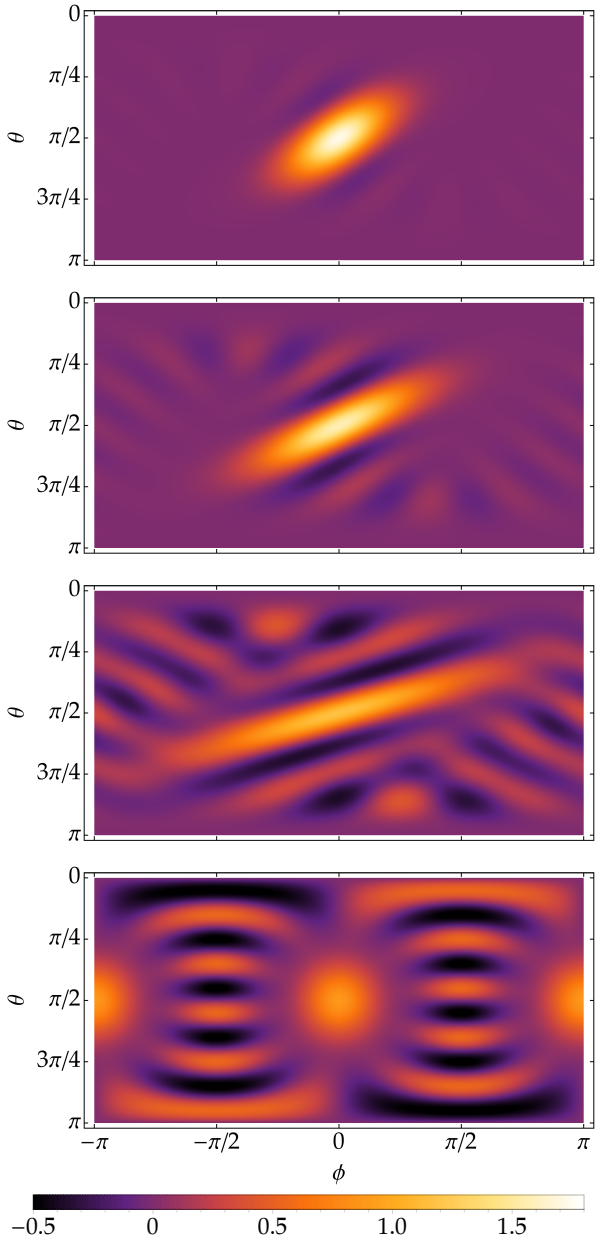

FIGURE 4.3: The evolution of SU(2) Wigner function of the coherent spin state $|\pi/2, 0\rangle$ under the action of one-axis twisting Hamiltonian for $N = 10$ atoms. This is the extension of Figure 2.9 from Section 2.7. The panel depicts a twisted coherent spin state for four different values of μ. In the top panel, we see a moderately squeezed state for $\mu = 0.1$. The second panel shows almost optimally squeezed state $\mu = 0.2$. The third panel shows a state that is no longer squeezed $\mu = 0.4$. Finally, the bottom panel shows the maximally entangled atomic cat state which is not spin squeezed. All these states are particle entangled. The animation presenting the evolution of the SU(2) Wigner function can be found in Reference [237]

4.2 Fine structures

What is so special about the twisted states is their complicated structure. The examples of the fine structures of these states can be seen in Figure 4.1 and 4.3. In particular, the atomic Schrödinger's cat state can serve to explain how the fine structures of this state contribute to enhanced phase sensitivity. We want to make a small rotation after which the final state is maximally distinguishable from the initial state. This results in a minimal overlap between the initial and the final state. Therefore, we should rotate the atomic Schrödinger's cat state about the axis perpendicular to the plane in which the fine structures are located. On the other hand, if we rotated the Wigner function about the axis parallel to the fine structures, the rotation would not see the fine structures, and it would be as if we rotated a coherent spin state; therefore it would not be possible to beat the shot-noise limit. The number of fine structures increases with N, and thus the Schrödinger's cat state gets more susceptible to changes with increasing number of atoms. Unfortunately, the fine structures are also very fragile, so decoherence and the incomplete knowledge of the initial state prevent from reaping the benefits of Schrödinger's cat state's fine structures. The reason why fine structures increase the distinguishability of states is given in detail in Reference [238] and also in Reference [213] which this Chapter is based on.

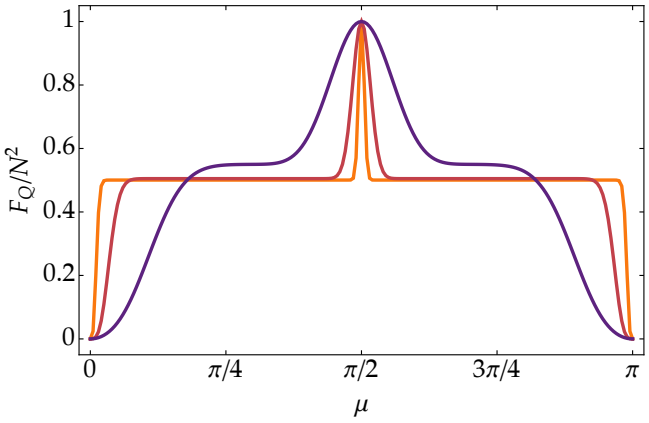

FIGURE 4.4: Quantum Fisher information as a function of number of atoms N. The purple, red, and orange lines correspond to 10, 100, and 1000 atoms respectively.

Interestingly, we do not need to wait for the creation of the Schrödinger's cat state. It turns out that a large set of twisted states are already sufficiently entangled to give scaling proportional to the Heisenberg scaling $1/N^2$. This can be seen in Figure 4.4 where quantum Fisher information is plotted as a function of the number of particles. The characteristic plateau extends its range with increasing N meaning that for large atom number $N \gg 1$ the creation of entanglement is almost instantaneous. From the perspective of a real system which takes into account decoherence and imperfect knowledge of the state, this is extremely beneficial. The entangled states from the plateau are not that fragile as the maximally entangled state against decoherence and can be potentially used to estimate an unknown parameter with very high precision, roughly two times worse than the maximal precision.

In order to understand why quantum Fisher information stays constant for the majority of twisted states (especially for $N \gg 1$), let us consider two experimentally attainable transformations, namely rotations of the generalised Bloch sphere around

x and y axes. If $\mu \gtrsim \sqrt{N}$, the phase of each term from Equation 4.1 changes quickly effectively yielding

$$F_Q = 4\Delta^2 \hat{J}_{x/y} \simeq 2 \left[\sum_{m=-j}^{j} c_m^2 \beta_m^2 \pm \sum_{m=-j}^{j} c_m c_{m+2} \beta_m \beta_{m+1} e^{4i\mu m} \right],$$

where $\beta_m = \sqrt{(N/2+m+1)(N/2-m)}$ which for large N can be approximated by $N/2$. Furthermore, when μ does not lie in the vicinity of $\pi/2$, the fast changes of the phase vanish the second sum from Equation 4.2 yielding $F_Q = N^2/2$ for both transformations. Only if μ is approximately equal to $\pi/2$ the phase factor is $\sim e^{i2\pi m} = 1$ and thus the second sum has a significant contribution. Figure 4.4 shows only the rotation around the x-axis which amounts to positive contribution; for the rotation around the y-axis the contribution is negative and therefore Fisher information is equal to 0.

Now we can show that the estimation of the unknown parameter θ from the population imbalance measurement exploits the entanglement presented in twisted states. To this end, we need the Fisher information

$$F(\theta) = \sum_{m=-j}^{j} \frac{1}{p(m|\theta)} \left(\partial_\theta p(m|\theta)\right)^2,$$

with $p(m|\theta)$ being the projection of the output state onto a Dicke state $|m\rangle$

$$p(m|\theta) = |\, \langle m|e^{-i\theta \hat{J}_{x/y}}|\psi(\mu)\rangle \,|^2.$$

For the rotation around x-axis, we get

$$F(\theta) = \sum_{m=-j}^{j} \left(\beta_m \sin(\tilde{\phi}_{m+1} - \tilde{\phi}_m)|\tilde{c}_{m+1}| - \beta_{m-1} \sin(\tilde{\phi}_m - \tilde{\phi}_{m-1})|\tilde{c}_{m-1}|\right)^2,$$

where $\tilde{c}_m = \langle m|e^{-i\theta \hat{J}_x}|\psi(\mu)\rangle$ and $\tilde{\phi}$ is the phase of $\tilde{c}_m$. On the plateau, where the phase changes quickly, the cross-term contribution to the Fisher information is negligible. Moreover, if we average the squared sine functions with theirs average value $1/2$, we get

$$F(\theta) \simeq \sum_{m=-j}^{j} \beta_m^2 |\tilde{c}_m|^2,$$

which resembles the first term from Equation 4.2. For a special case when θ is approximately 0 and $\tilde{c}_m$'s are distributed around $m = 0$, β_m^2 can be approximated with $N^2/4$ yielding

$$F \simeq \frac{N^2}{4} \sum_{m=-j}^{j} |\tilde{c}_m| = \frac{N^2}{4},$$

a result independent on θ. Note that for the rotation around the y axis the sine functions are replaced by cosine functions and thus giving the same Fisher information as above in Equation 4.2. This proves that the estimation from the population imbalance benefits from the entanglement present in twisted states and allows for Heisenberg limited sensitivity for a wide range of μ.

These results, however, are obtained for an ideal case, in the absence of detection errors and noise. Now we address the influence of these limitations by focusing on two deleterious sources limiting the performance of an interferometer exploiting twisted states. The first one arises from the inability to fully control the two-body interactions caused, for instance, by fluctuating magnetic field [239–241] or imprecise control over the twisting time. To account for this, we assume that the resulting state is an incoherent mixture of twisted states peaked around μ with uncertainty $\delta\mu$:

$$\hat{\rho}_\mu = \int \mathrm{d}\tilde{\mu}\, P(\tilde{\mu}-\mu)\, |\psi_{\tilde{\mu}}\rangle \langle\psi_{\tilde{\mu}}|\,,$$

where $P(\tilde{\mu}-\mu) \propto \exp\left[-\tilde{\mu}^2/2(\delta\mu)^2\right]$. With this state, the probability of measuring $|m\rangle$ is

$$p(m|\theta) = \mathrm{Tr}\left[|m\rangle\langle m|\, e^{-i\theta\hat{J}_{x/y}}\hat{\rho}_\mu e^{i\theta\hat{J}_{x/y}}\right].$$

If we assume now that $\delta\mu \lesssim 1$, the Fisher information becomes

$$F = \frac{N^2}{4}\frac{1}{\sqrt{1+2N(\delta\mu)^2}}.$$

Now, if one can precisely control μ so that $\delta\mu \lesssim 1/\sqrt{N}$, the Heisenberg scaling is retained. Even when the control over μ is not that precise so that $\delta\mu \gtrsim 1/\sqrt{N}$, the Fisher information is proportional to $N^{3/2}$, and sub-shot-noise interferometry is still possible.

Another factor limiting the sensitivity are atom detectors with finite resolution σ [242, 243]. As a consequence, the probability from Equation 4.2 has to be modified to account for σ:

$$\tilde{p}(m|\theta) = \sum_{m'=-j}^{j} R(m-m')p(m'|\theta),$$

where $R(m) \propto \exp\left[-m^2/2\sigma^2\right]$ is the Gaussian resolution function. The limited resolution of atom detectors are more deleterious than imprecise knowledge of μ since it smooths the fine structures in the probability. The numerical calculations show that the Fisher information has a universal behaviour:

$$F(\sigma) \propto \frac{N^2}{4}\frac{1}{\sigma^2},$$

which indicates the minimal required resolution of detectors allowing for beating the shot-noise limit, $\sigma \lesssim \sqrt{N}$.

These results show a general feature of entangled states. From the viewpoint of metrology, such states are highly susceptible to transformations that imprint a phase shift [244]. Subsequently, this susceptibility transfers to the distance between neighbouring probabilities $p(m|\theta)$ and $p(m|\theta+\delta\theta)$. In other words, the fine structures of a quantum state (see Figure 4.1) translate to fine structures in the probability. Finally, let us have a look at an experiment in which twisted states were generated and manipulated to reveal their quantumness by measuring the Fisher information.

4.3 Fisher information and entanglement of non-Gaussian spin states

The generation of entangled twisted states was reported by Helmut Strobel *et al.* in Reference [57]. Their experimental setup consisted of interacting Bose-Einstein condensates of Rubidium with linearly coupled two internal states (Figure 4.5, A and B). The linear coupling allowed for the control of the initial state and manipulation of the final state before the measurement (Figure 4.5, B and D). The interaction led to the generation of spin-squeezed states and subsequently to the generation of states referred to as non-Gaussian by the authors (Figure 4.5B).

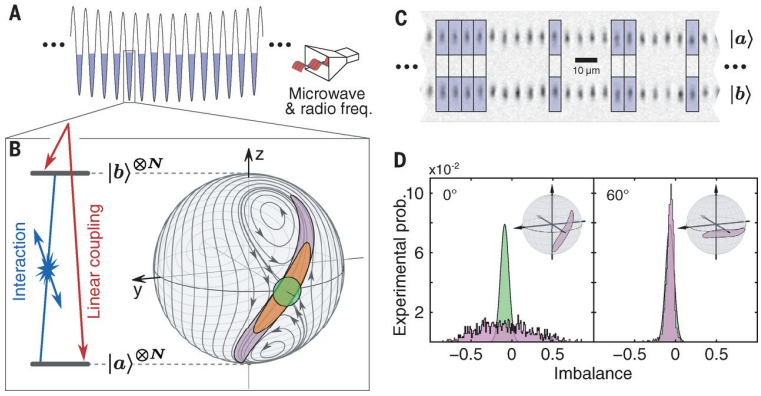

FIGURE 4.5: Figure from Reference [57]. Preparation and detection of twisted (non-Gaussian) states. (A) Bose-Einstein condensates in an optical lattice manipulated by microwave and radio frequency fields. (B) The interplay of nonlinear interaction (blue) and weak Rabi coupling (red) between the internal states $|a\rangle$ and $|b\rangle$ squeezes the initial coherent state (green) and subsequently creates non-Gaussian states. The state of the system is visualised on a generalised Bloch sphere with radius $J = N/2$, with N being the number of atoms. Edges of shaded areas are contours of the Husimi distribution for $N = 380$ atoms (C) Experimental absorption pictures. Shaded boxes indicate the sites which were selected for the analysis. (D) An exemplary histogram of the imbalance $z = 2\langle \hat{J}_z \rangle / N$ before and after rotation. Green Gaussian is the histogram for the ideal coherent spin state.

The characterisation of twisted states relied on destructive detection of the populations of the atomic states $|a\rangle = |F = 1, m_F = 1\rangle$ and $|b\rangle = |F = 2, m_F = -1\rangle$ for each condensate (Figure 4.5C). The probability distributions of the imbalance $z = (N_b - N_a)/N$ (the average value of $\hat{J}_z$ operator) were measured along defined directions by making an appropriate spin rotation before detection and by repeating the experiment many thousand times. The reconstruction of the density matrix confirmed initial squeezing and subsequent twisting of the initial state (see also Figure 4.3).

Further analysis of the variance of z revealed the minimum of squeezing $\xi_R^2 = -4.5 \pm 0.2$ dB below the standard quantum limit. Eventually, the twisting dynamics led to increased fluctuations in all directions, and after 25 ms the spin squeezing vanished.

The extraction of the Fisher information from the system was carried out using the Hellinger distance, defined as

$$d_{\mathrm{H}}^2(\theta) = \sum_z \left[\sqrt{P_z(\theta)} - \sqrt{P_z(0)}\right]^2$$

where $P_z(\theta)$ is the experimental probability distribution of z at angle θ. The Fisher information was extracted by expanding the Hellinger distance in Taylor series in the following way

$$d_{\mathrm{H}}^2(\theta) = \frac{F}{8}\theta^2 + \mathcal{O}(\theta^3),$$

which reveals a connection between Hellinger distance and Fisher information. The analysis of the Fisher information revealed that entanglement was still present in the system, although squeezing already vanished. As expected, when the state was still squeezed, Fisher information and the inverse spin squeezing agreed, $F/N \approx 1/\xi_R^2$, because these states are fully characterised by their variance.

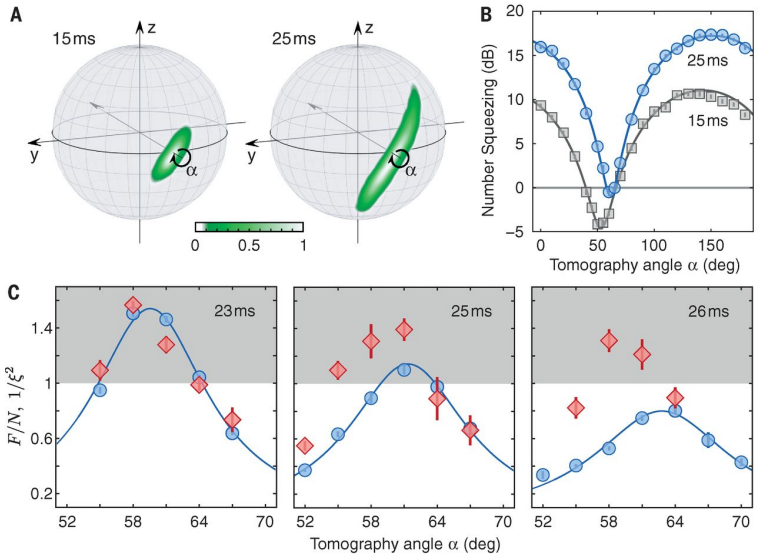

FIGURE 4.6: Figure from Reference [57]. Characterisation of entangled states. (A) Reconstruction of the Husimi function after evolution of 15 and 25 ms. (B) The analysis of the particle imbalance revealed maximum spin squeezing of $\xi_R^2 = -4.5 \pm 0.2$ dB for 15 ms and $\xi_R^2 = -0.2 \pm 0.3$ dB for 25 ms. (C) Comparison of the normalised Fisher information F/N (red squares) and the inverse of the spin squeezing parameter ξ_R^2 (blue circles). The grey shaded area is restricted for non-separable (entangled) states.

Chapter 5

Quantum-enhanced Interferometry with Cavity QED-generated Non-classical Light

Cavity quantum electrodynamics, usually shortened to cavity QED, is the study of the interaction between light confined in a reflective cavity and atoms or other particles, under conditions where the quantum nature of light is significant. One of the fathers of cavity quantum dynamics is Serge Haroche, who shares half of the Nobel prize in physics for developing the new field of physics where the interaction between an atom and radiation in an optical or microwave cavity is used to control the properties of the former.

In a series of experiments, Haroche used cavity quantum electrodynamics to realise Schrödinger's cat in which a macroscopic system is in a superposition of two different states. Such states are incredibly fragile, and the techniques developed to create and measure QED-states are now being applied, for instance, to the development of quantum computers. In this chapter, which is based on Reference [245], we focus on the exploitation of such states in phase estimation under realistic conditions.

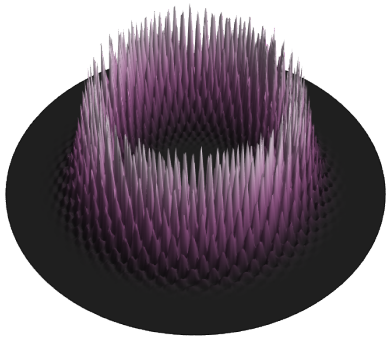

FIGURE 5.1: 3D Polar plot representing probability of measuring a certain number of photons for a Schrödinger's cat state.

Contents

5.1 The Jaynes-Cummings model

The Jaynes-Cummings model [246], or the Jaynes-Cummings Hamiltonian, was originally proposed in 1963 by Jaynes and Cummings to study the relationship between the quantum and the semi-classical theory in describing spontaneous emission. It describes a simple model (see Figure 5.2) comprised of a two-level atom consisting of the ground state $|g\rangle$ and the excited state $|e\rangle$ separated by energy $\hbar\omega_A$, where ω_A is the transition frequency, interacting with a single mode electromagnetic field with a frequency ω_C (see Chapter 1). This system is described by the following Hamiltonian

$$\hat{H} = \hat{H}_{\text{atom}} + \hat{H}_{\text{field}} + \hat{H}_{\text{int}},$$

where

$$\hat{H}_{\text{atom}} = \hbar\omega_A \hat{\sigma}_+ \hat{\sigma}_-,$$

describes the non-interacting two-level atom, where $\hat{\sigma}_+$ corresponds to exciting the atom and $\hat{\sigma}_-$ corresponds to the transition from the excited state to the ground state; they are also called raising and lowering operators of the atom. Note that in the previous Chapters, we were using a different notation, namely, instead of $\hat{\sigma}_+$ or $\hat{\sigma}_-$, we were using creation and annihilation operators corresponding to the ground state $\hat{g}$ and excited state $\hat{e}$. In this notation, $\hat{\sigma}_+$ corresponds to the $\hat{e}^\dagger \hat{g}$ which annihilates a particle in the ground states and creates a particle in the excited state. The second term

$$\hat{H}_{\text{field}} = \hbar\omega_A \hat{a}^\dagger \hat{a},$$

describes the longitudinal mode of the cavity, where operators $\hat{a}^\dagger$ and $\hat{a}$ are given by the decomposition of our single mode field

$$\hat{E} = \mathcal{E} \sin(kx) \left(\hat{a} + \hat{a}^\dagger\right) \quad \text{with} \quad \mathcal{E} = \sqrt{\frac{\hbar\omega_C}{2\epsilon_0 L}},$$

where ϵ_0 is the vacuum permittivity and L is the length of the cavity. The interaction energy in the dipole approximation, which assumes that the wavelength of the emitted photon is much larger than atomic dimension, is

$$\hat{H}_{\text{int}} = -\hat{d} \cdot \hat{E} = -\mathcal{P}\mathcal{E} \sin(kx) \left(\hat{\sigma}_+ + \hat{\sigma}_-\right) \left(\hat{a} + \hat{a}^\dagger\right),$$

where $\mathcal{P} = \langle e|q\hat{\mathbf{r}}|g\rangle$ is the effective electric dipole moment of the atom with q being the charge of an electron. In the rotating wave approximation, which effectively amounts to dropping double excitation terms, we obtain

$$\hat{H}_{\text{int}} = g\hbar \left(\hat{\sigma}_+ \hat{a} + \hat{\sigma}_- \hat{a}^\dagger\right),$$

where $g = -\frac{\mathcal{E}\mathcal{P}}{\hbar} \sin(kx)$ is called single-photon Rabi frequency. The Hamiltonian from Equation 5.1 in the rotating wave approximation

$$\hat{H}_{\text{JC}} = \hbar\omega_A \hat{\sigma}_+ \hat{\sigma}_- + \hbar\omega_A \hat{a}^\dagger \hat{a} + g\hbar \left(\hat{\sigma}_+ \hat{a} + \hat{\sigma}_- \hat{a}^\dagger\right)$$

is called the Jaynes-Cummings Hamiltonian and can be solved analytically by restricting ourselves to the invariant subspace $\{|n+1\rangle \otimes |g\rangle \equiv |n+1, g\rangle, |n\rangle \otimes |e\rangle \equiv |n, e\rangle\}$. Exact diagonalisation of the Jaynes-Cummings Hamiltonian leads to the so-called dressed states which are the eigenstates of the Jaynes-Cummings Hamiltonian

$$|+, n\rangle = \sin\theta_n |n, e\rangle + \cos\theta_n |n+1, g\rangle ,$$
$$|-, n\rangle = \sin\theta_n |n, e\rangle - \cos\theta_n |n+1, g\rangle ,$$

where

$$\cos\theta_n = \sqrt{\frac{\Omega_n - \delta}{2\Omega_n}} \quad \text{and} \quad \sin\theta_n = \sqrt{\frac{\Omega_n + \delta}{2\Omega_n}},$$

with

$$\Omega_n = \sqrt{4g^2(n+1) + \delta^2} \quad \text{and} \quad \delta = \omega_A - \omega_C.$$

The eigenenergies of the dressed states are

$$E_{\pm,n} = \frac{1}{2}\hbar\omega_A + (n+1)\hbar\omega_C \pm \frac{1}{2}\hbar\Omega_n.$$

The energy level structure for the Jaynes-Cummings model is presented in Figure 5.2.

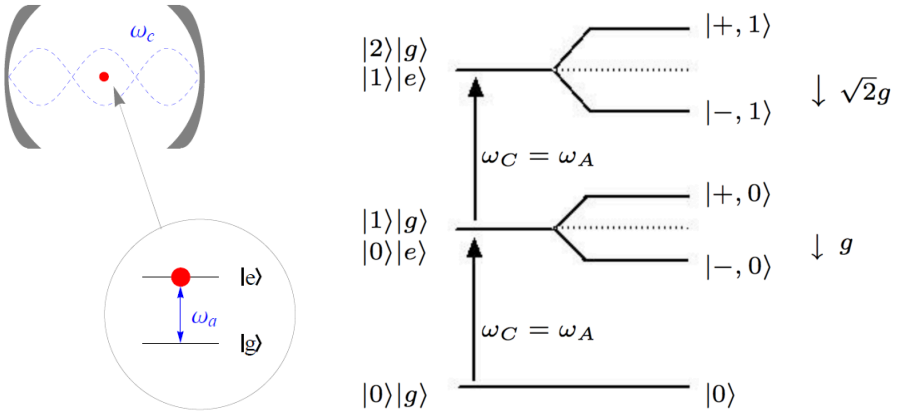

FIGURE 5.2: Left panel: illustration of the Jaynes-Cummings model. In the circle, photon emission and absorption are shown. Right panel: The Jaynes-Cummings energy levels for zero detuning $\delta = 0$. On the left: $g = 0$, on the right: $g \neq 0$. Figures taken from Reference [247]

The generalisation of the Jaynes-Cummings model to N atoms two-level atoms (equivalent to spin $N/2$) interacting with a single mode field is known as the Dicke model or the Tavis-Cummings model, which is introduced in the next Chapter.

The Jaynes-Cummings Hamiltonian does not include any coupling to the environment. In order to include the loss-mechanisms, namely spontaneous decay into the vacuum modes from $|e\rangle$ (rate Γ) and decay of the field mode (rate κ), usually caused by imperfect mirrors, one has to use a master equation approach or, to be more precise, the Lindblad master equation [248].

5.2 The Lindblad master equation

In this Section, we will introduce the Lindblad master equation. The following introduction is somewhat superficial since a detailed derivation reaches far beyond the scope of this thesis. An excellent and comprehensive introduction can be found in the Reference [249] and also in a more recent publication from Reference [250].

As a matter of fact, describing a system by a pure state is only an idealisation. Any quantum state that we can think of is inherently connected with its environment via some interaction which effectively entangles the two parties [21]. Haroche and Raimond wrote [249]:

> Whatever care is exercised to protect it, a quantum system A interacts, if only slightly, with its environment E. Information about the system's state is always leaking into the correlations building up between A and E. In other words, the environment, as a quantum version of Orwell's Big Brother, is continuously 'watching' the system and collecting information about it.

As a consequence, some information about A leaks to the environment E and *vice versa*. Then, the concept of a pure state of the subsystem A becomes inadequate since it no longer contains all the information about A. Therefore A cannot be described by a ket, but a density matrix which somehow reflects our lack of the full knowledge about the subsystem A.

The interaction of the environment also affects the dynamics of a subsystem; therefore, the Heisenberg equation of motion is inadequate in this situation. Nevertheless, the dynamics of A, technically speaking for its reduced density matrix $\hat{\rho}_A$, can be described by a master equation.

In the most general case, a linear quantum process transforming a density matrix into another one results from the coupling of the system with the environment. Mathematically speaking, the process of transformation of the initial density matrix $\hat{\rho}_A$ into a new one, is described by a linear map $\mathcal{L}_A$

$$\hat{\rho}_A \to \mathcal{L}_A(\hat{\rho}_A).$$

$\mathcal{L}_A$ is often called the super-operator because it is a linear operator in the super-Hilbert space of the operators acting in the Hilbert space of the system. These super-operators can also be expressed in terms of Hilbert space operators, the so-called Kraus operators [251], in the following way

$$\mathcal{L}_A(\hat{\rho}_A) = \sum_\mu \hat{M}_\mu \hat{\rho}_A \hat{M}_\mu^\dagger,$$

where the sum goes over maximally N_A^2 elements, where N_A is the dimension of Hilbert space of the subsystem A. The Kraus operators obey the normalisation condition

$$\sum_\mu \hat{M}_\mu \hat{M}_\mu^\dagger = \hat{I},$$

hence ensuring that the trace of the density matrix is preserved.

In general, it is not always possible to define a linear map deducing the state of the subsystem A after its interaction with the environment from the knowledge of $\hat{\rho}_A$ alone. The existence of a quantum map describing the effect of an environment E on a system A is guaranteed only if A and E are not initially entangled. This seems as an

extreme restriction because the interaction with the environment always introduces some correlations. However, when E is a large system with a short memory time, the effect of these correlations is rapidly washed out, and the linear quantum map describing the evolution of $\hat{\rho}_A$ can be found. This is exactly the claim of the Born-Markov approximation which states that the environment is big enough so that it effectively acts as a reservoir which does not 'feel' the interaction with the subsystem A, or in other words, the environment is never correlated with the subsystem A, and moreover, the state of the environment does not change in time. According to this, we can describe a map that takes a density matrix at time t and brings it to time $t+\tau$:

$$\hat{\rho}_A(t+\tau) = \mathcal{L}_\tau\left[\hat{\rho}_A(t)\right] = \sum_\mu \hat{M}_\mu(\tau)\hat{\rho}(t)\hat{M}_\mu^\dagger(\tau),$$

and define the derivative of $\hat{\rho}_A(t)$ with respect to t as

$$\frac{\mathrm{d}\hat{\rho}_A(t)}{\mathrm{d}t} = \frac{\mathcal{L}_\tau\left[\hat{\rho}_A(t)\right] - \hat{\rho}_A(t)}{\tau}.$$

Now, since $\mathcal{L}_\tau\left[\hat{\rho}_A(t)\right] = \hat{\rho}_A(t+\tau) = \hat{\rho}_A(t) + \mathcal{O}(\tau)$, where $\mathcal{O}(\tau)$ is a first order contribution in τ, one of the operators $\hat{M}_\mu$ must be of the order of unity, and can be written as

$$\hat{M}_0 = \hat{I} - i\hat{K}\tau + \mathcal{O}(\tau^2),$$

where $\hat{K}$ is an operator independent of τ. Now, let us isolate the Hermitian part of $\hat{K}$ and its anti-hermitian part, and define two new operators

$$\hat{H} = \hbar\frac{\hat{K}+\hat{K}^\dagger}{2} \quad \text{and} \quad \hat{J} = i\frac{\hat{K}-\hat{K}^\dagger}{2},$$

so that

$$\hat{K} = \frac{\hat{H}}{\hbar} - i\hat{J}.$$

Therefore, up to the first order in τ, we have:

$$\hat{M}_0(\tau)\hat{\rho}_A\hat{M}_0^\dagger(\tau) = \hat{\rho}_A - \frac{i\tau}{\hbar}\left[\hat{H},\hat{\rho}_A\right] - \tau\left(\hat{J}\hat{\rho}_A + \hat{\rho}_A\hat{J}\right).$$

The second term on the right hand side of the above equation resembles a commutator describing a unitary evolution of $\hat{\rho}_A$ governed by Hamiltonian $\hat{H}$. What does the third term correspond to? In order to answer this question, let us focus on all the other terms of $\hat{M}_\mu$ with $\mu \neq 0$, which are of the order of $\sqrt{\tau}$ since all the other terms in the Kraus sum from Equation 5.2 are of the order of τ. For $\mu \neq 0$ we can thus write

$$\hat{M}_\mu(\tau) = \sqrt{\tau}\hat{L}_\mu,$$

where $\hat{L}_\mu$ are τ-independent operators of the order of unity. The normalisation of the Kraus sum can be expressed then as

$$\sum_\mu \hat{M}_\mu^\dagger(\tau)\hat{M}_\mu(\tau) = \hat{I} - 2\hat{J}\tau + \sum_{\mu\neq 0}\tau\hat{L}_\mu^\dagger\hat{L}_\mu = \hat{I},$$

and thus we can write

$$\hat{J} = \frac{1}{2}\sum_{\mu\neq 0}\hat{L}_\mu^\dagger \hat{L}_\mu.$$

Arranging all terms together, we finally get the master equation for $\hat{\rho}_A$, in a generic form, the Lindblad expansion:

$$\frac{\mathrm{d}\hat{\rho}_A}{\mathrm{d}t} = -\frac{i}{\hbar}\left[\hat{H}_A, \hat{\rho}_A\right] + \sum_{\mu\neq 0}\left(\hat{L}_\mu\hat{\rho}_A\hat{L}_\mu^\dagger - \frac{1}{2}\hat{L}_\mu^\dagger\hat{L}_\mu\hat{\rho}_A - \frac{1}{2}\hat{\rho}_A\hat{L}_\mu^\dagger\hat{L}_\mu\right).$$

Physically, operators $\hat{L}_\mu$ describe the interaction between system A and its environment, and they are composed of two components:

$$\hat{L}_\mu = \sqrt{\Gamma_\mu}\hat{J}_\mu,$$

where Γ_μ and $\hat{J}_\mu$ correspond to the mechanism of the interaction and the interaction rate, respectively. The operators $\hat{J}_\mu$ are often referred to as the jump operators since they describe a drastic change of the state. As a matter of fact, the physical interpretation of the master equation in the Lindblad form is transparent, and it is possible, in many cases, to guess the form of $\hat{L}_\mu$ operators by a simple description of the relaxation events which affect system A. Indeed, if we are able to identify what can happen to the state of A, we can infer the form of the jump operators $\hat{J}_\mu$ and thus guess the structure of the Lindblad master equation.

In order to get some insight into the Lindblad master equation, let us consider a simple case of a two-level atom emitting a spontaneous photon in free space. Let us imagine a *gedanken* experiment in which the atom is surrounded by ideal photon detectors, so it is impossible to fail to detect the emitted photon. During a time interval, τ two things can happen. A photon can be either detected or not. From the law of energy conservation, the detection of a photon must correspond to a projection of the atom onto its ground state. Therefore, there is only one jump operator that describes the jump from the excited to the ground state, which is the lowering operator $\hat{\sigma}_-$, and the master equation is

$$\frac{\mathrm{d}\hat{\rho}_A}{\mathrm{d}t} = -\frac{i}{\hbar}\left[\hat{H}_A, \hat{\rho}_A\right] - \frac{\Gamma}{2}\left(\hat{\sigma}_+\hat{\sigma}_-\hat{\rho}_A + \hat{\rho}_A\hat{\sigma}_+\hat{\sigma}_- - 2\hat{\sigma}_-\hat{\rho}_A\hat{\sigma}_+\right),$$

where $\hat{H}_A = \omega_0\hat{\sigma}_z$. To make it more explicit, we can write the above Equation in terms of atomic populations ($\hat{\rho}_{Aee}$ and $\hat{\rho}_{Agg}$) and coherences ($\hat{\rho}_{Age} = \hat{\rho}_{Aeg}$)

$$\frac{\mathrm{d}\rho_{Aee}}{\mathrm{d}t} = -\Gamma\rho_{Aee}, \quad \frac{\mathrm{d}\rho_{Agg}}{\mathrm{d}t} = \Gamma\rho_{Agg}, \quad \frac{\mathrm{d}\rho_{Aeg}}{\mathrm{d}t} = -i\omega_0\rho_{Aeg} - \frac{\Gamma}{2}\rho_{Aeg}.$$

These equations describe the well-known statistical features of the spontaneous emission: an exponential decay of the excited state probability with the rate Γ and of the atomic coherence with the rate $\Gamma/2$. Note that Γ cannot be obtained through the simple and general argument leading to the Lindblad form of the master equation. It can, however, be determined by a Fermi golden-rule argument describing explicitly the coupling of the atomic transition to the continuum of field modes.

5.3 Quantum non-demolition measurement

Finally, let us focus on a very special kind of a measurement where an atom crossing the cavity can detect even a single photon without destroying it.

According to quantum mechanics, any quantum system upon a measurement of an observable should end up in an eigenstate corresponding to the measured eigenvalue. Mathematically, measuring observable $\hat{O}$ can yield any of the results O_1, O_2, O_3, ..., which are eigenvalues of $\hat{O}$ with corresponding probabilities given by

$$\Pr(\hat{O}_n) = \mathrm{Tr}\left[\hat{P}_n\hat{\rho}\right],$$

where $\hat{P}_n$ is the projection operator associated with the eigenvalue O_n. If the result of the measurement is n, then the initial density matrix $\hat{\rho}$ collapses to

$$\hat{\rho}' = \frac{\hat{P}_n\hat{\rho}\hat{P}_n}{\mathrm{Tr}\left[\hat{P}_n\,\hat{\rho}\right]}.$$

In a more general case, when the outcome of a measurement is not checked, the state of the system is randomly projected into one of the states described by $\hat{P}_n\hat{\rho}\hat{P}_n$, and thus leading to a mixed state

$$\hat{\rho}'' = \sum_n \hat{P}_n\hat{\rho}\hat{P}_n$$

which describes our lack of knowledge about the system's state. However, from the viewpoint of an experiment, this is not what happens. Let us consider a process of photo-detection of a field mode, where usually the measured quantity is the photon-number operator $\hat{N} = \hat{a}^\dagger\hat{a}$. The process of photo-detection relies on the photo-electric effect, which converts photons into the current and thus destroys the photons. In other words, the quantum state of light is always cast onto the vacuum state, so the state is not projected but instead demolished.

A quantum non-demolition measurement is a measurement which projects the state into the eigenstate corresponding to the measurement outcome and thus preserves the state for subsequent processing. The second essential feature in the definition of the quantum non-demolition measurement is its repeatability. According to the definition of a projective measurement, another projective measurement yields the same result:

$$\hat{P}_n\left|\psi\right\rangle = \left|P_n\right\rangle\left\langle P_n\right|\sum_n c_m\left|P_m\right\rangle = c_n\left|P_n\right\rangle,$$

so applying another projective measurement yields

$$\hat{P}_n c_n\left|P_n\right\rangle = \left|P_n\right\rangle\left\langle P_n\right| c_n\left|P_n\right\rangle = c_n\left|P_n\right\rangle.$$

In order to speak about a quantum non-demolition measurement, there should be no evolution between the two projective measurements; otherwise, the eigenstate produced in the first measurement may evolve and expand along different eigenstates as time goes on, and thus may change the result of the second projective measurement. This puts severe limitations on the kinds of systems and observables on which quantum non-demolition measurements can be performed.

In a quantum non-demolition measurement setup, we typically consider the measured system S which is coupled with a meter M. The Hamiltonian of the whole system comprises of three terms:

$$\hat{H} = \hat{H}_S + \hat{H}_M + \hat{H}_{SM},$$

describing the measured system $\hat{H}_S$, the meter $\hat{H}_M$, and their mutual interaction $\hat{H}_{SM}$. The quantum non-demolition measurement requires the Hamiltonian to satisfy certain conditions, which have been defined in details in Reference [252]. First of all, we need some information about the whole system to be contained in the observable $\hat{O}_M$ of the meter. Therefore the interaction part must not commute with the meter's observable

$$\left[\hat{H}_{SM}, \hat{O}_M\right] \neq 0.$$

Another requirement for the quantum non-demolition measurement is that the measurement should not affect the eigenstates of the measured observable of the measured system $\hat{O}_S$. This is the case when $\hat{H}_{SM}$ commutes with $\hat{O}_S$

$$\left[\hat{H}_{SM}, \hat{O}_S\right] = 0.$$

Finally, we must impose another condition on the eigenstates of $\hat{O}_S$ which is related to the repeatability of the measurement. If we do not restrict ourselves to high-speed processes, the eigenstates of $\hat{O}_S$ should be immutable under the action of the free system's Hamiltonian $\hat{H}_S$. This condition implies that $\hat{O}_S$ must be a constant of motion for $\hat{H}_S$:

$$\left[\hat{H}_S, \hat{O}_S\right] = 0.$$

A quantum non-demolition measurement inside an optical cavity was first performed by the group of Haroche at the École Normale Supérieure in Paris. In the experiment described in Reference [253], a method for preparation of small-photon-number Fock states was proposed. The experiment was based on measuring the phase shift of the atomic wavefunction after interaction with the electromagnetic field by the Ramsey separated-oscillatory-fields technique. The Fock states are not the only, non-classical states that can be prepared in an optical cavity. As a matter of fact, the same setup can be used to create quantum superpositions of classical fields, and even the most entangled Schrödinger's cat state [114].

We now apply described methods to show the generation of non-classical light in a cavity and its exploitation in interferometric phase measurement.

5.4 Generation of a non-classical cavity field

We consider an atom with three energetic levels (see Figure 5.3) initially prepared in the ground state c and subsequently put into a superposition of b and c

$$|\psi_A\rangle = \frac{1}{\sqrt{2}}\left(|b\rangle + |c\rangle\right)$$

by performing a $\pi/2$-pulse. Following this, such a prepared atom passes through the cavity and interacts there with a single-mode field:

$$|\psi_L\rangle = \sum_{n=0}^{\infty} C_n |n\rangle ,$$

where $|C_n|^2$ is the probability of measuring n photons inside the optical cavity.

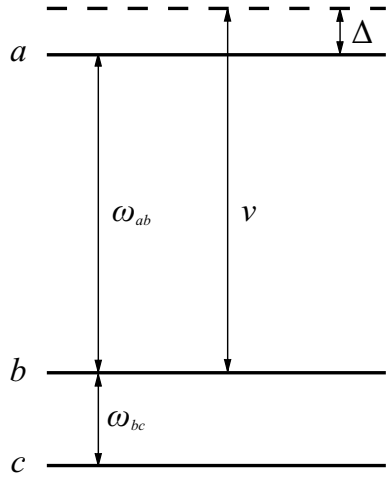

FIGURE 5.3: Cascade configuration of a three level atom. Transitions $a \leftrightarrow b$ and $b \leftrightarrow c$ are allowed, and $a \leftrightarrow c$ is forbidden. The frequency of the cavity field ν is detuned from $a \leftrightarrow b$ transition by $\Delta \equiv \nu - \omega_{ab}$. Figure taken from Reference [245].

We assume that the detuning Δ of the light frequency with respect to the atomic transition ω_{ab} is large, *i.e.*,

$$\frac{4g^2 n}{\Delta} \ll 1,$$

where g is the strength of atom-light interaction and n is the number of photons. In this limit, the first excited state b gains a phase factor (known as the dispersive phase shift)

$$|b\rangle \rightarrow e^{-inU_0 t} |b\rangle ,$$

where $U_0 = g^2/\Delta$, and t is the duration of atom-light interaction, while the amplitudes do not change meaning that the occupation of the higher excited state a is negligible. As the atom exits the cavity, another $\pi/2$-pulse acts on the state creating thus an atom entangled with the cavity field.

$$|\psi_{A+L}\rangle = \sum_{n=0}^{\infty} C_n e^{-i\frac{nU_0 t}{2}} |n\rangle \otimes \left[\sin\left(\frac{nU_0 t}{2}\right)|b\rangle - \cos\left(\frac{nU_0 t}{2}\right)|c\rangle\right]$$

Finally, the atomic state is measured and thus projected onto one of its energetic states b or c. Assuming that the state of the atom after this measurement is $|b\rangle$ and the cavity light is described by a coherent state with amplitude α, the final state of

the field reads:

$$|\psi_L\rangle = \frac{1}{\sqrt{\mathcal{A}}} \sum_{n=0}^{\infty} C_n e^{-i\frac{nU_0t}{2}} \sin\left(\frac{nU_0t}{2}\right) |n\rangle ,$$

where $C_n = e^{-|\alpha|^2/2}\alpha^n/\sqrt{n!}$ and $\mathcal{A}$ is the normalisation factor

$$\mathcal{A} = \frac{1}{2}\left[1 - e^{|\alpha|^2(\cos(U_0t)-1)} \cos\left(|\alpha|^2 \sin(U_0t)\right)\right] .$$

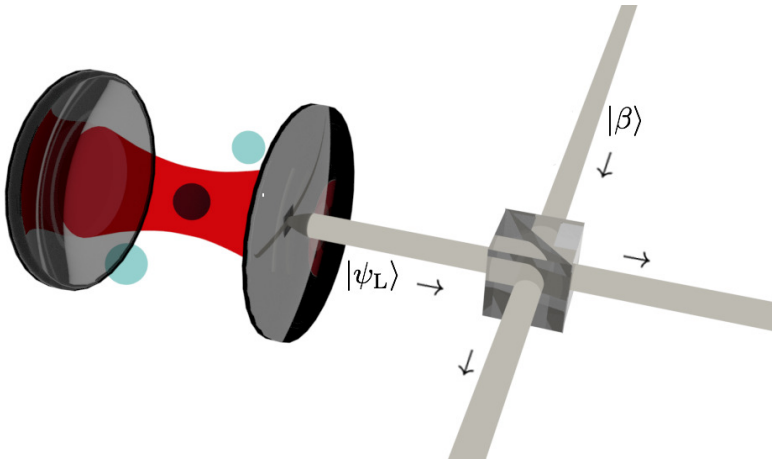

FIGURE 5.4: A schematic illustration presenting the setup. On the left side, an atom passes the optical cavity where it interacts with the electromagnetic field. When the atom leaves the cavity, its state is measured, and resulting state of the light is extracted from the cavity. The extracted beam is mixed with another coherent field $|\beta\rangle$ on a beam-splitter being an element of the Mach-Zehnder interferometer. Figure taken from Reference [245].

Alternatively, the state from Equation 5.4 can be rewritten as a superposition of two coherent states

$$|\psi_L\rangle \propto |\alpha e^{-iU_0t}\rangle - |\alpha\rangle ,$$

generally known as Schrödinger's kittens [254] which for $U_0t = \pi$ becomes a maximally entangled Schrödinger's cat (See also Section 1.5 in Chapter 1). In what follows, we focus on exploiting non-classicality of these type of states in quantum-enhanced interferometry.

5.5 Interferometric scheme and characterization

The generated non-classical state is now mixed on a beam-splitter with a coherent state $|\beta\rangle$ meaning that the initial state is described by

$$|\psi\rangle = |\psi_L\rangle_a \otimes |\beta\rangle_b ,$$

where a and b stands for the two modes of light. The Mach-Zehnder interferometer transforms this state according to

$$|\psi(\theta)\rangle = e^{-i\theta\hat{J}_y}\left[|\psi_L\rangle_a \otimes |\beta\rangle_b\right],$$

where θ is the unknown parameter that we want to estimate.

Before calculating quantum Fisher information, we want to note that the precision of the estimation of θ is linked to the distinguishability of neighbouring states along a path characterised by θ

$$|\langle\psi(\theta)|\psi(\theta+\delta\theta)\rangle| \simeq 1 - \frac{(\delta\theta)^2}{4}F_q,$$

which can also be expressed using the Wigner function

$$|\langle\psi(\theta)|\psi(\theta+\delta\theta)\rangle| = \pi\int \mathrm{d}\alpha W(\alpha)W(\alpha+\delta\alpha).$$

However, it is not clear how $\delta\theta$ relates to $\delta\alpha$. To resolve this issue, we assume that the intensity of the coherent beam $|\beta\rangle$ is high and replace the creation and annihilation operators for mode b with complex numbers β^* and β. According to this, we can rewrite the Mach-Zehnder transformation as

$$e^{-i\theta\hat{J}_y} = e^{-\frac{\theta}{2}\left(\hat{a}^\dagger\hat{b}+\hat{b}^\dagger\hat{a}\right)} \approx e^{-\frac{\theta}{2}\left(\hat{a}^\dagger\beta+\hat{\beta}^*\hat{a}\right)},$$

which turns out to be a displacement operator with a displacement of $|\beta|\theta/2$ in the direction set by the phase of β (denoted hereinafter by ϕ_β) (see Section 1.1 in Chapter 1); Therefore $\delta\alpha = |\beta|\delta\theta/2$. By combining Equations 5.5 and 5.5, we conclude that large values of quantum Fisher information require minimal overlap between neighbouring states. Interestingly the direction of the optimal displacement (the value of ϕ_β) can be read from the Wigner function (see Figure 5.5). To obtain a minimal overlap of the Wigner function (maximal quantum Fisher information) one ought to shift it along a direction perpendicular to the interference fringes. For instance, for $U_0t = \pi/2$ (Figure 5.5b) the phase ϕ_β should be equal to $\pi/4$, while for $U_0t = \pi$ (Figure 5.5d) the phase ϕ_β should be equal to π in order to make a translation along the imaginary axis.

When the overlap between the two coherent states from Equation 5.4 is negligible, the optimised quantum Fisher information (for every t with respect to the phase ϕ_β) reads

$$F_q \approx n_\alpha + n_\beta + 4n_\alpha n_\beta \sin^2\left(U_0t\right),$$

where n_α and n_β is the mean number of photons in mode a and b, respectively. For clarity, we fix now ϕ_β to 0, and take real α, so that the quantum Fisher information is approximately

$$F_q^{\phi_\beta=0} \approx n_\alpha + n_\beta + n_\alpha n_\beta \sin^2\left(\frac{U_0t}{2}\right).$$

Although this is not an optimal choice, it still can give a Heisenberg scaling of the sensitivity.

With these results at hand, we are now in the position to calculate the sensitivity of a particular estimation scheme. We assume that we perform a measurement of

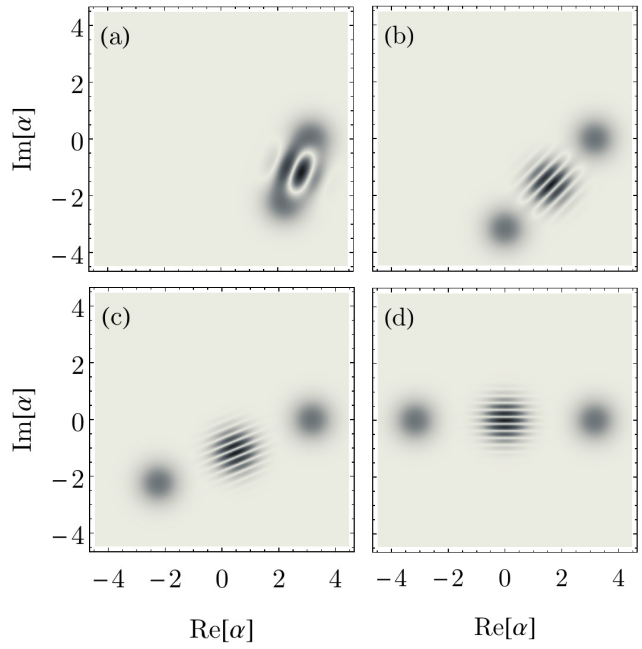

FIGURE 5.5: Wigner function of the state (5.4) displayed at $U_0 t = \pi/4$ **(a)**, $U_0 t = \pi/2$ **(b)**, $U_0 t = 3\pi/4$ **(c)** and $U_0 t = \pi$ **(d)**. Directions perpendicular to fringes indicate the direction of the optimal interferometer or the optimal value of the phase ϕ_β. Figure taken from Reference [245].

the output photons. The probability of measuring n photons at one output port and m at the second one is

$$p_{nm}(\theta) = |\langle n, m|\psi(\theta)\rangle|^2,$$

where $|n, m\rangle$ is a shorthand notation for $|n\rangle \otimes |m\rangle$. If we now use the maximum likelihood estimator the sensitivity is related to the Fisher information

$$F_c = \sum_{n,m} \frac{1}{p_{nm}(\theta)} \left(\partial_\theta p_{mn}(\theta)\right)^2$$

through the Cramér-Rao bound (see Section 3.2 in Chapter 3). Figure 5.6 shows the comparison between quantum Fisher information and its classical counterpart for two values of the unknown parameter θ. Although classical Fisher information exhibits strong dependence on θ, numerical calculations reveal that for $\theta = 0$ quantum Fisher information is greater than classical Fisher information only by a constant factor of $(n_\alpha + n_\beta)/2$, retaining thus the Heisenberg scaling.

The strong dependence of the Fisher information on θ is a result of a strong dependence of the probability from Equation 5.5 on θ. To see that, we choose the subspace of a constant number of photons $n + m = 40$ and show the probability as a function of the unknown parameter θ and the relative number of photons $\Delta n = n - m$. The fine structures visible in Figure 5.7 are responsible for the high interferometric signal. Similarly, as in the previous Chapter, it is possible to read the optimal operating range of probability. For instance, the probability from Figure 5.7c shows a strong dependence on θ at every point meaning that the sensitivity of the

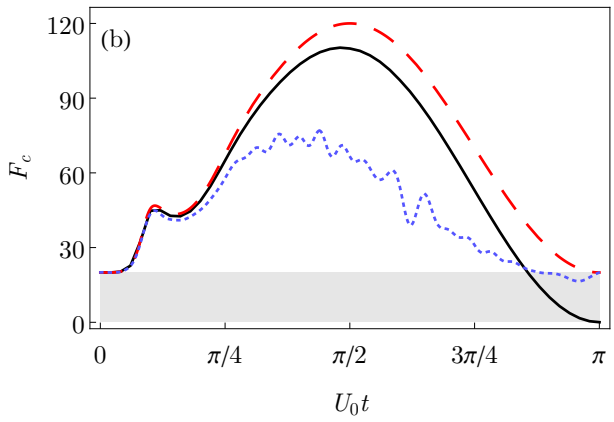

FIGURE 5.6: $\phi_\beta = 0$ case: the classical Fisher information at $\theta = 0$ (solid black) and $\theta = \pi/13$ (dotted blue), compared with the quantum Fisher information (dashed red). All results for $n_{\alpha/\beta} = 10$. The grey area represents the classical interferometry regime. Figure taken from Reference [245].

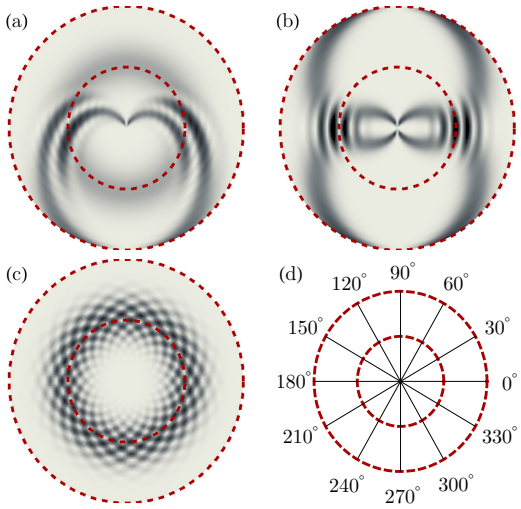

FIGURE 5.7: The probability of measuring a fixed number of photons ($N = 20$) as a function of θ (polar variable) and relative photon number Δn (radial variable). **(a)** and **(b)** correspond to real β with $U_0 t = \pi/2$ and $U_0 t = \pi$. **(c)** used imaginary β and $U_0 t = \pi$, **(d)** is the polar grid. Darker regions correspond to larger probability. Figure taken from Reference [245].

estimation does not depend on θ as opposed to the probability from 5.7a where the probability shows a strong dependence on θ around 0 and π.

5.6 Impact of imperfections

Finally, let us take into account the processes that lead to the deterioration of the sensitivity. The first process we focus on is the loss of photons from the cavity which we account for by incorporating a Lindblad term into the Heisenberg equation of

motion

$$\begin{aligned}\partial_t\hat{\rho} &= -\frac{i}{\hbar}\left[\hat{H},\hat{\rho}\right] + \mathcal{L}[\hat{\rho}] \\ &= -\frac{ig^2}{\hbar\Delta}\left[\hat{a}^\dagger\hat{a}\left|b\right\rangle\left\langle b\right|,\hat{\varrho}\right] + \kappa\left(\{\hat{a}^\dagger\hat{a},\hat{\varrho}\} - 2\hat{a}\hat{\rho}\hat{a}^\dagger\right),\end{aligned}$$

where κ is the photon loss rate. Although it is no longer possible to perform analytical calculations, numerical simulations show that there exist a time scale τ associated with the interactions and photon loss rate

$$\kappa\tau(U_0\tau)^2 n_\alpha = 1.$$

For times such that $t \lesssim \tau$, we observe that the numerical results are well fitted with the following formula:

$$F_q \approx n_\alpha + n_\beta + \exp\left[-\frac{2}{3}\left(\frac{t}{\tau}\right)^3\right]\sin^2(U_o t) n_\alpha n_\beta.$$

This phenomenological formula illustrates how the nonlinear term responsible for the sub-shot-noise scaling is suppressed by photon losses. The suppression becomes more significant as the number of photons n_α is increased and also for longer times. This should not come as a surprise since more photons and longer times lead to the creation of highly entangled states which are extremely fragile to decoherence. As a consequence, there exists an optimal operating regime for an interferometer and in realistic conditions it is more beneficial to create moderately entangled states that are not that fragile against decoherence but still can give sub-shot-noise sensitivity. Moreover, Equation 5.6 can serve as a rough estimate for the optimal working point of the interferometer.

Before calculating the classical Fisher information, we can ask an interesting question: what happens with the fine structures under the action of decoherence? To answer this question, we plot the photon number distribution of the Schrödinger's cat and show how losses of photons affect the fine structures. As can be seen in Figure 5.8a, even moderate losses can smooth out the fine structures that give rise to the high interferometric signal. This has profound consequences for the classical Fisher information and thus for the sensitivity of estimation. Now, the Fisher information is calculated according to Equation 5.5 with probability

$$p_{nm}(\theta) = \mathrm{Tr}\left[\left|n,m\right\rangle\left\langle n,m\right|\hat{\rho}(\theta)\right].$$

The comparison between quantum Fisher information and classical Fisher information for various values of κ is presented in Figure 5.8b. Apart from decreasing, the classical Fisher information also exhibits oscillations which can be smoothed out by choosing an optimal θ at each instant of time.

Another limitation that we want to focus on is the finite resolution of photon counters. Note that in the previous Chapter the finite resolution of atom detectors was much more severe to the sensitivity than lack of precise knowledge about the state. The imperfect photon counters are modelled by convoluting the probability from Equation 5.5 with a Gaussian distribution

$$\mathcal{P}_{nm}(\theta) = \mathcal{N}\sum_{n',m'=0}^{\infty} p_{nm}(\theta) e^{-\frac{(n'-n)^2+(m'-m)^2}{2\sigma^2}},$$

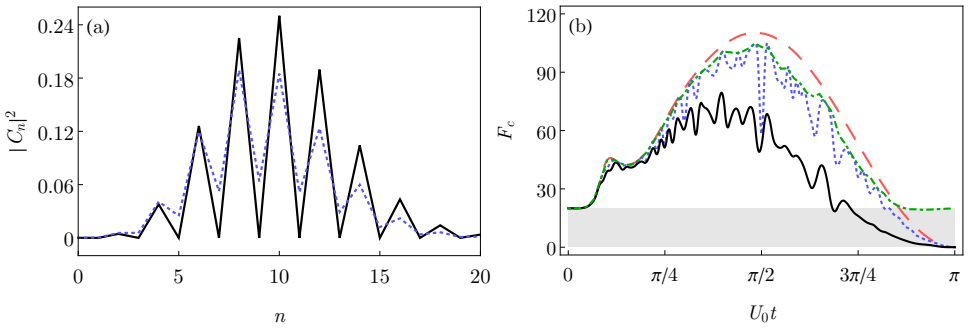

FIGURE 5.8: **(a)** Effect of the photon losses on the number distribution of the light field with initially $n_\alpha = 10$, outgoing from the cavity at $U_0 t = \pi$ for an ideal case (solid black line) and $\kappa = 10^{-2}$ case (dotted blue line). **(b)** The Fisher information calculated at $\theta = 0$ with $n_{\alpha/\beta} = 10$ for: $\kappa = 0$ (dashed red), $\kappa = 10^{-3}$ (dotted blue) and $\kappa = 10^{-2}$ (solid black). Dot-dashed green line is the $\kappa = 10^{-3}$ case optimized over θ for every instant. Figure taken from Reference [245].

where $\mathcal{N}$ is the normalisation factor and σ accounts for the resolution of the detectors. The classical Fisher information for three various values of σ are presented in Figure 5.9. As expected the finite resolution of detectors are much more severe than decoherence arising from the loss of photons. However, it is still possible to retain sub-shot-noise sensitivity even when the detectors are not perfect.

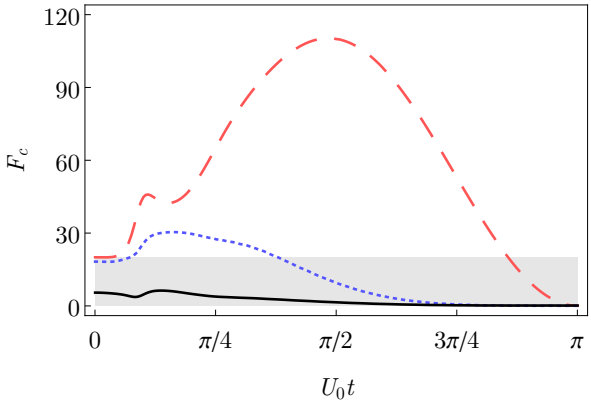

FIGURE 5.9: Fisher information with imperfect detectors for $n_{\alpha/\beta} = 10$ and $\sigma = 0$ (dashed red), $\sigma = 1$ (dotted blue) and $\sigma = 5$ (solid black). Figure taken from Reference [245].

5.7 Implementation

Finally, let us focus on the implementation of the foregoing estimation protocol. As has been stated in the introduction to this Chapter, the creation of such entangled states was realised by using the superconductive microwave cavities [255, 256]. These ideas were also extended to the optical regime [257, 258], where it is much easier to exploit photons due to their long-distance propagation. The most important, as well as fragile, part of the proposed interferometric scheme is the extraction of the photons from the cavity. On the one hand, the leakage of photons from the cavity

leads to decoherence and hence limits the interferometric precision, but on the other hand, the non-classical field in the cavity can be transformed into an entangled state only when the photons are extracted from the cavity through the mirrors, which act as beam splitters. Unfortunately, for the highly non-classical cat states, even a single loss of a photon renders the output state classical [116]. However, it is still possible to beat the shot-noise limit even with an imperfect extraction of photons provided that the generated states are moderately non-classical.

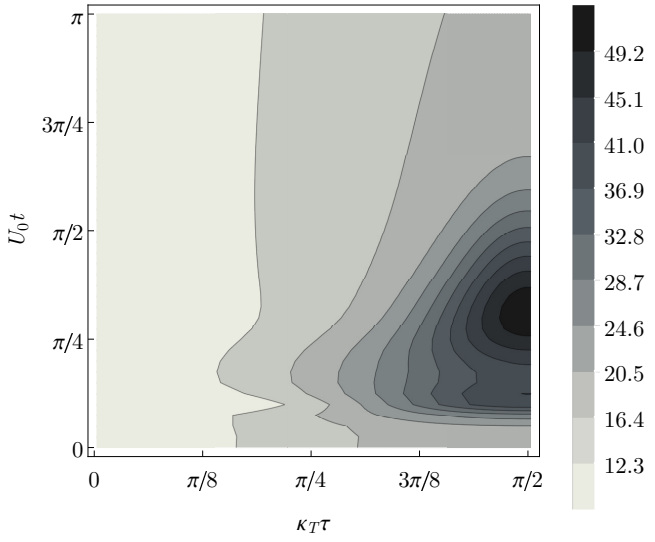

FIGURE 5.10: Quantum Fisher information for Mach-Zehnder interferometer as a function of $U_0 t$ and transfer time $\kappa_T \tau$ calculated by taking the light extracted from the cavity on one of the interferometer's input port and a coherent field on the other one. Here $\kappa_T = 0.049$ and $\tilde{\kappa} = 0.001$. At transfer time equal to $\pi/2\kappa_T$ all the photons are extracted from the cavity, and at interaction time π/U_0 the cat state is created in the cavity. Figure taken from Reference [245].

To examine how quantum Fisher information is affected by imperfect extraction of the non-classical field from the cavity, we propose a simple but qualitative model which treats the extracted photons as a new mode $\hat{c}$. In this model, one of the cavity mirrors serves as a beam-splitter leading to the following equation of motion

$$\begin{aligned} \partial_t \hat{\rho} &= -\frac{i}{\hbar}\left[\hat{H}_T, \hat{\rho}\right] + \mathcal{L}\left[\hat{\rho}\right] \\ &= -\frac{i\kappa_T}{\hbar}\left[\hat{a}^\dagger \hat{c} + \hat{c}^\dagger \hat{a}, \hat{\rho}\right] + \tilde{\kappa}\left(\{\hat{a}^\dagger \hat{a}, \hat{\rho}\} - 2\hat{a}\hat{\rho}\hat{a}^\dagger\right), \end{aligned}$$

where κ_T is the photon extraction rate (related to κ from Equation 5.6) and $\tilde{\kappa}$ is the photon loss rate corresponding to the absorption of photons within the mirror. Quantum Fisher information calculated for the new mode $\hat{c}$ is presented in Figure 5.10. As expected, the optimal state with respect to the sensitivity is not the highly entangled Schrödinger's cat state, but a moderately entangled superposition of two coherent state visible in Figure 5.5a. As a matter of fact, in a standard Fabry-Perot cavity, the cavity loss rate κ and the transfer rate κ_T are not independent and essentially of the same order. Therefore, a desired experimental setup should include the possibility of controlling the loss rate. In the preparation stage, when the non-classical state is being generated, it should be as low as possible, while in the extraction stage it

should be switched to a higher value enabling thus for fast extraction of the non-classical state. Although such a control is a challenging task, it can be realised in nano-fibre setups with evanescent wave coupling. The quick tuning of the cavity decay and coupling minimises mirror losses and allows for optimised routing and photon out-coupling [259].

Chapter 6

Chaos Metrology

Chaos is a branch of mathematics which studies the behaviour of systems that are extremely sensitive to the initial conditions. Even a small change of some parameters can result in widely diverging trajectories for chaotic systems, which effectively makes them unpredictable. This randomness, however, is only apparent since the systems' behaviour is completely determined by the initial conditions. The chaos theory was summarised by Edward Lorenz as [260]:

> Chaos: When the present determines the future, but the approximate present does not approximately determine the future.

In this chapter, based on Reference [261], we focus on the exploitation of quantum Fisher information in chaotic systems. Although quantum chaos in terms of exponential divergence of initially nearby trajectories does not exist, and therefore it cannot be used to increase the phase sensitivity, quantum Fisher information can be used to study chaotic transitions and characteristic time-scales, for instance, the Ehrenfest time which heralds the breakdown of the correspondence between the classical and quantum dynamics.

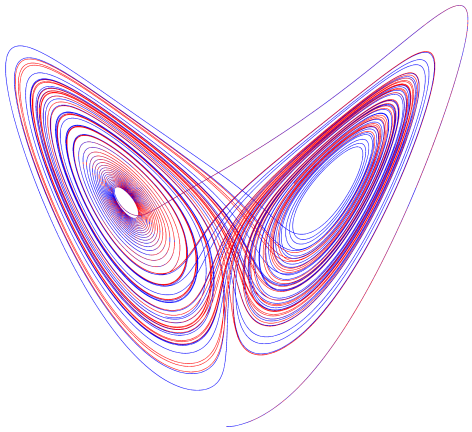

FIGURE 6.1: Chaotic solution of the Lorenz system known as the Lorenz attractor. Figure from Reference [262]

Contents

6.1 Chaos

We begin with an elementary dynamical system that consists of two connected pendula, each of length l and mass m, known as a double-rod pendulum. This rudimentary system exhibits surprisingly rich dynamics with a high sensitivity to initial conditions and therefore is considered as one of the most paradigmatic cases of classical chaos.

To describe the system, we need the angles between each rod and the vertical, denoted by θ_1 and θ_2. If we take the origin of the system to be located at the point of the suspension of the upper pendulum, the centre of mass position of each rod can be described as:

$$x_1 = \frac{l}{2}\sin\theta_1$$
$$y_1 = -\frac{l}{2}\cos\theta_1$$

$$x_2 = l\left(\sin\theta_1 + \frac{1}{2}\sin\theta_2\right)$$
$$y_2 = -l\left(\cos\theta_1 + \frac{1}{2}\cos\theta_2\right),$$

where subscripts 1 and 2 denote the upper (first) and lower (second) rod. With de-

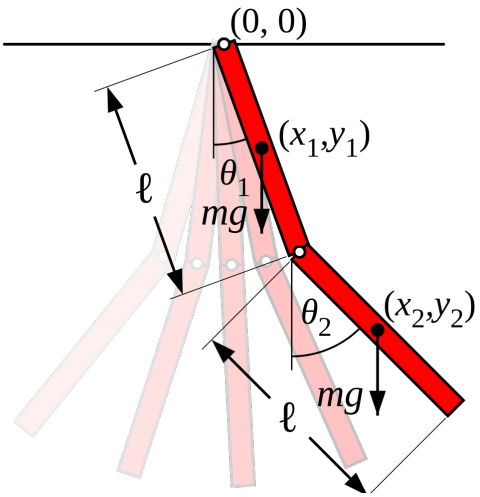

FIGURE 6.2: Schematic representation of a double-rod pendulum. Figure taken from Reference [263]

fined coordinates we can proceed to write the Lagrangian of the system

$$L = \frac{1}{2}m\left(\dot{x}_1^2 + \dot{y}_1^2 + \dot{x}_2^2 + \dot{y}_2^2\right) + \frac{1}{2}I\left(\dot{\theta}_1^2 + \dot{\theta}_2^2\right) - mg\left(y_1 + y_2\right),$$

where $I = \frac{1}{12}ml^2$ is a moment of inertia of a single pendulum, and the dot denotes the derivative with respect to time. Combining the above equations gives

$$L = \frac{1}{6}ml^2\left(4\dot{\theta}_1^2 + \dot{\theta}_2^2 + 3\dot{\theta}_1\dot{\theta}_2\cos\left(\theta_1 - \theta_2\right)\right) + \frac{1}{2}mgl\left(3\cos\theta_1 + \cos\theta_2\right).$$

Now, using the Euler-Lagrange Equation, we can express the momenta as

$$p_{\theta_1} = \frac{\partial L}{\partial \dot{\theta}_1} = \frac{1}{6} ml^2 \left(8\dot{\theta}_1 + 3\dot{\theta}_2 \left(\theta_1 - \theta_2\right)\right),$$
$$p_{\theta_2} = \frac{\partial L}{\partial \dot{\theta}_2} = \frac{1}{6} ml^2 \left(2\dot{\theta}_2 + 3\dot{\theta}_1 \left(\theta_1 - \theta_2\right)\right),$$

and subsequently invert them to get the equations for angles

$$\dot{\theta}_1 = \frac{6}{ml^2} \frac{2p_{\theta_1} - 3\cos\left(\theta_1 - \theta_2\right) p_{\theta_2}}{16 - 9\cos^2\left(\theta_1 - \theta_2\right)},$$
$$\dot{\theta}_2 = \frac{6}{ml^2} \frac{8p_{\theta_2} - 3\cos\left(\theta_1 - \theta_2\right) p_{\theta_1}}{16 - 9\cos^2\left(\theta_1 - \theta_2\right)}.$$

The remaining equations of motion are

$$\dot{p}_{\theta_1} = -\frac{1}{2} ml^2 \left(\dot{\theta}_1 \dot{\theta}_2 \sin\left(\theta_1 - \theta_2\right) + 3\frac{g}{l} \sin\theta_1\right)$$
$$\dot{p}_{\theta_2} = -\frac{1}{2} ml^2 \left(-\dot{\theta}_1 \dot{\theta}_2 \sin\left(\theta_1 - \theta_2\right) + \frac{g}{l} \sin\theta_1\right).$$

These last four equations fully describe the dynamics of the system. Unfortunately, the analytical integration of these equations is impossible, however, one can perform this integration numerically.

In what follows, we trace the position of the tip of the second rod for two initial conditions which differ only in the initial angle by 10^{-6} . As we can see in Figure

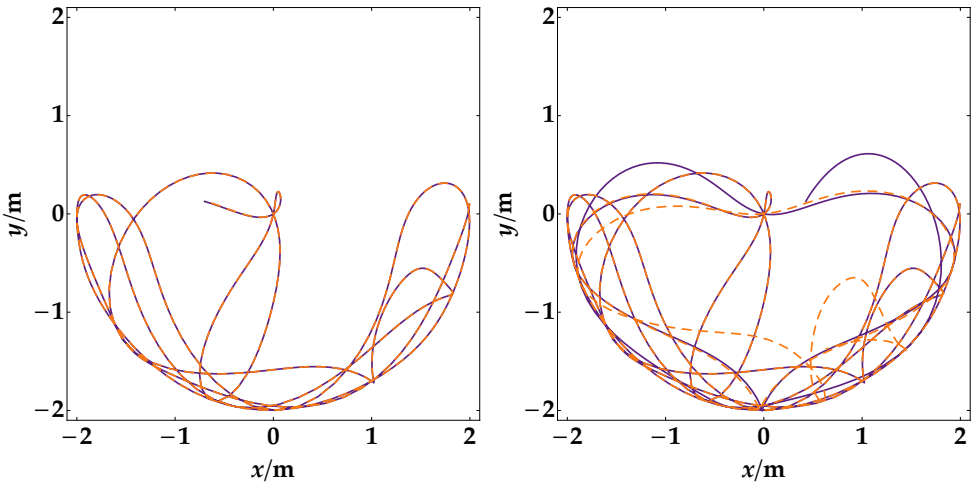

FIGURE 6.3: Two trajectories of the second rod's tip for two initial conditions that differ in the initial angle by 10^{-6}. The two frames are captured at times before and after the divergence of the trajectories, respectively.

6.3, the two trajectories follow the same path and at some point start to diverge. In a computer simulation, the chaotic systems are entirely predictable because we can set the initial conditions with arbitrary precision. However, in realistic simulations, where we first need to measure some quantities and subsequently insert them into a model, chaotic systems are predictable in the short run. This is because an ideally

exact measurement is impossible; therefore, the prediction time strongly depends on the accuracy of the measurement of the state of the system. In general, the amount of time that the behaviour of a chaotic system can be effectively predicted also depends on how much uncertainty can be tolerated in the forecast, and a time scale associated with dynamics of the system, called the Lyapunov time [264].

The Lyapunov time is defined as the inverse of a system's largest Lyapunov exponent. The number of Lyapunov exponents is equal to the dimensionality of the phase space. Usually, one uses the maximal Lyapunov exponent since it determines the general predictability of dynamical systems. A positive maximal Lyapunov exponent is associated with chaotic systems. The largest Lyapunov exponent is defined as [265]:

$$\lambda = \lim_{t\to\infty} \lim_{\delta \mathbf{Z}_0 \to \infty} \frac{1}{t} \ln \frac{|\delta \mathbf{Z}(t)|}{|\delta \mathbf{Z}_0|},$$

where $\delta \mathbf{Z}_0$ is the initial separation of trajectories, $\delta \mathbf{Z}(t)$ is the separation of trajectories at time t, and λ is the largest Lyapunov exponent. What has already been stated in the introduction to this Chapter, the uncertainty in chaotic systems increases exponentially with elapsed time. This means, in practice, that meaningful predictions can be made only over an interval of maximally two or three Lyapunov times; otherwise, the system appears random. However, instead of making meaningful predictions, it is also possible to use the characteristic exponential dependence on the initial conditions of chaotic systems to find the initial conditions with colossal accuracy.

Imagine now that we want to measure the initial state of the double rod pendulum with very high precision. To this end, we can perform an experiment with a double-rod pendulum in which we are able to prepare the initial state with some uncertainty and subsequently let the system evolve. By measuring the position of the second rod's tip in time (or the angles, for instance), it is possible to distinguish the trajectories, or the initial states, which initially were indistinguishable, similarly as in Figure 6.3, and thus reduce the uncertainty of the initial state. In an ideal situation, it would be possible to measure the initial condition with extreme accuracy in a relatively short time. In this sense, we can think of the chaotic dynamics as a magnifying glass that increases the resolution of our measurement in time. Of course, from the realistic viewpoint, the final uncertainty is limited by imperfections and noise, but the idea of exploiting chaos in precision measurements is extremely tempting.

As a matter of fact, it would be even more tempting to combine chaotic behaviour with entanglement and thus make chaos-enhanced quantum metrology. Unfortunately, the Schorödinger's equation, which governs the quantum realm, is linear with respect to the wavefunction and genuine chaos, in terms of exponential dependence on the initial conditions, is impossible. This can also be seen from the perspective of quantum Fisher information. The quantum Fisher information is calculated by optimising the classical Fisher information over all possible measurements. The mean value of an observable $\hat{M}$ in quantum mechanics is described as (for pure states)

$$\langle \psi | \hat{M} | \psi \rangle \equiv \langle \hat{M} \rangle .$$

Now imagine the following procedure. We prepare an initial state $|\psi\rangle$ and let it interact with some system that introduces a minute change to our state. We know the mechanism, but we do not know the strength of the interaction; therefore, assuming the transformations are restricted to rotations (see Equation 1.6), the initial state after

the interaction reads

$$|\psi(\phi)\rangle = e^{-i\phi\hat{J}_{\hat{n}}}|\psi\rangle\,,$$

where the direction $\hat{n}$ is known and the parameter ϕ is unknown. Subsequently, we let our system evolve according to some Hamiltonian. The resulting state is then

$$|\tilde{\psi}(\phi)\rangle = e^{-i\hat{H}t/\hbar}|\psi(\phi)\rangle = e^{-i\hat{H}t/\hbar}e^{-i\phi\hat{J}_{\hat{n}}}|\psi\rangle\,.$$

Now, we are performing an arbitrary measurement $\hat{M}$ and want to estimate the value of ϕ with the highest possible sensitivity. It is not obvious what kind of measurement we should choose, so let us first look at the ultimate bound given by the quantum Fisher information. As it has been already stated, the quantum Fisher information is optimised over all possible measurements. Then, we have

$$\begin{aligned}\langle\hat{M}\rangle &= \langle\tilde{\psi}(\phi)|\hat{M}|\tilde{\psi}(\phi)\rangle = \langle\psi(\phi)|e^{i\hat{H}t/\hbar}\hat{M}e^{-i\hat{H}t/\hbar}|\psi(\phi)\rangle \\ &= \langle\psi(\phi)|\hat{M}'|\psi(\phi)\rangle\,.\end{aligned}$$

In other words, the evolution governed by a Hamiltonian describing a closed system changes only the observable, and, as a consequence, the measurement we need to perform on the state $|\psi(\phi)\rangle$. Moreover, since the quantum Fisher information is related to the distance between neighbouring quantum states, it means that for unitary transformations, there cannot be exponential dependence on initial conditions. Therefore, chaos (with respect to the exponential sensitivity to the initial conditions) does not exist in genuine quantum systems, i.e., those whose evolution is governed by the Schrödinger equation (or the Heisenberg equation of motion). Any subsequent evolution after the change of the initial state cannot help to further distinguish the final state from the initial one. Therefore, for initially uncorrelated states, the maximal precision is bounded by the linear interferometry shot-noise limit, which can be overcome with the use of entangled states only. Notwithstanding, this result shows us what kind of transformations can be still useful in metrology.

The lack of chaotic trajectories in quantum mechanics is a great challenge for the quantum-classical correspondence [266] and has motivated a search for the so-called quantum signatures of chaos [267, 268]. If a quantum system exhibits signatures of chaos, it means that in the classical limit, the system will exhibit chaotic behaviour. The most renowned examples of signatures of quantum chaos include spectral properties of the generating Hamiltonian [269], phase-space scarring [270], fidelity decay [271], and most importantly entanglement [272].

Very recently, the chaotic behaviour was studied in the framework of quantum metrology. In Reference [273], the authors investigate how a quantum kicked top can be used in magnetometry. Although the authors show the gain over the shot noise limit, it is not clear whether the gain has really chaotic origins or it is merely because of the entanglement generation.

In the next Sections, we show how the quantum Fisher information analysis of the dynamics of the Dicke model [274] can be used to study quantum chaos.

6.2 The Dicke model

The Dicke model is easy to describe theoretically. It describes a system composed of N atoms which collectively interact with a single mode of light. The essence of this

cooperative behaviour is that the atomic dipoles interact coherently with the privileged radiation mode. In recent years, the Dicke model has renewed interest because of its superradiant phase transition [275, 276] and because it is a simple model in which one can find multi-partite entanglement, squeezing, classical as well as quantum chaos [277–279], and it is an exactly solvable quantum system [280]. Above all, the Dicke model can be realised in systems more widely than in the original cavity quantum electrodynamics case [281]. Furthermore, it was an early investigation of something analogous to a laser-like behaviour, superradiance, from a time well before the laser [282].

The Hamiltonian of the Dicke model can be written as

$$\hat{H} = \hbar\Big\{\omega_0 \hat{J}_z + \omega\, \hat{a}^\dagger \hat{a} + g\sqrt{\frac{1}{N}}\left(\hat{a} + \hat{a}^\dagger\right)\hat{J}_x\Big\}.$$

The first term describes spin precession about the z axis with frequency ω_0, and the second term describes harmonic oscillation with frequency ω. The last term is the interaction term and can be viewed as a spin precession about the x axis with a 'frequency' $\propto \hat{a} + \hat{a}^\dagger$ and as driving of the oscillator by a 'force' $\propto \hat{J}_x$. The coupling g is the Rabi frequency. In standard quantum optics approach, the Dicke Hamiltonian is usually considered in the rotating-wave approximation, which is valid for small values of coupling. This simplifies the analysis of the Dicke Hamiltonian, but at the same time removes the possibility of quantum chaos [278].

Although there are many works devoted to the Dicke model, the emergence of chaos as the energy and coupling are varied is still an open question, as well as the relative status between the superradiant phase transition and the crossover from regular to chaotic behaviour [283].

Quantum phase transitions are usually connected with the critical behaviour of certain features, for example, entanglement or non-classicality. In Reference [284], quantum Fisher analysis was used in the Dicke model to study the transition from the so-called normal phase to the superradiant phase. The authors numerically generated the ground state of the Dicke model as a function of coupling and calculated the quantum Fisher information subsequently for reduced density matrices of atoms and photons. Although using reduced density matrices can destroy entanglement and may lead to the loss of some information, quantum Fisher information shows critical behaviour around the critical point, especially as the system approaches the thermodynamic limit.

In the next Section, we show how quantum Fisher information can be used to characterise the transition from integrable to chaotic dynamics. Integrability means that the number of system's constants of motion is equal to the number of its degrees of freedom and implies that a small change of initial state results in small change of the final state. As a matter of fact, integrable and chaotic systems are two limiting cases of dynamics' stability and typically systems exhibit mixed dynamics meaning that the phase space has coexisting regions of integrable or chaotic motions.

6.3 Chaos metrology

Apart from metrological applications, quantum Fisher information can also be applied to characterise the time-scales of the Dicke model and physical systems whatsoever and thus the transition between classical and chaotic dynamics since these time-scales depend on the character of dynamics. First is the Ehrenfest time, which is the timescale at which the correspondence between quantum and classical dynamics

breaks down [285]. Quantum Fisher information can sense the Ehrenfest time since the breakdown of the correspondence coincides with the build-up of entanglement and non-classicality. In other words, a system stops to behave classically as soon as the system's state becomes non-classical. Second time-scale which can be studied with the help of the quantum Fisher information is the Heisenberg time. This longer time-scale is associated with the fact that after some time the system reaches the boundary of the Hilbert space and effectively begins to behave as an integrable system [286]. The finiteness of the Hilbert space also affects the maximal amount of entanglement, which can be quantified with quantum Fisher information. Similarly, as in Reference [283], we fix the energy of the initial state with respect to the ground state and look at dynamics from the perspective of quantum Fisher information.

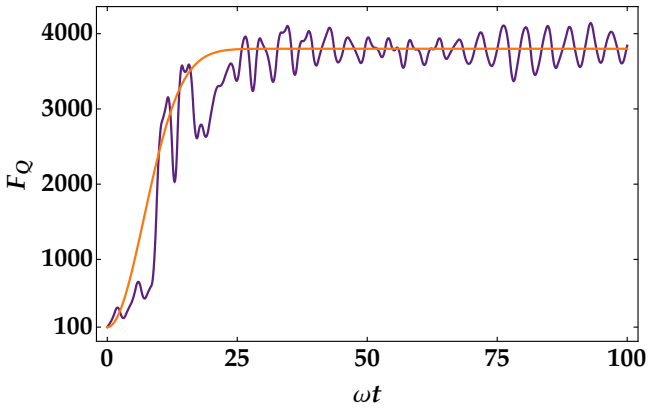

FIGURE 6.4: Optimised quantum Fisher information for the Dicke model as a function of rescaled time. Here $\omega = \omega_0 = 1$ and $g = 0.6\omega$. The violet curve is the original data and the orange curve is the approximation given by Equation 6.3.

In order to examine the dynamics of the Dicke model with the help of quantum Fisher information, we consider a system with 100 atoms and coupling g ranging from 0.1 to 1.0 (units of ω hereinafter). For each coupling, we start the dynamics with a classical state consisting of a coherent spin state (atoms) and a coherent field state. The coherent spin state is polarised along the $-z$ axis (minimal energy for a classical state), and the amplitude of the field coherent state is chosen in such a way that the energy E of the resulting state satisfies

$$\frac{E - E_{\text{gs}}}{E_{\text{gs}}} \approx 0.527,$$

where E_{gs} is the energy of the ground state. The Energy and the parameters of the simulation are chosen in a way allowing for observation of the onset of the chaotic behaviour in the vicinity of the superradiant phase transition. Since the field Fock space is infinite, we have to cut it in an appropriate place. This is done by increasing the photonic cutoff up to a point at which the amplitude of the last coefficient is negligible. For smaller energies, the onset of the chaotic behaviour is expected to occur for couplings $g > 1$ which greatly increases the mean number of photons and thus greatly increasing the effective dimension of the Hilbert space, preventing a reliable simulation. On the other hand, for larger energies, the chaotic onset is expected to occur below the critical coupling.

The trajectories of the states $|\psi(t)\rangle$ are subsequently used to calculate maximal quantum Fisher information (without tracing out the photonic degrees of freedom) by finding the eigenvalues of the γ_C matrix (see Equation 3.5 in Section 3.5) at each t:

$$4\begin{pmatrix} \Delta^2\hat{J}_x & \langle\{\hat{J}_x,\hat{J}_y\}\rangle/2-\langle\hat{J}_x\rangle\langle\hat{J}_y\rangle & \langle\{\hat{J}_x,\hat{J}_z\}\rangle/2-\langle\hat{J}_x\rangle\langle\hat{J}_z\rangle \\ \langle\{\hat{J}_y,\hat{J}_x\}\rangle/2-\langle\hat{J}_y\rangle\langle\hat{J}_x\rangle & \Delta^2\hat{J}_y & \langle\{\hat{J}_y,\hat{J}_z\}\rangle/2-\langle\hat{J}_y\rangle\langle\hat{J}_z\rangle \\ \langle\{\hat{J}_z,\hat{J}_x\}\rangle/2-\langle\hat{J}_z\rangle\langle\hat{J}_x\rangle & \langle\{\hat{J}_z,\hat{J}_y\}\rangle/2-\langle\hat{J}_z\rangle\langle\hat{J}_y\rangle & \Delta^2\hat{J}_z \end{pmatrix},$$

where $\{\bullet,\bullet\}$ stands for the anticommutator. According to this procedure, the minimal and the maximal value of the quantum Fisher information is N and N^2, respectively. A typical result of this procedure can be seen in Figure 6.4. The quantum Fisher information starts from the atomic shot-noise because the simulation was initialised with a classical state. Subsequently, although there is no term in the Hamiltonian corresponding to the interaction among the atoms, they start to entangle. The entanglement among the atoms arises because they effectively interact via the light mode. After the initial slow growth, quantum Fisher information increases quickly up to a point when it reaches a quasi-stationary value (see oscillations in Figure 6.4). We call the entanglement build-up time the time after which the quantum Fisher information saturates. The entanglement build-up time is bound from below by the Ehrenfest time and from above by the Heisenberg time.

To ensure ourselves that we are dealing with chaotic or regular dynamics, we calculate the Wigner function and examine whether it possesses scars [270] which are signatures of quantum chaos (see Figure 6.5).

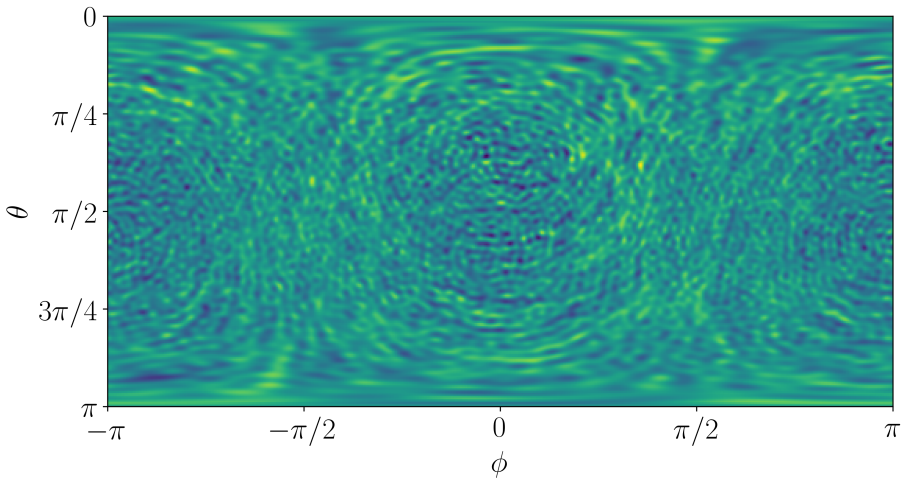

FIGURE 6.5: The phase-space scarring [270] is a signature of quantum chaos. The figure presents the Mercator projection of the SU(2) Wigner function of a chaotic state generated with the Dicke Hamiltonian.

In order to get the characteristic features of the quantum Fisher information, we approximate it we the following function:

$$F_Q = \mathrm{SN} + A\left(1-\exp\left(-(x/t_s)^2\right)\right),$$

where SN stands for the atomic shot-noise (here 100), A is the asymptotic value of quantum Fisher information and t_s is the entanglement build-up time.

Figure 6.6 shows the asymptotic value of quantum Fisher information and the entanglement build-up time as a function of coupling g. The asymptotic value of the

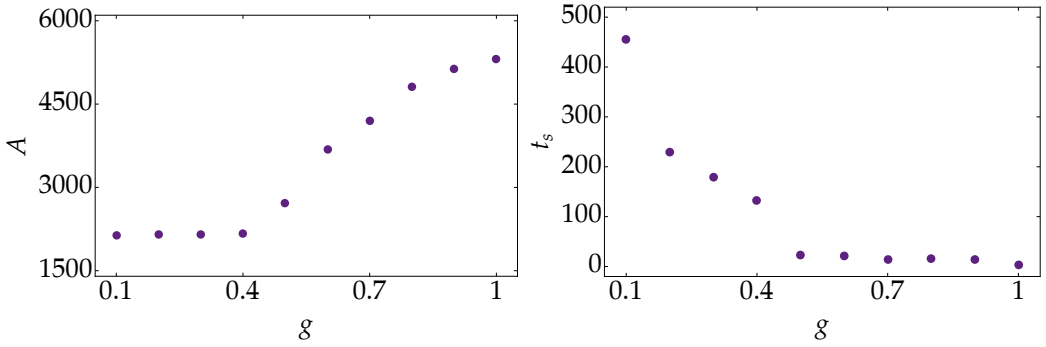

FIGURE 6.6: Parameters A and t_s as a function of g taken from the fit to the dynamics of quantum Fisher information, see Equation 6.3.

quantum Fisher information for small g does not depend on the value of g because the system is integrable. The onset of chaos begins around $g = 0.4$ where Fisher information starts to grow until it saturates around $g = 1$. The saturation of the asymptotic value of quantum Fisher information occurs because the system starts to feel finiteness of the Hilbert space. In other words, the fine structures responsible for the large value of the Fisher information are limited by the size of the Hilbert space. If we look at the entanglement build-up time t_s on the other hand, we see that it decreases quickly below $g = 0.5$ and afterwards it is constant. The minimal value of the entanglement build-up time is limited by the Ehrenfest time which for integrable dynamics behaves as [283]

$$t_{\mathrm{E}} \sim \sqrt{j}$$

and for chaotic dynamics behaves as [283]

$$t_{\mathrm{E}} \sim \frac{1}{2\lambda} \ln j,$$

where $j = N/2$ and λ is the Lyapunov time. In order to study the Ehrenfest time, we generated trajectories by fixing the coupling to 0.9 and the energy of the initial state, as in Equation 6.3, and a various number of atoms from $N = 20$ to $N = 90$. Subsequently, the Ehrenfest time is identified as the moment when optimised quantum Fisher information exhibits the first kink. This seemingly arbitrary identification is justified by the fact that when the correspondence between classical and quantum dynamics breaks down, the state is no longer classical which affects the behaviour of the quantum Fisher information. In Figure 6.7, we show the position of the first kink of the Fisher information as a function of $\ln N$.

An interesting question that may be answered with the help of the quantum Fisher information is what happens with the Ehrenfest time for mixed dynamics where some parts of the phase space are integrable and others are chaotic. The Ehrenfest time is a quantity that is well defined for systems that are non-chaotic or chaotic (see Equations 6.3 and 6.3). However, there is no theory which tells what happens with the Ehrenfest time when crossing from integrable to chaotic dynamics.

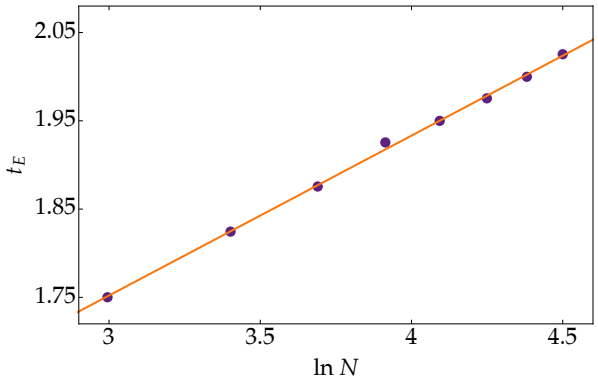

FIGURE 6.7: The Ehrenfest time as seen by the quantum Fisher information as a function of $\ln N$. The dots are the values from the simulation, and the orange curve is a logarithmic fit.

Although the quantum Fisher information analysis cannot strictly say how qualitatively Ehrenfest time changes along this transition, it can show how it changes quantitively between $\sqrt{j}$ and $\ln j$ scaling. To examine the characteristic scaling with j, we pick two values of the coupling strength g, one corresponding to integrable dynamics and one corresponding to chaotic dynamics, and subsequently run a simulation for the number of particles ranging from 30 to 100. The results are presented in Figure 6.8.

By normalising the optimised quantum Fisher information, we can clearly see the transition from shot-noise to Heisenberg scaling. Interestingly, the transition is sharp ($\ln j$ scaling) for chaotic dynamics and smooth ($\sqrt{j}$ scaling) for regular dynamics. A similar type of analysis may also show when and under which conditions the Lyapunov exponent enters the definition of the Ehrenfest time. Also, as it has been stated in the first paragraph of this Section, quantum Fisher information can be used to study the Heisenberg time [273]. We defer, however, this investigation to future work.

In conclusion to this Chapter, we want to stress that although quantum metrology cannot be enhanced by diverging quantum trajectories, its methods are still advantageous to study chaotic properties of dynamical systems. As a consequence, quantum Fisher information finds its new applications besides metrology and studying phase transitions. This new application is possible because Fisher information is a tool that measures the susceptibility of a system to a change. On top of that, Fisher information can also be used to study the relationship between entanglement and chaos.

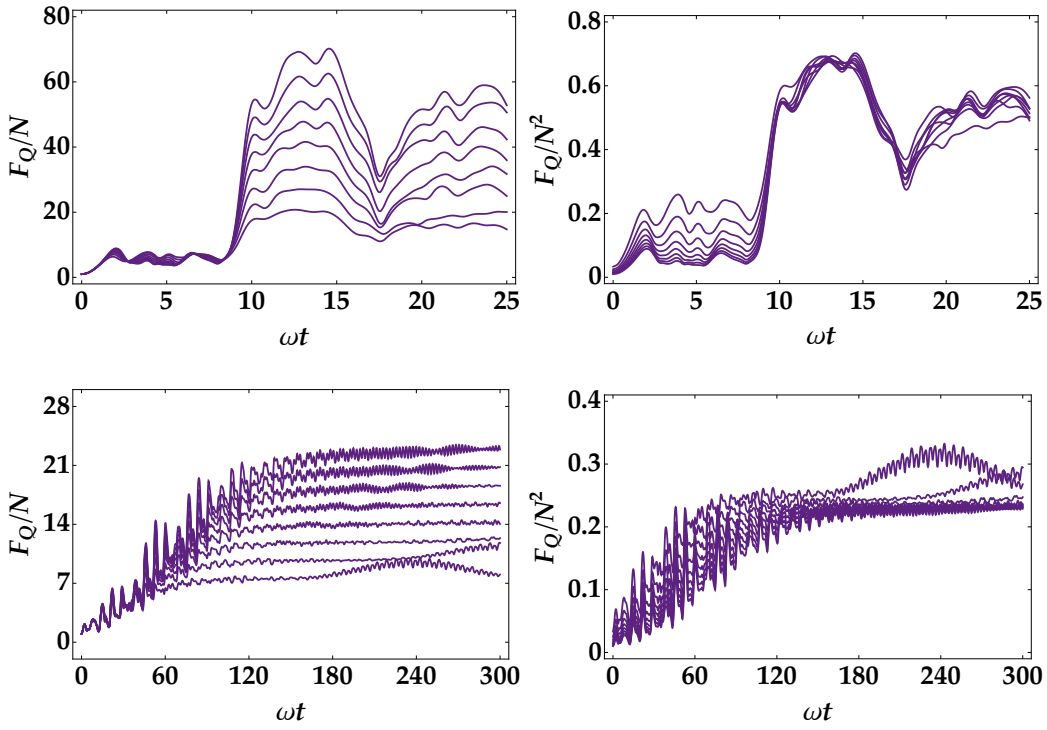

FIGURE 6.8: Optimised quantum Fisher information for $g = 0.9$ (top row) and $g = 0.4$ (bottom row) normalised to shot-noise limit (left column) and Heisenberg limit (right column). The transition from shot-noise scaling to Heisenberg scaling is abrupt for chaotic dynamics ($g = 0.9$) but smooth for regular dynamics ($g = 0.4$). Here N ranges from 30 to 100.

Chapter 7

Conclusions

This dissertation was devoted to the use of quantum effects and phenomena in precision measurements, a field known as quantum metrology. These non-classical properties were created in a system composed of atoms in a Bose-Einstein condensate, a system composed of light confined in an optical cavity which interacts with a single atom, and in a hybrid system where atoms in a Bose-Einstein condensate interact with a single mode of light in an optical cavity.

The first quantum property we studied was entanglement between the atoms in a Bose-Einstein condensate, which can be exploited to break the classical precision limit of measurement, even if one cannot fully control the creation of entanglement and detection of atoms. The second quantum property that we studied was the non-classicality of the light prepared by a quantum non-demolition measurement. We show that using this type of non-classical light in a Mach-Zehnder interferometer can yield an extremely entangled state of two modes of light which again gives rise to the sub-shot-noise precision. The last metrological scheme, although only loosely related to precision measurements, may lead to the development of new sensors exploiting chaotic features of physical systems. Moreover, this type of analysis opens a new perspective on studying quantum chaos in general.

Quantum metrology promises high-precision measurements of physical parameters with far-reaching implications for science and technology, as it has been shown in this dissertation and many other theoretical and experimental investigations. The most promising effect that was predicted to increase the precision and that was studied in a vast amount of works is quantum entanglement since, potentially, it can give rise to the Heisenberg scaling of the precision. So far, however, the classical limit of precision has been beaten only in a few experiments, and only for relatively small samples, as the required non-classical states are challenging to prepare and stabilise. It seems that a serious enemy of entanglement-based quantum metrology is decoherence which efficiently prevents from switching from the proof-of-principle experiments to real life applications. Another factor limiting the entanglement-based quantum metrology is the problem of imperfect detectors. The highly entangled states require ideal detectors, otherwise, all the information encrypted in these fragile states is lost. Therefore, imperfect detectors limit the amount of entanglement in the initial states and thus the final sensitivity of a measuring device.

Quantum entanglement is one of the most interesting phenomena with potential applications in many fields but is of course not the only effect that can increase the precision of a measurement. For example, ideas of replacing entangled initial states by dynamics were proposed in References [273, 287], but, as a matter of fact, the dynamics are itself often introducing entanglement into the system, so one could say that effectively this is still an entanglement-based enhancement. An interesting metrological scheme not exploiting entanglement but the quantum coherence of a single artificial atom was recently described in Reference [288]. The authors

implemented two-phase estimation algorithms (Kitaev [289] and the semiclassical Fourier-transform [290] algorithms) using an artificial atom realised with a superconducting transmon circuit and demonstrated flux sensitivity exceeding the classical shot-noise limit of the device. This very interesting protocol is based on the fact that the unknown parameter (denoted by λ) defines the energy states $E_n(\lambda)$ of the quantum probe system. The unknown parameter λ can be estimated from the phase $\phi = \Delta E(\lambda)\tau/\hbar$ accumulated by the system in the course of its evolution during the time τ. Then, the ultimate precision is constrained by the Heisenberg relation $\Delta E(\lambda) \geq 2\pi\hbar/t$ which sets the fundamental limit to $\delta\lambda \propto 1/t$ achievable with the help of the phase estimation algorithms for times of the order of probe's coherence time $t \sim T_2$.

Very recently, a single-atom transistor was proposed as a precise magnetic field sensor [291, 292]. Typically, the collisional properties of atoms are tuned with the help of external magnetic fields (Feshbach resonances); however, the collisions can be treated as a probe of the magnetic field itself. In the described scheme, the atoms were colliding with impurities in waveguides generated by an optical lattice. Since the external magnetic field strongly affects the collisional properties of atoms, it is possible to extract the information about the field by measuring the transmission of atoms through the waveguides. Interestingly, this robust against experimental imperfections sensor was not based on the preparation of many-body entangled states.

Another example of a metrological system which is not based on entanglement is a supersolid, which simultaneously exhibits contrasting and seemingly irreconcilable superfluid and crystalline orders. In a naïve picture, a supersolid can be viewed as a solid capable of a dissipationless flow. In a recent theoretical investigation, a supersolid state of matter was studied in a ring cavity with a Bose-Einstein condensate within [293]. In this system, losses of photons, typically introducing decoherence, do not destroy the supersolidity and, what is more, allow for monitoring the relative phase between the cavity modes which enables one to non-destructively follow the displacement of the Bose-Einstein condensate in real time. Therefore, it could be used as a free-falling zero temperature mass for gravitational acceleration measurements.

We also have shown that quantum Fisher information can find its application in studying quantum chaos. One can identify characteristic time-scales or even phase transitions of physical systems by calculating the optimised quantum Fisher information as a function of time. This is possible because it has been shown that the chaotic behaviour manifests itself in the process of entanglement [273, 294]. Moreover, this opens the possibility to study the relation between classical and quantum chaos from an entirely new perspective.

Finally, it seems that the common mindset in the field of quantum metrology is the hunt for sub-shot-noise scaling or ultimately for the Heisenberg scaling. However, measuring devices are not characterised by the scaling of the sensitivity but by their effective performance. For instance, it is sometimes argued that when the sensitivity is

$$\Delta\theta = \alpha N^d,$$

the factor α is irrelevant because the improvement granted by α is negligible compared to that granted by sufficiently large N [295]. Such a statement is only true under the assumption that N can be an arbitrarily large number. As a matter of fact, the sub-shot-noise scaling is currently only possible for relatively small sample sizes N, because for larger samples the effect of decoherence and limitations arising from

noise prohibit the exploitation of entanglement and thus the sub-shot-noise scaling of the sensitivity, as has been shown in this dissertation and other works.

In short, the conclusions of this work are critical for entanglement-based quantum metrology but not for quantum metrology itself. Entanglement, while potentially extremely attractive from a theoretical point of view, is too fragile in practical metrological applications. As a consequence, the future of quantum metrology may lie in the hands of phenomena not necessarily exploiting or involving quantum entanglement. Moreover, quantum metrology without entanglement may find its new applications in describing various kinds of quantum phase transitions or the estimation of thermodynamic parameters and also parameters characterising non-equilibrium states [295]. For quantum-metrology, besides entanglement, there is still plenty of room in the quantum.

Bibliography

1. V. Giovannetti, S. Lloyd, L. Maccone, *Physical Review Letters* **96**, 010401 (2006).
2. S. L. Braunstein, C. M. Caves, *Physical Review Letters* **72**, 3439–3443 (22 1994).
3. L. Pezzé, A. Smerzi, *Physical Review Letters* **102**, 100401 (10 2009).
4. P. Kok, S. L. Braunstein, J. P. Dowling, *Journal of Optics B: Quantum and Semiclassical Optics* **6**, S811 (2004).
5. A. A. Michelson, E. W. Morley, *Sidereal Messenger, vol. 6, pp. 306-310* **6**, 306–310 (1887).
6. L. Zehnder, *Zeitschrift für Instrumentenkunde* **11**, 275–285 (1891).
7. L. Mach, *Zeitschrift für Instrumentenkunde* **12**, 89–93 (1892).
8. T. Berrada *et al.*, *Nature Communications* **4** (2013).
9. M. G. A. Paris, *Physical Review A* **59**, 1615–1621 (2 1999).
10. G. Haack, H. Förster, M. Büttiker, *Physical Review B* **82**, 155303 (15 2010).
11. A. Einstein, *Prussian Academy of Sciences* **1**, 668–696 (1916).
12. B. P. Abbott et al., *Physical Review Letters* **116**, 061102 (6 2016).
13. M. Inguscio, L. Fallani, *Atomic Physics: Precise Measurements and Ultracold Matter* (Oxford University Press, 2013).
14. A. Peters, K. Y. Chung, S. Chu, *Nature* **400**, 849–852 (1999).
15. T. L. Gustavson, P. Bouyer, M. A. Kasevich, *Physical Review Letters* **78**, 2046–2049 (11 1997).
16. C. R. Ekstrom, J. Schmiedmayer, M. S. Chapman, T. D. Hammond, D. E. Pritchard, *Physical Review A* **51**, 3883–3888 (5 1995).
17. J. B. Fixler, G. T. Foster, J. M. McGuirk, M. A. Kasevich, *Science* **315**, 74–77, ISSN: 0036-8075 (2007).
18. N. Ramsey, *Molecular Beams* (Oxford University Press, 1956), vol. 20.
19. S. A. Diddams, J. C. Bergquist, S. R. Jefferts, C. W. Oates, *Science* **306**, 1318–1324, ISSN: 0036-8075 (2004).
20. R. Lynch, *Physics Reports* **256**, 367–436 (1995).
21. W. H. Zurek, presented at the Quantum Gravity And Cosmology-Proceedings Of The Xxii Gift International Seminar On Theoretical Physics, p. 117.
22. C. M. Caves, *Physical Review D* **23**, 1693–1708 (8 1981).
23. B Yurke, *Physical Review Letters* **56**, 1515 (1986).
24. M. Holland, K Burnett, *Physical Review Letters* **71**, 1355 (1993).
25. B. Sanders, G. Milburn, *Physical Review Letters* **75**, 2944 (1995).
26. J. Bollinger, W. M. Itano, D. Wineland, D. Heinzen, *Physical Review A* **54**, R4649 (1996).

27. L. Pezzé, A. Smerzi, *Physical Review Letters* **100**, 073601 (2008).
28. D. Wineland, J. Bollinger, W. Itano, D. Heinzen, *Physical Review A* **50**, 67 (1994).
29. A Sørensen, L.-M. Duan, J. Cirac, P. Zoller, *Nature* **409**, 63–66 (2001).
30. G. D'Ariano, P. L. Presti, *Physical Review Letters* **86**, 4195 (2001).
31. P. Hyllus *et al.*, *Physical Review A* **85**, 022321 (2012).
32. G. Tóth, *Physical Review A* **85**, 022322 (2012).
33. V. Giovannetti, S. Lloyd, L. Maccone, *Nature Photonics* **5**, 222–229 (2011).
34. P. Walther *et al.*, *Nature* **429**, 158–161 (2004).
35. M. W. Mitchell, J. S. Lundeen, A. M. Steinberg, *Nature* **429**, 161–164 (2004).
36. T. Nagata, R. Okamoto, J. L. O'brien, K. Sasaki, S. Takeuchi, *Science* **316**, 726–729 (2007).
37. K. Goda *et al.*, *Nature Physics* **4**, 472–476 (2008).
38. D Leibfried *et al.*, *Science* **304**, 1476–1478 (2004).
39. C. Roos, M Chwalla, K Kim, M Riebe, R Blatt, *Nature* **443**, 316–319 (2006).
40. J Hald, J. Sørensen, C. Schori, E. Polzik, *Physical Review Letters* **83**, 1319 (1999).
41. W. Wasilewski *et al.*, *Physical Review Letters* **104**, 133601 (2010).
42. R. Sewell *et al.*, *Physical Review Letters* **109**, 253605 (2012).
43. C. Orzel, A. Tuchman, M. Fenselau, M Yasuda, M. Kasevich, *Science* **291**, 2386–2389 (2001).
44. J Esteve, C Gross, A Weller, S Giovanazzi, M. Oberthaler, *Nature* **455**, 1216–1219 (2008).
45. M. F. Riedel *et al.*, *Nature* **464**, 1170–1173 (2010).
46. J. Cirac, M Lewenstein, K Mølmer, P Zoller, *Physical Review A* **57**, 1208 (1998).
47. L.-M. Duan, A Sørensen, J. Cirac, P Zoller, *Physical Review Letters* **85**, 3991 (2000).
48. A. Micheli, D Jaksch, J. I. Cirac, P Zoller, *Physical Review A* **67**, 013607 (2003).
49. C. D. Hamley, C. Gerving, T. Hoang, E. Bookjans, M. S. Chapman, *Nature Physics* **8**, 305–308 (2012).
50. Y. Castin, in *Coherent Atomic Matter Waves* (Springer, 2001), pp. 1–136.
51. A. S. Sørensen, K. Mølmer, *Physical Review Letters* **86**, 4431 (2001).
52. S Inouye *et al.*, *Nature* **392**, 151–154 (1998).
53. D. Petrov, D. Gangardt, G. Shlyapnikov, presented at the Journal de Physique IV (Proceedings), vol. 116, pp. 5–44.
54. C. Gross, T. Zibold, E. Nicklas, J. Esteve, M. K. Oberthaler, *Nature* **464**, 1165–1169 (2010).
55. C. F. Ockeloen, R. Schmied, M. F. Riedel, P. Treutlein, *Physical Review Letters* **111**, 143001 (2013).
56. W. Müssel, H Strobel, D Linnemann, D. Hume, M. Oberthaler, *Physical Review Letters* **113**, 103004 (2014).
57. H. Strobel *et al.*, *Science* **345**, 424–427 (2014).
58. B. Lücke *et al.*, *Science* **334**, 773–776 (2011).

59. I. D. Leroux, M. H. Schleier-Smith, V. Vuletić, *Physical Review Letters* **104**, 073602 (2010).
60. J. Appel *et al.*, *Proceedings of the National Academy of Sciences* **106**, 10960–10965 (2009).
61. J. G. Bohnet *et al.*, *Nature Photonics* **8**, 731–736 (2014).
62. G.-Y. Xiang, B. L. Higgins, D. Berry, H. M. Wiseman, G. Pryde, *Nature Photonics* **5**, 43–47 (2011).
63. R. Krischek *et al.*, *Physical Review Letters* **107**, 080504 (2011).
64. M Kacprowicz, R Demkowicz-Dobrzański, W Wasilewski, K Banaszek, I. Walmsley, *Nature Photonics* **4**, 357–360 (2010).
65. I. Afek, O. Ambar, Y. Silberberg, *Science* **328**, 879–881 (2010).
66. M. Jachura, R. Chrapkiewicz, R. Demkowicz-Dobrzański, W. Wasilewski, K. Banaszek, *Nature Communications* **7** (2016).
67. B. Escher, R. de Matos Filho, L Davidovich, *Nature Physics* **7**, 406–411 (2011).
68. R. Demkowicz-Dobrzański, J. Kołodyński, M. Guţă, *Nature Communications* **3**, 1063 EP – (Sept. 2012).
69. J. F. Haase, A. Smirne, J. Kołodyński, R. Demkowicz-Dobrzański, S. F. Huelga, *New Journal of Physics* **20**, 053009 (2018).
70. M. Planck, *Annalen der Physik* **309**, 553–563, ISSN: 1521-3889 (1901).
71. T. S. Kuhn, *Black-body theory and the quantum discontinuity, 1894-1912* (University of Chicago Press, 1987).
72. A. Einstein, *Annalen der physik* **322**, 132–148 (1905).
73. T. H. Maiman, *Nature* **187**, 493–494 (1960).
74. E. C. G. Sudarshan, *Physical Review Letters* **10**, 277–279 (7 1963).
75. R. J. Glauber, *Physical Review* **131**, 2766–2788 (6 1963).
76. R. J. Glauber, *Physical Review* **130**, 2529–2539 (6 1963).
77. L. MANDEL, E. WOLF, *Rev. Mod. Phys.* **37**, 231–287 (2 1965).
78. H. J. Kimble, M. Dagenais, L. Mandel, *Physical Review Letters* **39**, 691 (1977).
79. R. Loudon, P. L. Knight, *Journal of Modern Optics* **34**, 709–759 (1987).
80. E. Schrödinger, *Naturwissenschaften* **14**, 664–666 (1926).
81. F. Hausdorff, *Ber. Verh. Kgl. SÃd' chs. Ges. Wiss. Leipzig., Math.-phys. Kl.* **58**, 19–48 (1906).
82. M. O. Scully, M. S. Zubairy, *Quantum optics*, 1999.
83. K. Husimi, *Proceedings of the Physico-Mathematical Society of Japan. 3rd Series* **22**, 264–314 (1940).
84. A Mann, M Revzen, *Physics Letters A* **134**, 273–275 (1989).
85. K. Takahashi, N. Saitô, *Physical Review Letters* **55**, 645 (1985).
86. P Leboeuf, A. Voros, *Journal of Physics A: Mathematical and General* **23**, 1765 (1990).
87. P Leboeuf, J Kurchan, M Feingold, D. Arovas, *Physical Review Letters* **65**, 3076 (1990).
88. E. Wigner, *Physical Review* **40**, 749 (1932).

89. C. Weedbrook *et al.*, *Reviews of Modern Physics* **84**, 621 (2012).
90. N Sonine, *Mathematische Annalen* **16**, 1–80 (1880).
91. K Vogel, H Risken, *Physical Review A* **40**, 2847 (1989).
92. D. Smithey, M Beck, M. G. Raymer, A Faridani, *Physical Review Letters* **70**, 1244 (1993).
93. K Banaszek, C Radzewicz, K Wódkiewicz, J. Krasiński, *Physical Review A* **60**, 674 (1999).
94. E. Lu, *Lettere al Nuovo Cimento (1971-1985)* **2**, 1241–1244 (1971).
95. H. P. Yuen, *Physical Review A* **13**, 2226 (1976).
96. H Takahasi, *Advances in Communication Systems* **1**, 7 (1965).
97. R. Slusher, L. Hollberg, B. Yurke, J. Mertz, J. Valley, *Physical Review Letters* **55**, 2409 (1985).
98. P Carruthers, M. Nieto, *Physical Review Letters* **14**, 387 (1965).
99. L. Mandel, *Optics Letters* **4**, 205–207 (1979).
100. L.-A. Wu, H. Kimble, J. Hall, H. Wu, *Physical Review Letters* **57**, 2520 (1986).
101. P. S. Laplace, *Théorie analytique des probabilités* (Courcier, 1820).
102. R. L. Hudson, *Reports on Mathematical Physics* **6**, 249–252 (1974).
103. R Short, L Mandel, *Physical Review Letters* **51**, 384 (1983).
104. F. Hong-Yi, F. Yue, *Physical Review A* **54**, 958 (1996).
105. C. Hong, L Mandel, *Physical Review Letters* **54**, 323 (1985).
106. T. Hirano, M. Matsuoka, *Optics Letters* **15**, 1153–1155 (1990).
107. L Mandel, *Physica scripta* **1986**, 34 (1986).
108. E. Schrödinger, presented at the Mathematical Proceedings of the Cambridge Philosophical Society, vol. 31, pp. 555–563.
109. J. D. Trimmer, *Proceedings of the American Philosophical Society*, 323–338 (1980).
110. W. H. Zurek, *Reviews of Modern Physics* **75**, 715 (2003).
111. V. Dodonov, I. Malkin, V. Man'Ko, *Physica* **72**, 597–615 (1974).
112. B. Yurke, D. Stoler, *Physical Review Letters* **57**, 13 (1986).
113. V. B. Braginsky, Y. I. Vorontsov, K. S. Thorne, *Science* **209**, 547–557 (1980).
114. M Brune, S Haroche, J. Raimond, L Davidovich, N Zagury, *Physical Review A* **45**, 5193 (1992).
115. K. Gheri, H Ritsch, *Physical Review A* **56**, 3187 (1997).
116. H. Ritsch, G. Milburn, T. Ralph, *Physical Review A* **70**, 033804 (2004).
117. B Wang, L.-M. Duan, *Physical Review A* **72**, 022320 (2005).
118. P. Hariharan, *Basiscs od Interferometry* (Academic Press, 2010).
119. B. Yurke, S. L. McCall, J. R. Klauder, *Physical Review A* **33**, 4033 (1986).
120. F. Bloch, *Physical Review* **70**, 460 (1946).
121. J. Schwinger, in *A Quantum Legacy: Seminal Papers of Julian Schwinger* (World Scientific, 1952), pp. 173–223.
122. I. Bloch, *Nature Physics* **1**, 23–30 (2005).

123. M. P. Fisher, P. B. Weichman, G Grinstein, D. S. Fisher, *Physical Review B* **40**, 546 (1989).

124. D. Jaksch, C. Bruder, J. I. Cirac, C. W. Gardiner, P. Zoller, *Physical Review Letters* **81**, 3108 (1998).

125. M. Greiner, O. Mandel, T. Esslinger, T. W. Hänsch, I. Bloch, *Nature* **415**, 39–44 (2002).

126. C. Orzel, A. Tuchman, M. Fenselau, M Yasuda, M. Kasevich, *Science* **291**, 2386–2389 (2001).

127. M. Girardeau, *Journal of Mathematical Physics* **1**, 516–523 (1960).

128. B. Paredes *et al.*, *Nature* **429**, 277–281 (2004).

129. T. Kinoshita, T. Wenger, D. S. Weiss, *Science* **305**, 1125–1128 (2004).

130. B. DeMarco, D. S. Jin, *Science* **285**, 1703–1706 (1999).

131. A. G. Truscott, K. E. Strecker, W. I. McAlexander, G. B. Partridge, R. G. Hulet, *Science* **291**, 2570–2572 (2001).

132. C. Regal, M. Greiner, D. S. Jin, *Physical Review Letters* **92**, 040403 (2004).

133. C Chin *et al.*, *Science* **305**, 1128–1130 (2004).

134. M. W. Zwierlein, J. R. Abo-Shaeer, A. Schirotzek, C. H. Schunck, W. Ketterle, *Nature* **435**, 1047–1051 (2005).

135. T. Rom *et al.*, *Physical Review Letters* **93**, 073002 (2004).

136. R. P. Feynman, *Foundations of Physics* **16**, 507–531 (1986).

137. M. H. Anderson, J. R. Ensher, M. R. Matthews, C. E. Wieman, E. A. Cornell, *Science* **269**, 198–201, ISSN: 0036-8075 (1995).

138. C. C. Bradley, C. Sackett, J. Tollett, R. G. Hulet, *Physical Review Letters* **75**, 1687 (1995).

139. K. B. Davis *et al.*, *Physical Review Letters* **75**, 3969 (1995).

140. S. N. Bose, *Plancks gesetz und lichtquantenhypothese* (Springer, 1924).

141. A. Einstein, *Quantentheorie des einatomigen idealen Gases* (Akademie der Wissenshaften, in Kommission bei W. de Gruyter, 1924).

142. M. Andrews *et al.*, *Science* **275**, 637–641 (1997).

143. B. P. Anderson, M. A. Kasevich, *Science* **282**, 1686–1689 (1998).

144. L. Deng *et al.*, *Nature* **398**, 218–220 (1999).

145. S Inouye *et al.*, *Science* **285**, 571–574 (1999).

146. M. Kozuma *et al.*, *Science* **286**, 2309–2312 (1999).

147. S Inouye *et al.*, *Physical Review Letters* **85**, 4225 (2000).

148. M.-O. Mewes *et al.*, *Physical Review Letters* **78**, 582 (1997).

149. I. Bloch, T. W. Hänsch, T. Esslinger, *Physical Review Letters* **82**, 3008 (1999).

150. V. M. Pérez-García, H. Michinel, H. Herrero, *Physical Review A* **57**, 3837 (1998).

151. S. Burger *et al.*, *Physical Review Letters* **83**, 5198 (1999).

152. J Denschlag *et al.*, *Science* **287**, 97–101 (2000).

153. L Khaykovich *et al.*, *Science* **296**, 1290–1293 (2002).

154. M. R. Matthews *et al.*, *Physical Review Letters* **83**, 2498 (1999).

155. K. Madison, F Chevy, W Wohlleben, J. Dalibard, *Physical Review Letters* **84**, 806 (2000).

156. J. Abo-Shaeer, C Raman, J. Vogels, W. Ketterle, *Science* **292**, 476–479 (2001).

157. C. D. Hamley, C. Gerving, T. Hoang, E. Bookjans, M. S. Chapman, *Nature Physics* **8**, 305–308 (2012).

158. W. H. Zurek, U. Dorner, P. Zoller, *Physical Review Letters* **95**, 105701 (2005).

159. M. Albiez *et al.*, *Physical Review Letters* **95**, 010402 (2005).

160. B. D. Josephson, *Physics Letters* **1**, 251–253 (1962).

161. A. J. Leggett, *Reviews of Modern Physics* **73**, 307 (2001).

162. A. Smerzi, S. Fantoni, S. Giovanazzi, S. Shenoy, *Physical Review Letters* **79**, 4950 (1997).

163. J. Links, A. Foerster, A. P. Tonel, G. Santos, presented at the Annales Henri Poincaré, vol. 7, pp. 1591–1600.

164. A. S. Sørensen, K. Mølmer, *Physical Review Letters* **86**, 4431 (2001).

165. J. Radcliffe, *Journal of Physics A: General Physics* **4**, 313 (1971).

166. A. Altland, F. Haake, *Physical Review Letters* **108**, 073601 (2012).

167. R. H. Dicke, *Physical Review* **93**, 99 (1954).

168. T Holstein, H. Primakoff, *Physical Review* **58**, 1098 (1940).

169. Wikipedia contributors, *Bloch sphere — Wikipedia, The Free Encyclopedia*.

170. J. Radcliffe, *Journal of Physics A: General Physics* **4**, 313 (1971).

171. G. S. Agarwal, *Physical Review A* **24**, 2889 (1981).

172. A. R. Edmonds, "Angular momentum in quantum mechanics", tech. rep. (CERN, 1955).

173. J. Ma, X. Wang, C.-P. Sun, F. Nori, *Physics Reports* **509**, 89–165 (2011).

174. M. Kitagawa, M. Ueda, *Physical Review A* **47**, 5138 (1993).

175. X. Wang, B. C. Sanders, *Physical Review A* **68**, 012101 (2003).

176. D. Ulam-Orgikh, M. Kitagawa, *Physical Review A* **64**, 052106 (2001).

177. D. J. Wineland, J. J. Bollinger, W. M. Itano, D. Heinzen, *Physical Review A* **50**, 67 (1994).

178. D. J. Wineland, J. J. Bollinger, W. M. Itano, F. Moore, D. Heinzen, *Physical Review A* **46**, R6797 (1992).

179. V. Giovannetti, S. Lloyd, L. Maccone, *Science* **306**, 1330–1336 (2004).

180. A Sørensen, L.-M. Duan, J. Cirac, P. Zoller, *Nature* **409**, 63–66 (2001).

181. J Esteve, C Gross, A Weller, S Giovanazzi, M. Oberthaler, *Nature* **455**, 1216–1219 (2008).

182. T. Fernholz *et al.*, *Physical Review Letters* **101**, 073601 (2008).

183. G. S. Agarwal, R. Puri, R. Singh, *Physical Review A* **56**, 2249 (1997).

184. R. Deb, M. S. Abdalla, S. Hassan, N Nayak, *Physical Review A* **73**, 053817 (2006).

185. S. Chaudhury *et al.*, *Physical Review Letters* **99**, 163002 (2007).

186. C. Law, H. Ng, P. Leung, *Physical Review A* **63**, 055601 (2001).

187. A. Micheli, D Jaksch, J. I. Cirac, P Zoller, *Physical Review A* **67**, 013607 (2003).

188. G. Agarwal, R. Puri, *Physical Review A* **49**, 4968 (1994).
189. G.-R. Jin, Y.-C. Liu, W.-M. Liu, *New Journal of Physics* **11**, 073049 (2009).
190. I. D. Leroux, M. H. Schleier-Smith, V. Vuletić, *Physical Review Letters* **104**, 073602 (2010).
191. C. Gross, T. Zibold, E. Nicklas, J. Esteve, M. K. Oberthaler, *Nature* **464**, 1165–1169 (2010).
192. M. F. Riedel *et al.*, *Nature* **464**, 1170–1173 (2010).
193. M. H. Schleier-Smith, I. D. Leroux, V. Vuletić, *Physical Review A* **81**, 021804 (2010).
194. B. C. Sanders, *Physical Review A* **40**, 2417 (1989).
195. A. Rojo, *Physical Review A* **68**, 013807 (2003).
196. D. Kajtoch, E. Witkowska, *Physical Review A* **92**, 013623 (2015).
197. K. Helmerson, L. You, *Physical Review Letters* **87**, 170402 (2001).
198. J. Wesenberg, K. Mølmer, *Physical Review A* **65**, 062304 (2002).
199. I. Bouchoule, K. Mølmer, *Physical Review A* **65**, 041803 (2002).
200. M. Jafarpour, A. Akhound, *Physics Letters A* **372**, 2374–2379 (2008).
201. A. André, L.-M. Duan, M. Lukin, *Physical Review Letters* **88**, 243602 (2002).
202. C. Gardiner, P. Zoller, *Quantum noise: a handbook of Markovian and non-Markovian quantum stochastic methods with applications to quantum optics* (Springer Science & Business Media, 2004), vol. 56.
203. M. A. Nielsen, I. L. Chuang, *Quantum* **546**, 1231 (2000).
204. Y. Li, Y. Castin, A. Sinatra, *Physical Review Letters* **100**, 210401 (2008).
205. A. Peres, *Physical Review Letters* **77**, 1413 (1996).
206. R. F. Werner, *Physical Review A* **40**, 4277 (1989).
207. C. W. Helstrom, *Quantum detection and estimation theory* (Academic press, 1976).
208. W. K. Wootters, *Physical Review D* **23**, 357 (1981).
209. S. Boixo, A. Monras, *Physical Review Letters* **100**, 100503 (2008).
210. G. A. Durkin, J. P. Dowling, *Physical Review Letters* **99**, 070801 (2007).
211. S. Luo, *Physical Review Letters* **91**, 180403 (2003).
212. P. Szańkowski, *arXiv preprint arXiv:1502.01111* (2015).
213. K Gietka, P Szańkowski, T Wasak, J Chwedeńczuk, *Physical Review A* **92**, 043622 (2015).
214. H. Lee, P. Kok, J. P. Dowling, *Journal of Modern Optics* **49**, 2325–2338 (2002).
215. C. J. Bordé, *Physics Letters A* **140**, 10–12 (1989).
216. K. Gietka, J. Chwedeńczuk, *Physical Review A* **90**, 063601 (2014).
217. C. R. Rao, *Bulletin of Calcutta Mathematical Society* **37**, 81–91 (1945).
218. H. Cramér, *Mathematical Methods of Statistics* (Princeton University Press, 2016), vol. 9.
219. M. Fréchet, *Revue de l'Institut International de Statistique*, 182–205 (1943).
220. G Darmois, *Revue de l'Institut International de Statistique*, 9–15 (1945).

221. R. A. Fisher, presented at the Mathematical Proceedings of the Cambridge Philosophical Society, vol. 22, pp. 700–725.

222. S. L. Braunstein, C. M. Caves, G. J. Milburn, *annals of physics* **247**, 135–173 (1996).

223. C. Helstrom, *Physics Letters A* **25**, 101–102 (1967).

224. A. S. Holevo, *Probabilistic and statistical aspects of quantum theory* (Springer Science & Business Media, 2011), vol. 1.

225. A. W. F. Edwards, *Likelihood* (CUP Archive, 1984).

226. G. M. Tino, M. A. Kasevich, *Atom Interferometry* (IOS Press, 2014), vol. 188.

227. Z Hradil *et al.*, *Physical Review Letters* **76**, 4295 (1996).

228. M Zawisky *et al.*, *Journal of Physics A: Mathematical and General* **31**, 551 (1998).

229. L Pezzé, A Smerzi, G Khoury, J. Hodelin, D Bouwmeester, *Physical Review Letters* **99**, 223602 (2007).

230. J. P. Dowling, *Physical Review A* **57**, 4736 (1998).

231. T. Kim, O. Pfister, M. J. Holland, J. Noh, J. L. Hall, *Physical Review A* **57**, 4004 (1998).

232. C. C. Gerry, R. Campos, *Physical Review A* **68**, 025602 (2003).

233. L Pezzé, L. Collins, A Smerzi, G. Berman, A. Bishop, *Physical Review A* **72**, 043612 (2005).

234. O. Barndorff-Nielsen, R. Gill, *Journal of Physics A: Mathematical and General* **33**, 4481 (2000).

235. L. Seveso, M. A. Rossi, M. G. Paris, *Physical Review A* **95**, 012111 (2017).

236. R. Demkowicz-Dobrzanski, J. Czajkowski, P. Sekatski, *Physical Review X* **7**, 041009 (4 2017).

237. `https://www.youtube.com/watch?v=pYXIM24Neko`.

238. T. Wasak, A. Smerzi, L. Pezzé, J. Chwedeńczuk, *Quantum information processing* **15**, 2231–2252 (2016).

239. C. Chin, R. Grimm, P. Julienne, E. Tiesinga, *Reviews of Modern Physics* **82**, 1225 (2010).

240. F. Dalfovo, S. Giorgini, L. P. Pitaevskii, S. Stringari, *Reviews of Modern Physics* **71**, 463 (1999).

241. I. Bloch, J. Dalibard, W. Zwerger, *Reviews of modern physics* **80**, 885 (2008).

242. J. F. Sherson *et al.*, *Nature* **467**, 68 (2010).

243. D. Hume *et al.*, *Physical review letters* **111**, 253001 (2013).

244. T Wasak, P Szańkowski, J Chwedeńczuk, *Physical Review A* **91**, 043619 (2015).

245. K. Gietka, T. Wasak, J. Chwedeńczuk, F. Piazza, H. Ritsch, *The European Physical Journal D* **71**, 273 (2017).

246. E. T. Jaynes, F. W. Cummings, *Proceedings of the IEEE* **51**, 89–109 (1963).

247. Wikipedia contributors, *Jaynes-Cummings model — Wikipedia, The Free Encyclopedia*.

248. G. Lindblad, *Communications in Mathematical Physics* **48**, 119–130 (1976).

249. S. Haroche, J.-M. Raimond, *Exploring the quantum: atoms, cavities, and photons* (Oxford university press, 2006).

250. C. Gardiner, P. Zoller, in *The Quantum World of Ultra-Cold Atoms and Light Book II: The Physics of Quantum-Optical Devices* (World Scientific, 2015), pp. 1–524.

251. K. Kraus, *States, effects and operations: fundamental notions of quantum theory* (Springer, 1983).

252. C. M. Caves, K. S. Thorne, R. W. Drever, V. D. Sandberg, M. Zimmermann, *Reviews of Modern Physics* **52**, 341 (1980).

253. M Brune, S Haroche, V Lefevre, J. Raimond, N Zagury, *Physical Review Letters* **65**, 976 (1990).

254. A. Ourjoumtsev, R. Tualle-Brouri, J. Laurat, P. Grangier, *Science* **312**, 83–86 (2006).

255. J.-M. Raimond, M Brune, S. Haroche, *Reviews of Modern Physics* **73**, 565 (2001).

256. A. Rauschenbeutel *et al.*, *Physical Review Letters* **83**, 5166 (1999).

257. A. D. Boozer, A. Boca, R. Miller, T. E. Northup, H. J. Kimble, *Physical Review Letters* **98**, 193601 (2007).

258. M. Lettner *et al.*, *Physical Review Letters* **106**, 210503 (2011).

259. T. Aoki *et al.*, *Physical review letters* **102**, 083601 (2009).

260. C. M. Danforth, *Mathematics of Planet Earth* **17** (2013).

261. K Gietka, J Chwedeńczuk, T Wasak, F Piazza, *arXiv preprint cond-mat/1812.01013* (2018).

262. C. G. Moreira, M. J. Pacifico, S. Romaña, *arXiv preprint arXiv:1611.01174* (2016).

263. Wikipedia contributors, *Double pendulum — Wikipedia, The Free Encyclopedia*.

264. G. Boeing, *Systems* **4**, 37 (2016).

265. A. Wolf, J. B. Swift, H. L. Swinney, J. A. Vastano, *Physica D: Nonlinear Phenomena* **16**, 285–317 (1985).

266. A. Peres, *Quantum theory: concepts and methods* (Springer Science & Business Media, 2006), vol. 57.

267. F. Haake, *Quantum signatures of chaos* (Springer Science & Business Media, 2013), vol. 54.

268. H.-J. Stöckmann, *Quantum chaos: an introduction*, 2000.

269. F. Haake, *Quantum SigNatures of Chaos* (Springer Science & Business Media, 2013), vol. 54.

270. E. J. Heller, *Physical Review Letters* **53**, 1515 (1984).

271. J. Emerson, Y. S. Weinstein, S. Lloyd, D. Cory, *Physical review letters* **89**, 284102 (2002).

272. X. Wang, S. Ghose, B. C. Sanders, B. Hu, *Physical Review E* **70**, 016217 (2004).

273. L. J. Fiderer, D. Braun, *Nature Communications* **9**, 1351 (2018).

274. R. H. Dicke, *Physical Review* **93**, 99 (1954).

275. K. Hepp, E. H. Lieb, *Physical Review A* **8**, 2517 (1973).

276. K. Hepp, E. H. Lieb, *Annals of Physics* **76**, 360–404 (1973).

277. R Graham, M Höhnerbach, *Zeitschrift für Physik B Condensed Matter* **57**, 233–248 (1984).

278. C. Emary, T. Brandes, *Physical Review E* **67**, 066203 (2003).

279. C. Emary, T. Brandes, *Physical Review Letters* **90**, 044101 (2003).

280. D. Braak, *Physical Review Letters* **107**, 100401 (10 2011).

281. K. Baumann, C. Guerlin, F. Brennecke, T. Esslinger, *Nature* **464**, 1301 (2010).

282. B. M. Garraway, *Philosophical Transactions of the Royal Society of London A: Mathematical, Physical and Engineering Sciences* **369**, 1137–1155 (2011).

283. A. Altland, F. Haake, *New Journal of Physics* **14**, 073011 (2012).

284. T.-L. Wang *et al.*, *New Journal of Physics* **16**, 063039 (2014).

285. P. G. Silvestrov, C. W. J. Beenakker, *Physical Review E* **65**, 035208 (3 2002).

286. T. Gorin, T. Prosen, T. H. Seligman, M. Žnidarič, *Physics Reports* **435**, 33–156 (2006).

287. S. Boixo *et al.*, *Physical Review Letters* **101**, 040403 (2008).

288. S Danilin *et al.*, *npj Quantum Information* **4**, 29 (2018).

289. A. Y. Kitaev, *arXiv preprint quant-ph/9511026* (1995).

290. W. van Dam, G. M. D'Ariano, A. Ekert, C. Macchiavello, M. Mosca, *Physical Review Letters* **98**, 090501 (2007).

291. K. Jachymski *et al.*, *Physical Review Letters* **120**, 013401 (2018).

292. T. Wasak, K. Jachymski, T. Calarco, A. Negretti, *Physical Review A* **97**, 052701 (2018).

293. F. Mivehvar, S. Ostermann, F. Piazza, H. Ritsch, *Physical Review Letters* **120**, 123601 (2018).

294. K Furuya, M. Nemes, G. Pellegrino, *Physical Review Letters* **80**, 5524 (1998).

295. D. Braun *et al.*, *Rev. Mod. Phys.* **90**, 035006 (3 2018).